Instituto Nacional de Astrofísica
Óptica y Electrónica

"Complete solutions to the oblate spheroidal angular equation and their potential application in optics"

by

Eng. Héctor Carlos Méndez Dzul

A dissertation submitted in partial fulfilment of the requirements for the degree of

Master on Science with Major on Optics

Thesis Advisor:
Alfonso Isaac Jaimes Nájera PhD, INAOE
Thesis Co-Advisor:
Ulises Ruiz Corona PhD, INAOE

August 2018
Tonantzintla, Puebla

Abstract

Spheroidal beams are described by exact solutions to the Helmholtz equation when it is written in oblate spheroidal coordinates. The behavior of spheroidal beams range from highly focused waves to paraxial beams that asymptotically behave as Laguerre-Gauss beams. Their transverse structure is dictated by the spheroidal angular function of the first kind, the latter being a solution to the oblate spheroidal angular equation. In this work we study a new second solution to the latter equation with a specific asymptotic behavior for large spheroidicity parameters. This allows us to find Hankel-like oblate spheroidal angular functions. Our results may find applications in Optics, particularly, in building fundamental traveling waves that constitute spheroidal beams in superposition, with which physical phenomena, such as self-healing, can be described from physical grounds. Finally, a first insight on such application is discussed.

Resumen

Los haces esferoidales se describen mediante soluciones exactas a la ecuación de Helmholtz cuando ésta se escribe en coordenadas esferoidales oblatas. Dichos haces se pueden comportar tanto como ondas altamente enfocadas, como haces paraxiales cuyo comportamiento asintótico es similar al de los haces Laguerre-Gauss. La estructura transversal de los haces esferoidales está dictada por la función angular esferoidal oblata del primer tipo, ésta última siendo una solución a la ecuación angular esferoidal oblata. En este trabajo estudiamos una nueva segunda solución a esta última ecuación con un comportamiento asintótico específico para parámetros de esferoidicidad grandes. Esto nos permite encontrar funciones angulares esferoidales oblatas tipo Hankel. Nuestros resultados pueden encontrar aplicaciones en Óptica, particularmente, en la construcción de ondas viajeras fundamentales que en superposición conforman a los haces esferoidales, con las cuales es posible describir, de principios físicos, fenómenos tales como la autoreconstrucción de haces. Finalmente, discutimos las primeras ideas sobre dicha aplicación.

Contents

List of Figures

Dedicated to my family...

Introduction

It is known from the midst of the nineteenth century by the work of James Clerk Maxwell and the experimental results on Heinrich Hertz, that light is an electromagnetic wave [1] [2]. In free space, electromagnetic waves are described by uncoupled wave equations that are satisfied by the electric and magnetic fields. By considering electromagnetic fields in free space as time harmonic fields, the wave equation can be simplified to the Helmholtz equation so that the wavefields can be described by means of their spatial component. Since the invention of the laser in the 1960s, highly directional wavefields, namely optical beams, grew in importance from both the theoretical and practical standpoints [3] [4]. Under the consideration of highly directional wavefields, the Helmholtz equation can be simplified to the paraxial wave equation. A summary of those paraxial beams has been done by Kogelnik and li [5] . A standard method used in order to obtain solutions from the Helmholtz and the paraxial waves equations consists in the use of a punctual light source that is moved into a complex position so that the solution becomes directional [6] [7] [8]. This method possesses the inherent problem of providing solutions with singularities. In the work of Chavez and Rodriguez [9], it was found by means of the oblate spheroidal coordinate system and its solutions for the Helmholtz equation, that solutions describing highly directional beams can be constructed so that they behave asymptotically as paraxial Laguerre-Gauss beams, or as non-paraxial, highly focused waves depending on the value of a particular parameter. By considering the maximum diffraction angle of a beam as 30 degrees, as described by Siegman [3], it was obtained a threshold that separates the paraxial and non-paraxial behavior of the spheroidal waves, setting aside problems related to singularities. Beams that possesses defined energy distribution as well as defined non trivial wavefront constitution during propagation. Examples of those are the Bessel, Laguerre-Gauss and Hermite-Gauss beams [10] [11] [3]. Structured beams possess interesting physical properties. It is known that electromagnetic fields possesses linear and angular momentum, the angular momentum can either be from the polarization of the field, or from the spatial distribution. The contribution from the spatial distribution can be described as the variation of the poynting vector over a helical wavefront. This characteristic is the

orbital angular momentum [12], and has been used for multiple applications as transferring information [13] and optical manipulation of microparticles [14] [15]. Another interesting property of some structured beams is the following: if a portion of the beam is obstructed by an opaque object, after a certain distance of propagation, the damage is partially " healed ". This property is called self-healing. Much work has been done on this subject [16] [17] [18]. In the case of Bessel beams, it was found by Chavez [19] that the self-healing can be described by means of interfering conical waves, namely, Hankel waves, described by the two linearly independent solutions of the Bessel equation [20] [21]. Furthermore, Hankel waves can be considered as fundamental traveling waves constituting, in superposition, the Bessel beams. In the same spirit, in the work of Jaimes [22] it was constructed a second solution for the associated Laguerre equation, that can be used to describe the physical properties of the Laguerre-Gauss beams through the interference of two Hankel-like, semi-conical waves. However, this approach possesses an inherent problem: the second solution to the associated Laguerre equation that is used to construct the Hankel-like waves, turned out to be a function that approaches infinity as the radial distance increases. Therefore, the Hankel-like semi-conical waves are strictly unbounded functions. Our hypothesis is that this singular behavior is induced by the paraxial approximation, which applies for distances close to the propagation axis, and not necessarily away from it.

This work is centered on the oblate spheroidal angular equation and its linearly independent solutions. As mentioned before, the asymptotic expansion of the angular component of the oblate wavefunction, for large spheroidicity parameters, takes the form of the Laguerre-Gauss beam [9] [23] [24]. Thus, according to our hypothesis, we will use solutions to the exact Helmholtz equation, namely, the spheroidal wavefunctions, since they remain finite over the whole space. In order to construct spheroidal waves that behave asymptotically as the Hankel-like semi-conical waves associated in superposition to the Laguerre-Gauss beams, in this work a revision on the second solution to the spheroidal angular equation is done. The standard second solution to the oblate spheroidal angular equation is not suitable for the construction of Hankel-like spheroidal waves. This work deals with constructing an alternative second spheroidal angular functions that allows the construction of the Hankel-like spheroidal waves. Solving this problem will allow us the exploration of related topics, such as the physical behavior of the spheroidal beams, the nature of the divergence of the Hankel-like waves associated to Laguerre-Gauss beams, and the behavior of non-paraxial beams that are useful in areas as the optical manipulation of microparticles.

From chapter one to chapter four, a brief summary on the background of this work is presented. Chapter one contains the basic theory of paraxial beams, specifically, the

Gaussian beam. Chapter two contains the deduction and general properties of Laguerre-Gauss beams, that is, the solution to the paraxial wave equation in circular cylindrical coordinates. Chapter three contains a summary on the importance of second solutions to the differential equations obtained by solving the Helmholtz or the paraxial wave differential equations with the method of separation of variables, in the context of waves fulfilling the Sommerfeld radiation condition. This is presented in the case of Hankel waves for the Helmholtz equation in circular cylindrical coordinates, as they model the propagation of Bessel beams, being the latter the result on the interference of Hankel waves. In this chapter, is also presented the case of the Laguerre-Gauss beams, where a second solution to the associated Laguerre equation is used to construct Hankel like, semi-conical waves, with which is intended to describe the propagation properties of the Laguerre-Gauss beams. Also, the aforementioned problem of the second solution is discussed. Chapter four contains the basic theory of the spheroidal wavefunctions, the standard method used to compute them, and the connection between the spheroidal wavefunctions and the Laguerre-Gauss beams. Chapter five describes the methods developed in this work to approximate an alternative second solution to the spheroidal angular equation that allows to construct Hankel-like spheroidal waves. Lastly, we present some concluding remarks and perspectives of this work.

Chapter 1

The Gaussian beam

This chapter contains a brief explanation of the Gaussian beam, its deduction and properties, along with background required in further chapters.

1.1 The paraxial equation

The Maxwell equation's play a central role in the theory of electromagnetic fields. These equations describe the dynamics of the electromagnetic phenomena, and they constitute a milestone in the development of the physical theories in the nineteenth century, unifying many of the empirical results obtained for more than a century in a single theory. In vacuum they are expressed as in 1.1

$$\begin{aligned} \vec{\nabla} \cdot \vec{E} &= 0, \\ \vec{\nabla} \cdot \vec{B} &= 0, \\ \vec{\nabla} \times \vec{E} &= -\frac{\partial \vec{B}}{\partial t}, \\ \vec{\nabla} \times \vec{B} &= \mu_0 \epsilon_0 \frac{\partial \vec{E}}{\partial t}, \end{aligned} \tag{1.1}$$

where $\vec{E}$ is the electric field, $\vec{B}$ the magnetic field, ϵ_0 the permittivity of free space, and μ_0 is the permeability of free space. In this case, the speed of light is given by:

$$c = \frac{1}{\sqrt{\epsilon_0 \mu_0}}.$$

By taking the curl in the curl terms of (1.1), and using some vector identities, it is possible to obtain a standard wave equation as the behavior describing the electromagnetic fields [25]

$$\begin{aligned} \frac{1}{c^2}\frac{\partial^2 \vec{E}}{\partial t^2} - \vec{\nabla}^2 \vec{E} = 0. \\ \frac{1}{c^2}\frac{\partial^2 \vec{B}}{\partial t^2} - \vec{\nabla}^2 \vec{B} = 0. \end{aligned} \tag{1.2}$$

The equations (1.2) are of vector nature, however, these last equations are uncoupled. The vector nature of the fields is described by the property of polarization [25]. A field is considered scalar if the variations are only in a direction of polarization, thus, only one component of (1.2) is considered.

Considering a scalar, monochromatic wave, this is, only one frequency, the resultant equation is the Helmholtz equation (1.3), and the temporal component of the wave is given by $\exp(-i\omega t)$, being ω the angular frequency of the wave. The wave equation is reduced to the Helmholtz equation,

$$\nabla^2 U(\vec{r}) + k^2 U(\vec{r}) = 0. \tag{1.3}$$

The Helmholtz equation describes the spatial propagation of the wave. A case of interest is that of a highly directional field, that is, a field in which most of the energy and its variations, are confined in the neighborhood of the propagation axis, usually the z-axis. This last requirement is known as the paraxial condition, and the solutions receives the name of beams, and have the following form,

$$U(\vec{r}) = u(\vec{r}) \exp(ikz). \tag{1.4}$$

Where U is a solution of the Helmholtz equation and u is a paraxial solution. Physically, the paraxial condition can be written as (1.5) [26].

$$\lambda \left| \frac{\partial u}{\partial z} \right| \ll |u| . \tag{1.5}$$

Under the assumptions (1.4) and (1.5), the Helmholtz equation can be simplified to the paraxial wave equation,

$$\nabla_t^2 u(\vec{r}) + 2ik\frac{\partial u(\vec{r})}{\partial z} = 0, \tag{1.6}$$

where ∇_t^2 is the transverse laplacian, given by

$$\nabla_t^2 = \frac{\partial^2}{\partial x^2} + \frac{\partial^2}{\partial y^2}.$$

1.2 Wavefronts and rays

Electromagnetic waves are, in general, complex functions of the space coordinates and time. It is possible to express a wave in the form 1.7

$$\vec{E}_0(\vec{r}) = \vec{e}\, e^{ik_0 n(\vec{s}\cdot\vec{r})}, \tag{1.7}$$

where $\vec{s}$ is an unit vector representing the direction of propagation and $\vec{e}$ is a complex position dependent vector function. If r, the position vector, is much greater than a wavelength, and away from any source, the field in equation (1.7) can be represented locally as a plane wave, and $\vec{e}$ can be slowly varying function independent of k_0, the wavenumber. In this region, the wave can be expressed as

$$\vec{E}_0(\vec{r}) = \vec{e}\, e^{ik_0 S(\vec{r})}, \tag{1.8}$$

where $S(\vec{r})$ is a scalar function of position, namely the optical path of the wave. This wave solution is evaluated in the Maxwell equations (1.1) to obtain the equation that describes $S(\vec{r})$, independent of $\vec{e}$, valid in the approximation of distances much greater than λ. This results in the Eikonal Equation [25],

$$(\vec{\nabla} S(\vec{r}))^2 = n^2, \tag{1.9}$$

with $n = \sqrt{\mu\epsilon}$. The Eikonal equation (1.9) is the connection between the wave optics and the ray optics. The surfaces $S(\vec{r}) = constant$ are called wave fronts. In this approximation, the direction of the time averaged Poynting vector, which represents the energy transfer, is given by

$$\vec{s} = \frac{\vec{\nabla} S}{\|\vec{\nabla} S\|}. \tag{1.10}$$

The vector $\vec{s}$ represents the direction of energy transfer, and the curves tangential to these vectors are called rays. These geometric entities will be used in further sections.

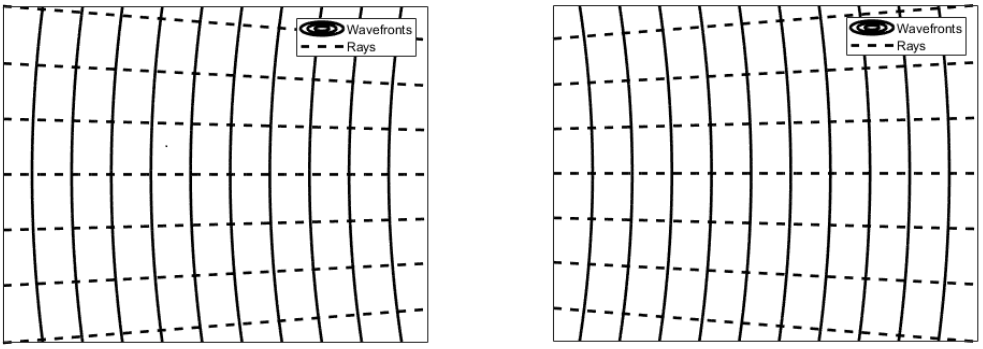

FIGURE 1.1: Wavefronts and rays.

1.3 The plane wave and the spherical wave

Two types of waves represent some of the limits of the asymptotic behavior of wave propagation. These are the plane waves (1.11) and the spherical waves (1.12).

$$u = e^{ikz}, \tag{1.11}$$

$$u = \frac{e^{ikr}}{\|r\|}. \tag{1.12}$$

Their properties are opposite: the plane wave is totally directional, that is, the wave fronts are planes and the rays are straight lines normal to them, thus, the intensity does not depend on position. The other extreme is the spherical wave, whose wave fronts are concentric spheres and with radial lines as the rays. This wave has the property of being non directional, that is, the wave is propagating at any point in space, so the energy decreases with distance. This is illustrated in fig. (1.3) and (1.2)

The curvature of a surface is given by the inverse of radius of the osculating sphere at the point. As the wave fronts in a spherical wave are given by concentric spheres, the curvature decreases with distance. The plane wave, unlike the spherical wave, has null curvature everywhere, and a radius of curvature infinitely large. Even though both kind of waves are widely used, and general solutions of the Helmholtz equation are given in terms of them (like the Huygens principle and the angular spectrum propagation method)[27], these solutions possess inherent difficulties: The plane wave exists in all space with infinite energy, and the spherical wave possesses a singularity at $\vec{r} = 0$. Both of them are nonphysical in this regard.

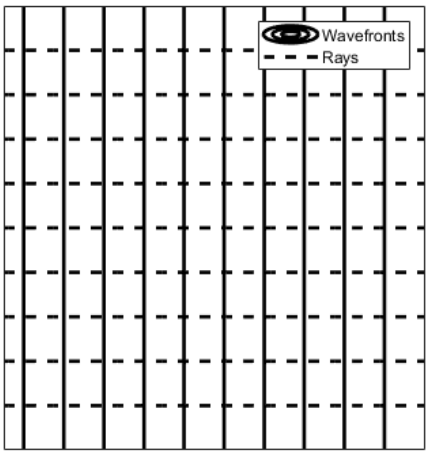

FIGURE 1.2: Wavefronts and rays of the plane wave.

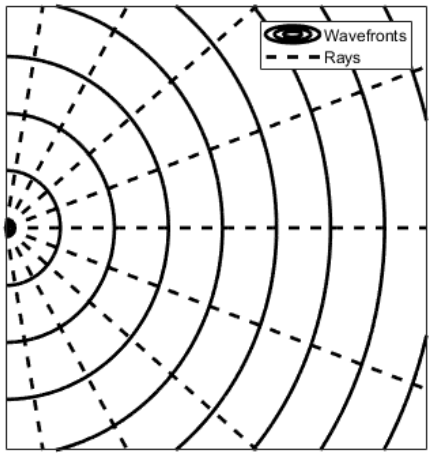

FIGURE 1.3: Wavefronts and rays of the spherical wave.

1.4 The Gaussian beam

The paraxial wave equation (1.6) describes waves which are confined close to the propagation axis. A special case, is the beam presented in a laser, which has a Gaussian intensity profile. To obtain this solution, we can propose a solution of the form

$$u(\vec{r}) = A_0 \exp ik(x^2 + y^2)/2q(z) \exp ip(z), \tag{1.13}$$

where A_0 is a constant, $p(z)$ and $q(z)$ are functions dependent on the propagation distance. Using (1.13) and (1.6), we obtain

$$p(z) = q_0 + z, \tag{1.14}$$

$$q(z) = i \log(\frac{q_0 + z}{q_0}), \tag{1.15}$$

where $q_0 = q(0)$. It is convenient to write $q(z)$ in the form

$$\frac{1}{q(z)} = \frac{1}{R(z)} + \frac{i\lambda}{2\pi\omega(z)^2}, \tag{1.16}$$

where, as we will see later, R corresponds to the radius of curvature of the beam, $\omega(z)$ corresponds to the spot size, taken on the intensity, the measurable value, rather than

on the amplitude, as in some literature [28]. With this definition of q, we have

$$\exp(p(z)) = \frac{1}{1 - z/R_0 + i\lambda z/2\pi\omega_0^2}, \tag{1.17}$$

where $R_0 = R(z = 0)$ and $\omega_0 = \omega(z = 0)$. By taking the real parts of equations (1.15) and (1.16), we obtain

$$\frac{1}{R(z)} = \frac{Re(q_0) + z}{|q_0^2| + 2zRe(q_0) + z^2}, \tag{1.18}$$

from where it can be seen that $R = \infty$ at some value. By taking $R_0 = \infty$, we obtain

$$\frac{1}{q_0} = \frac{i\lambda}{2\pi\omega_0^2}. \tag{1.19}$$

By constructing a new parameter, z_0, the Rayleigh range as

$$z_0 = \frac{\pi\omega_0^2}{\lambda} = \frac{k\omega_0^2}{2}, \tag{1.20}$$

we obtain

$$R(z) = \frac{z}{2z_0} + \frac{2z_0}{z}, \tag{1.21}$$

$$\omega(z) = \omega_0\sqrt{1 + \frac{z^2}{4z_0^2}}. \tag{1.22}$$

The Rayleigh range is the distance at which the beam expands $\sqrt{2}$ the minimum size at the focus. The spot size $\omega(z)$ describes the energy distribution in a transverse plane, it can be seen from equation (1.22) that the spot size takes the geometric form of an hyperbola. The radius of curvature $R(z)$ describes the behavior of the wavefront as the beam propagates. By using $p(z)$ of (1.14) we obtain the Gouy phase shift,

$$\phi(z) = \arctan\frac{z}{2z_0}. \tag{1.23}$$

The Guoy phase shift is a general property of a focusing wave, and can be described as the extra path a straight light ray has to travel, in comparison to the curved path defined with the Eikonal equation [29]. In summary, the full Gaussian beam can be written as

$$u(x, y, z) = \frac{1}{\sqrt{1 + z^2/4z_0^2}} e^{-i\phi(z)} e^{-(x^2+y^2)/2\omega(z)^2} e^{i(x^2+y^2)/2\omega_0^2 R(z)}. \tag{1.24}$$

The figures through 1.4 to 1.9 illustrate the main components of the Gaussian beam.

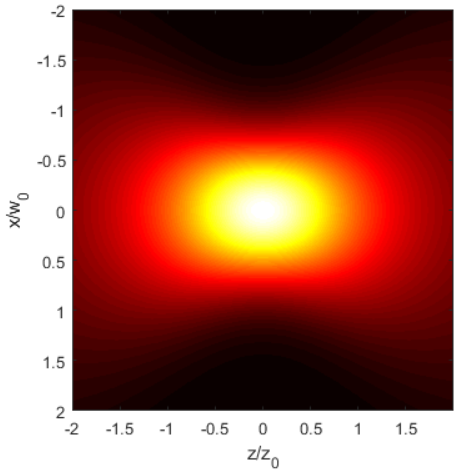

FIGURE 1.4: Longitudinal intensity.

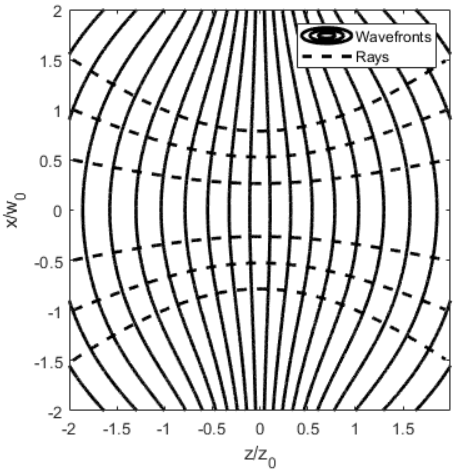

FIGURE 1.5: Wavefronts and rays.

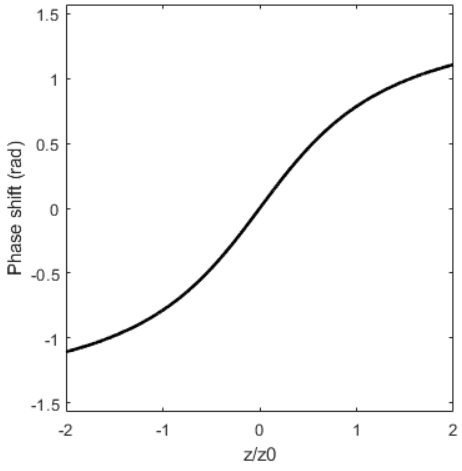

FIGURE 1.6: Guoy phase shift.

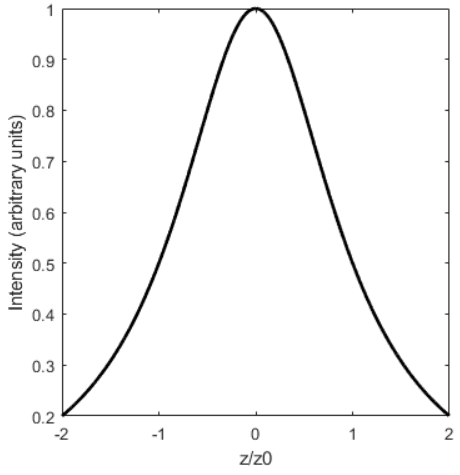

FIGURE 1.7: Intensity on axis.

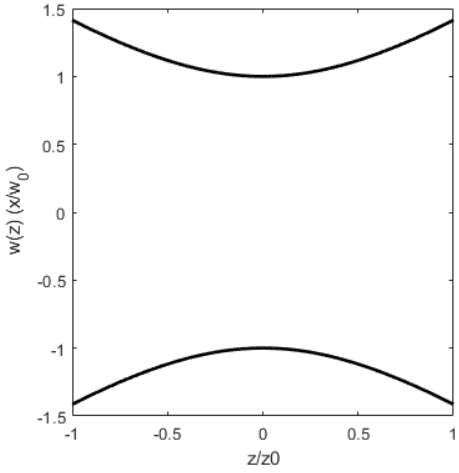

FIGURE 1.8: Waist of the Gaussian beam.

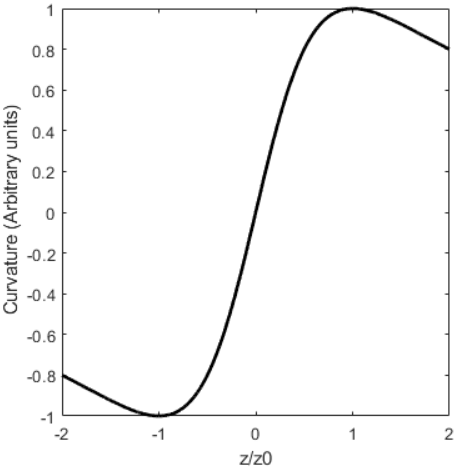

FIGURE 1.9: Curvature of the Gaussian beam.

1.5 Properties of the Gaussian beam

The Gaussian beam, being the starting point to study more general beam solutions, has some interesting properties.

The Gaussian beam (1.24), has a real exponential as a transverse component, given by $e^{-(x^2+y^2)/\omega(z)^2}$. This property means that the Gaussian beam transverse profile is conserved during propagation, the only change is a scale factor given by $\omega(z)$.

The radius of curvature, with the inverse shown in figure 1.9 possesses an interesting property: near the focus the curvature is zero, which means that in this region its phase structure is approximately the one of a plane wave. This can be seen too in figure 1.5. The plane $z = 0$, where the beam is tightest, is called the focal plane, or the beam waist.

Now, to see the form of the Gaussian beam at large distances, let us write the spherical wave as

$$\frac{e^{ikr}}{r} = \frac{e^{ik\sqrt{x^2+y^2+z^2}}}{\sqrt{x^2+y^2+z^2}} = \frac{e^{ikz\sqrt{1+(x^2+y^2)/z^2}}}{z\sqrt{1+(x^2+y^2)/z^2}}. \tag{1.25}$$

Now considering the paraxial region $z \gg \sqrt{x^2+y^2}$, the denominator in equation (1.25) can be approximated by z, and the exponent can be expanded in powers of z. By taking only the first terms, we obtain the paraxial approximation of the spherical wave by

$$\frac{e^{ikr}}{r} \approx \frac{1}{z} e^{ikz}\, e^{ik(x^2+y^2)/2z}, \tag{1.26}$$

Let us write again the amplitude Gaussian beam,

$$E(\vec{r}) = A_0 e^{-i\phi(z)} e^{-(x^2+y^2)/2\omega(z)^2} \frac{e^{ikz}}{\sqrt{1+z^2/4z_0^2}} e^{ik(x^2+y^2)/2R(z)},$$

with z large enough $R(z) \sim z$, $w(z) \sim w_0 z$ and $exp(i\phi(z)) \sim i$, the Gaussian beam, leaving constants aside, can be written as

$$E(\vec{r}) \sim \frac{1}{z} e^{ikz}\, e^{ik(x^2+y^2)/2z}. \tag{1.27}$$

Comparing 1.27 and 1.26, they take the same form at large distances. Last results are summarized as: in short distances a Gaussian beam is closer to a localized plane wave, whereas at large distance, the Gaussian beam is similar to a spherical wave.

The size of the Gaussian beam is given by $\omega(z)$.

$$\omega(z) = \omega_0 \sqrt{1 + \frac{z^2}{4z_0^2}}. \tag{1.28}$$

This takes the form of an hyperbola, as illustrated in figure 1.8, which is the main reason for the use of spheroidal coordinates in the next chapters.

1.6 Natural coordinates for the Gaussian beam

A useful set of coordinates for the Gaussian beam is given by

$$\begin{aligned} z' &= \frac{z}{z_0}, \\ x' &= \frac{x}{w_0}, \\ y' &= \frac{y}{w_0}. \end{aligned} \tag{1.29}$$

Under this transformation, the Gaussian beam is expressed as [30] [31]

$$u(x', y', z') = e^{-i\phi(z')} \frac{1}{\sqrt{1 + z'^2/4}} e^{i(x'^2+y'^2)/2R(z')} e^{-(x'^2+y'^2)/2\omega^2(z')}, \tag{1.30}$$

where

$$\begin{aligned} \phi(z') &= \arctan(z'/2), \\ R(z') &= \frac{z'}{2} + \frac{2}{z'}, \\ \omega(z') &= \sqrt{1 + z'^2/4}. \end{aligned} \tag{1.31}$$

Under these coordinates, the Gaussian beam takes an elegant trait, this is,

$$\begin{aligned} I(z' = 2, x' = 0, y' = 0) &= U\overline{U} = A_0^2/2, \\ I(z' = 0, x' = y' = 1) &= U\overline{U} = A_0^2\, e^{-1}. \end{aligned} \tag{1.32}$$

These natural units are also useful to compare beams of different size, with a better insight than in SI units, as in the first definition of the Gaussian beams. In further chapters, normalized units are used and designated as (x, y, z), unless otherwise stated.

Chapter 2

Laguerre-Gauss beams

This chapter contains a brief explanation on the Laguerre-Gauss (LG) beams, and its properties.

2.1 The Laguerre-Gauss beams

The Gaussian beam, in natural circular cylindrical coordinates (ρ, ϕ, z) can be written as

$$u(\vec{r}) = A_0 r^{-i\phi(z)} \frac{1}{\sqrt{1+z^2/4}} e^{i\rho^2/2R(z)} e^{-\rho^2/2\omega^2(z)}, \tag{2.1}$$

where

$$\rho = \sqrt{x^2+y^2}, \tag{2.2}$$

and $R(z)$, $\phi(z)$ and $\omega(z)$ are the defined in section 1.6.
To derive the solution in circular cylindrical coordinates, the next ansatz is proposed.

$$v(\vec{r}) = F(\rho/\omega(z))G(\phi)u(\vec{r})\, e^{i\alpha(z)}. \tag{2.3}$$

This solution is evaluated in the paraxial wave equation 1.6, which in natural circular cylindrical coordinates is given by

$$\frac{\partial^2 v}{\partial \rho^2} + \frac{1}{\rho}\frac{\partial v}{\partial \rho} + \frac{1}{\rho^2}\frac{\partial^2 v}{\partial \phi^2} + 4i\frac{\partial v}{\partial z} = 0. \tag{2.4}$$

After evaluation, the paraxial equation takes the form

$$\frac{1}{F}\frac{\partial^2 F}{\partial \rho^2} + \frac{4}{Fu}\frac{\partial u}{\partial \rho}\frac{\partial F}{\partial \rho} + \frac{1}{\rho F}\frac{\partial F}{\partial \rho} + \frac{1}{\rho^2 G}\frac{\partial^2 G}{\partial \phi^2} + \frac{4i}{F}\frac{\partial F}{\partial z} - 4\frac{\partial \alpha}{\partial z} = 0. \tag{2.5}$$

With the coordinate transform

$$\zeta = \rho/\omega, \tag{2.6}$$

the paraxial equation is then written as

$$\frac{1}{F}\frac{\partial^2 F}{\partial \zeta^2} + \frac{1}{F}\left(\frac{i\omega^2}{R} - 4\right)\zeta\frac{\partial F}{\partial \zeta} + \frac{1}{\zeta F}\frac{\partial F}{\partial \zeta} - \frac{i\omega^2}{R}\frac{\zeta}{F}\frac{\partial F}{\partial \zeta} + \frac{1}{\zeta^2}\frac{1}{G}\frac{\partial^2 G}{\partial \phi^2} - \omega^2\frac{\partial \alpha}{\partial z} = 0. \tag{2.7}$$

the next step is separating equations for each variable. The first equation comes from taking the last term of equation (2.7), and set it equal to a constant C, since it is the only z-dependent term, which gives

$$\alpha(z) = 2C\arctan(z/2). \tag{2.8}$$

The second to last term in equation (2.7) is the one ϕ-dependant. The solution to the associated differential equation, in order to be a physical solution it must be continuous around a closed path encircling the azimuth axis, that is, the separation constant must be an integer. By this condition, the azimuth function takes the form

$$G(\phi) = A_m e^{im\phi} + B_m e^{-im\phi}. \tag{2.9}$$

Now, equation 2.7 can be written as

$$\frac{d^2 F}{d\zeta^2} + \left(\frac{1}{\zeta} - 2\zeta\right)\frac{dF}{d\zeta} + \left(C - \frac{m^2}{\zeta^2}\right) = 0. \tag{2.10}$$

With the coordinate transformation $y = \zeta^2$, the last equation takes the form 2.11

$$y\frac{d^2 F}{dy^2} + (1-y)\frac{dF}{dy} + \frac{1}{4}\left(C - \frac{m^2}{y}\right)F = 0. \tag{2.11}$$

By trying a power expansion solution (Frobenius solution) to equation 2.11, it can be concluded that an adequate solution can be written as

$$H(y) = y^{-m/2}F(y). \tag{2.12}$$

Is to be noted that equation (2.12) possesses a mistake in the exponent in the book *Mathematical Methods for Optical Physics and Engineering* [28]. By using equations (2.11) and (2.12), the differential equation for H is

$$y\frac{d^2 H}{dy^2} + (m+1-y)\frac{dH}{dy} + \left(\frac{1}{4}C - \frac{m}{2}\right)H = 0. \tag{2.13}$$

the last equation is the associated Laguerre equation, the coefficient $(C/4 - m/2)$, must be an integer in order to obtain a physical solution with finite energy, namely, the radial index n. Thus, the associated Laguerre equation is given by

$$y\frac{d^2H}{dy^2} + (m + 1 - y)\frac{dH}{dy} + nH = 0. \tag{2.14}$$

Equation 2.14 is very important in this work, and shall be used in further chapters. Finally, the Laguerre-Gauss beam can be written as

$$v_n^m(\vec{r}) = \sqrt{\frac{2n!}{\pi(n+m)!}} \left(\frac{\rho}{\omega(z)}\right)^m L_n^m\left(\frac{\rho^2}{\omega^2(z)}\right) e^{im\phi}\, e^{-i\alpha(z)}\, u(\vec{r}), \tag{2.15}$$

where

$$\alpha(z) = (2n + m + 1)\arctan(z/2), \tag{2.16}$$

and the normalization constant is set from

$$\iint_{\mathbb{R}^2} v_n^m(\vec{r})\overline{v_n^m(\vec{r})}\, dr^2 = 1. \tag{2.17}$$

2.2 Properties of the Laguerre-Gauss beam

The Laguerre-Gauss beams possess properties which are different from the Gaussian beam. These properties are briefly explained in this section.

The Laguerre-Gauss beam, as the Gaussian beam, remains with the same form over propagation, up to a scaling factor, namely, they are structurally stable on propagation. Indeed, the squared modulus of the Laguerre-Gauss beam is scaled by $\omega(z)$.

Given the Laguerre-Gauss beam structure, the wavefronts have the same behavior of the Gaussian beam, that is, at the neighborhood of the focal plane the wavefronts are almost plane, and over large distances the wavefronts take the form of the paraxial approximation of the spherical wave, as discussed in the previous chapter.

The waist of the Laguerre-Gauss beams is different from the waist of the Gaussian beam. This is due to the associated Laguerre polynomials that conform the transverse structure of the beams. As stated in [32], an useful definition of spot size will contain all the maxima of intensity of the beam within this region. The spot size defined for a Gaussian beam does not include the last ring of the Laguerre-Gauss beam. Besides, the diffraction angle of a Gaussian beam is not applicable in general to a Laguerre-Gauss beam. By considering the square root of the variance of the Laguerre-Gauss beam as the definition for a spot size, it can be obtained

$$W_L(z) = \omega(z)\sqrt{2n + m + 1}. \tag{2.18}$$

It is remarkable that the Laguerre-Gauss spot size presents a hyperbolic behavior, just like a Gaussian beam spot size. The parameter m describes the angular variation of the beam, and its effect over the beam phase can be observed in figures 2.1 to 2.4 .

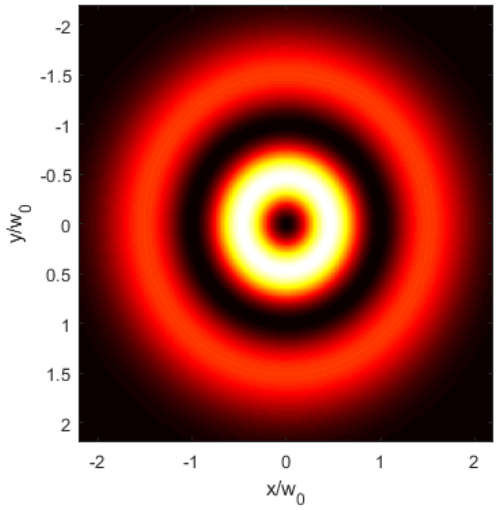

FIGURE 2.1: Intensity of Laguerre-Gauss beam with $n = 1$ and $m = 1$ at the focal plane.

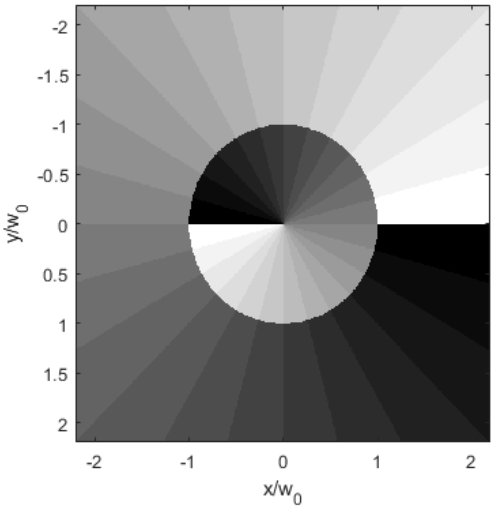

FIGURE 2.2: Phase of Laguerre-Gauss beam with $n = 1$ and $m = 1$ at the focal plane.

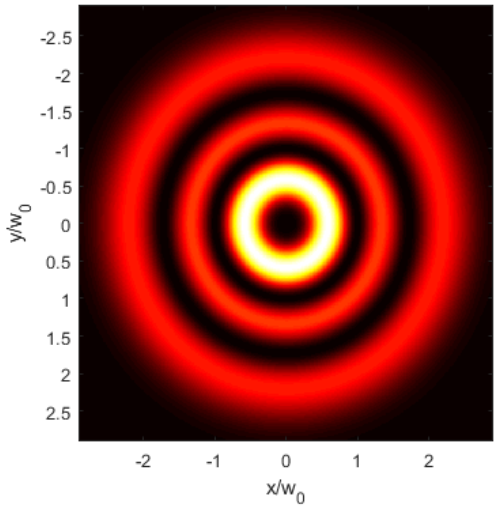

FIGURE 2.3: Intensity of Laguerre-Gauss beam with $n = 2$ and $m = 2$ at the focal plane.

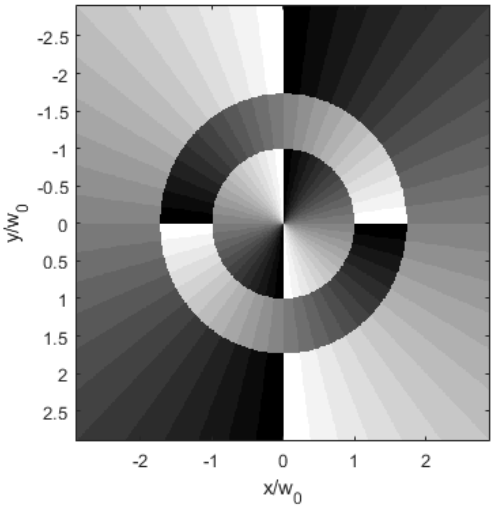

FIGURE 2.4: Phase of Laguerre-Gauss beam with $n = 2$ and $m = 2$ at the focal plane.

In the work of Allen et Al [12] is discussed and proved that for a Laguerre-Gauss beam, the orbital angular momentum is well defined and proportional to m for the field, and $\hbar m$ per photon. This can be understood as follows. The phase term induces a helical wavefront. Since the poynting vector is locally normal to the wavefront, it has an azimuthal component different from zero for $m \neq 0$, implying that the beam carries orbital angular momentum. This property is especially useful in the manipulation of microparticles, as cells, in instruments named optical tweezers.
The Laguerre beams, as other structured beams and modes, possess an useful property, that is, if the beam is obstructed by a relatively small object, after some distance, the beam will heal the damage, thus the Laguerre-Gauss beams are self-healing[33]. This behavior is, at least, hard to explain by considering the theoretical beam rays from the beam. Figures 2.5 and 2.6 illustrates this behavior.

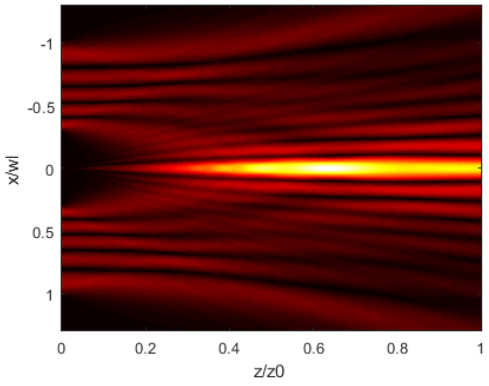

FIGURE 2.5: Self healing of an obstructed Laguerre-Gauss beam with $n = 7$ and $m = 0$.

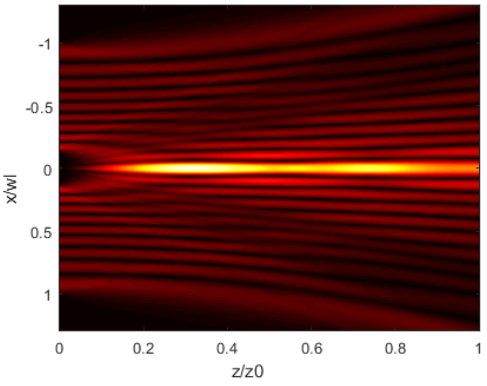

FIGURE 2.6: Self healing of an obstructed Laguerre-Gauss beam with $n = 10$ and $m = 0$.

2.2.1 The asymptotic behavior of the Laguerre-Gaussian beam with large n

At the focal plane, and dropping the normalization constant, the Laguerre Gauss can be expressed as

$$u(z = 0) = (\rho)^m \, L_n^m \left(\rho^2\right) \, e^{im\phi} \, e^{-\rho^2/2}. \tag{2.19}$$

For large n, by using the properties of the associated Laguerre polynomials as a confluent hypergeometric function [34], the Laguerre function takes the asymptotic form [33]

$$L_n^m(x) \sim e^{x/2} \, (x(n + (m + 1)/2))^{-m/2} J_m(2\sqrt{x(n + (m + 1)/2)}),$$

which is equivalent to

$$e^{-x/2}x^{m/2}L_n^m(x) \sim J_m(2\sqrt{x(n+(m+1)/2)}). \tag{2.20}$$

By comparing 2.19 and 2.20, it can be concluded that for large n the Laguerre-Gaussian beam takes the form

$$u(z=0) \sim e^{im\phi}J_m\left(2\rho\sqrt{2(n+(m+1)/2)}\right). \tag{2.21}$$

The result of equation (2.21) relates two important optical fields, the Laguerre-Gauss beam and the Bessel beam. This permits a peer-comparison between Laguerre-Gauss and Bessel beams, and concluding that Laguerre-Gauss beams possess better propagation properties than Bessel beams [33]. The Bessel beams will be discussed in further chapters.

Chapter 3

The need for second solutions

This chapter contains a brief explanation about the Laguerre second solution, and the basis for the Hankel-type waves as constituents of the Laguerre-Gauss beams, in analogy to Bessel beam and the Hankel waves.

3.1 The Bessel beam

3.1.1 Deduction of the Bessel beam

This section contains a brief deduction and explanation of the Bessel beam, and their constituent Hankel waves [19]. The Helmholtz equation

$$\nabla^2 U(\vec{r}) + k^2 U(\vec{r}) = 0, \tag{3.1}$$

can be written, in circular cylindrical coordinates as

$$\frac{1}{\rho}\partial_\rho(\rho\,\partial_\rho)U(\vec{r}) + \frac{1}{\rho^2}\partial_{\phi,\phi}U(\vec{r}) + \partial_{z,z}U(\vec{r}) + k^2 U(\vec{r}) = 0, \tag{3.2}$$

where k, the wave vector, is defined as $k^2 = (2\pi/\lambda)^2 = k_r^2 + k_z^2$. To solve this equation, the method used is the separation of variables, and the solution $U(\vec{r})$, is proposed as $R(\rho)T(\phi)Z(z)$. With some algebraic manipulations, the Helmholtz equation can be written as

$$k^2\rho + \frac{\rho R''(\rho)}{R(\rho)} + \frac{R'(\rho)}{R(\rho)} + \frac{T''(\phi)}{\rho T(\phi)} + \frac{\rho Z''(z)}{Z(z)} = 0, \tag{3.3}$$

this equation is readily separable, and the solutions depend on the boundary conditions. In optics, the solution to equation (3.3) must be finite and continuous everywhere. By

separating the z-dependent term, and setting it equal to $-k_z^2$, the resultant differential equation for $Z(z)$ is

$$\frac{Z''(z)}{Z(z)} = -k_z^2, \tag{3.4}$$

and its general solution can be expressed as

$$Z(z) = c_1 e^{ik_z z} + c_2 e^{-ik_z z}. \tag{3.5}$$

Note that we are taking $k_z \in \mathbb{R}$ in equation (3.3). Taking the $T(\phi)$ terms and setting them equal to $-m^2$, where m must be an integer for $T(t)$ being continuous around a close loop around the z axis, the resulting differential equation is

$$\frac{T''(\phi)}{T(\phi)} = -m^2, \tag{3.6}$$

whose general solution can be written as

$$T(\phi) = c_3 e^{im\phi} + c_4 e^{-im\phi}. \tag{3.7}$$

The remaining differential solution, after substituting the constants, is written as follows

$$\rho\left(k_z^2 - k^2\right) R(\rho) + \frac{m^2 R(\rho)}{\rho} + \rho R''(\rho) - R'(\rho) = 0 \tag{3.8}$$

By writing $k^2 - k_z^2 = k_r^2$, and some algebraic manipulations, the differential equation can be written as

$$\rho^2 R''(\rho) + \rho R'(\rho) + \left(\rho^2 k_\rho^2 - m^2\right) R(\rho) = 0,$$

this is a Bessel differential equation, and the general solution can be written in the following form

$$R(\rho) = c_5 J_m(k_\rho \rho) + c_6 N_m(k_\rho \rho),$$

where J_m is the Bessel function of the first kind, and N_m is the Bessel function of the second kind also known as Neumann function. To obtain the standard solution, some conditions are taken for the coefficients $c_1 \ldots c_6$. We are interested in solutions that describe waves propagating along the $z-$axis direction, and solutions with only one orbital angular momentum phase term, thus, $c2 = c4 = 0$. The Bessel function of the second kind N_m possesses a singularity at $\rho = 0$, thus along the z-axis. Commonly, the physical solution is chosen to avoid this singularity, and thus, c_2 is equal to zero. However in further sections these solutions will be proved to have real physical meaning. Thus, the standard Bessel beam is

$$U(\rho, \phi, z) = e^{im\phi}\, e^{ik_z z} J_m(k_\rho \rho). \tag{3.9}$$

3.1.2 Properties of the Bessel beam

The Bessel modes have properties very different compared to the Gaussian beam. This properties have been studied in many works. In this section we present some of them.

3.1.2.1 The nondiffracting property of the Bessel beam

In the work of Durnin [10], it was pointed out a peculiar property of the Bessel mode, if ideally, it does not change over propagation in space, this can be expressed as

$$\|U(\rho, \phi, z = 0)\|^2 = \|U(\rho, \phi, z > 0)\|^2 \tag{3.10}$$

That is, an ideal Bessel beam is non-diffracting. However, the Bessel function of the first kind is not a square integrable function. But a real Bessel beam, just like a real plane wave, cannot have an infinite amount of energy. If we truncate it by using a circular aperture, the behavior is very different from an ideal Bessel beam. The former, as it propagates, it undergoes diffraction, remaining non-diffracting only in a delimited region of space . In figures 3.1 and 3.2 both theoretical and approximate Bessel modes are illustrated with m=0 and $k_r = 1/10$.

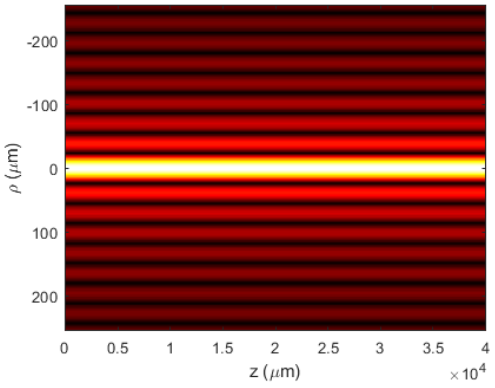

FIGURE 3.1: Amplitude of theoretical Bessel beam.

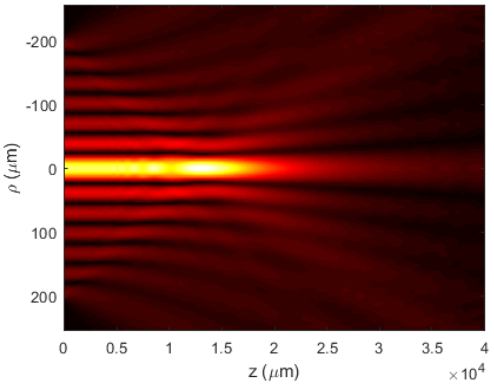

FIGURE 3.2: Amplitude of actual Bessel beam.

On the other hand, a very interesting property of Bessel beams is the self-healing. A relatively small damage to the beam will reconstruct after propagating certain distance. This property was first noticed by Bouchal et al. [35] and it was explained in terms of geometrical considerations. This behavior is illustrated in figures 3.3 and 3.4.

Furthermore, Bessel beams, like the Laguerre-Gauss beams, display an angular dependence of $\exp(im\phi)$, and thus, have a well defined amount of orbital angular momentum. Although Bessel beams have the advantage of being nondiffracting, they remain that

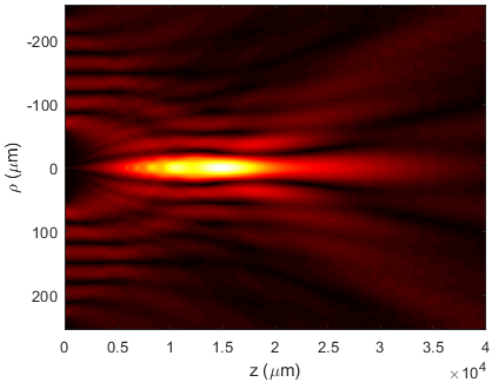

FIGURE 3.3: Self healing of a Bessel beam with m=0 and $k_r = 1/10$.

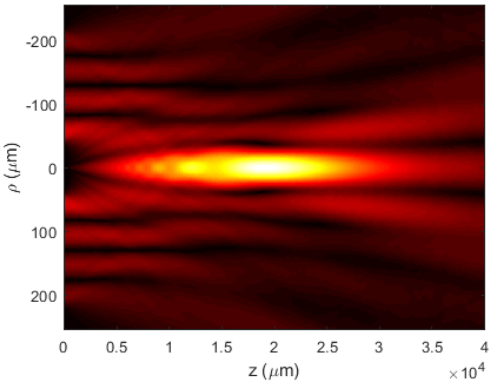

FIGURE 3.4: Self healing of a Bessel beam with m=0 and $k_r = 1/15$.

way only in a limited region of space. In this sense Laguerre-Gauss beams have a farther stable propagation than Bessel beams under similar conditions [33].

3.1.3 The Sommerfeld radiation condition

By solving the Helmholtz equation, we obtain a general mathematical solution, and like it was shown in section 3.1, the physical solution must be chosen by considering boundary conditions. The latter specify the physical solution unambiguously. We are interested in free space wave propagation, and it has its own boundary condition, namely, the Sommerfeld radiation condition [36]. It can be written as :

$$\lim_{r\to\infty} r\left(ikU - \frac{\partial U}{\partial r}\right) = 0, \tag{3.11}$$

where U is a solution for the Helmholtz equation.
The Sommerfeld radiation condition can be understood in the following way: it requires that the solution behaves as an outgoing wave asymptotically for $\rho \to \infty$. In other words, there cannot be incoming waves from infinity. If applying the Sommerfeld radiation condition to a plane wave $\exp(i\vec{k}\cdot\vec{r})$, it can be seen that a plane wave does not fulfill the radiation condition, and is not suitable as a physical solution. An interesting case is the spherical wave. This can be written as $\exp(ikr)/r$ or $\exp(-ikr)/r$ for an outgoing (diverging) and incoming (converging) spherical wave, respectively. For the converging wave:

$$\begin{aligned} &\lim_{r\to\infty} r\left(-ik\frac{e^{ikr}}{r} - \frac{\partial}{\partial r}\frac{e^{-ikr}}{r}\right), \\ &\lim_{r\to\infty} \frac{e^{-ikr}(1+2ikr)}{r} \neq 0 \end{aligned} \tag{3.12}$$

while for the outgoing wave:

$$\begin{aligned} &\lim_{r\to\infty} r\left(ik\frac{e^{ikr}}{r} - \frac{\partial}{\partial r}\frac{e^{ikr}}{r}\right), \\ &\lim_{r\to\infty} \frac{e^{ikr}}{r} = 0. \end{aligned} \tag{3.13}$$

From this, it can be concluded that an incoming spherical wave does not fulfill the Sommerfeld radiation condition, while the outgoing does. Furthermore, it can be concluded that a solution to the Helmholtz equation that behaves asymptotically as an outgoing spherical wave also fulfills the radiation condition.

3.1.4 The Sommerfeld radiation condition and the Bessel beam

As it was discussed in the work of Chavez-Cerda [19] the standard Bessel beams do not fulfill the radiation condition. This and related results are treated in this section.
To evaluate the radiation condition for the Bessel beam, it is important to study the asymptotic behavior of the Bessel function for large arguments. For both Bessel functions of the first and second kind, their asymptotic expansions are:

$$\begin{aligned} J_m(x) &\sim \sqrt{\frac{2}{\pi z}}\cos\left(x - \frac{m\pi}{2} - \frac{\pi}{4}\right) \\ Y_m(x) &\sim \sqrt{\frac{2}{\pi z}}\sin\left(x - \frac{m\pi}{2} - \frac{\pi}{4}\right) \end{aligned} \tag{3.14}$$

Another form to express the solution of the Bessel equation are the Hankel functions, which in terms on J_m and N_m are defined as:

$$\begin{aligned} H_m^{(1)}(x) &= J_m(x) + iN_m(x) \\ H_m^{(2)}(x) &= J_m(x) - iN_m(x) \end{aligned} \tag{3.15}$$

With their respective asymptotic expansions for large arguments

$$\begin{aligned} H_m^{(1)}(x) &\sim \frac{(1-i)e^{ix-\frac{i\pi m}{2}}}{\sqrt{\pi x}} \\ H_m^{(2)}(x) &\sim \frac{(1+i)e^{\frac{i\pi m}{2}-ix}}{\sqrt{\pi x}} \end{aligned}$$

The radiation condition needs to be evaluated in the radial direction, and for this case it can be written as

$$\lim_{\rho\to\infty}\sqrt{\rho}\left(\frac{dH}{d\rho}-ik_rH\right)=0. \tag{3.16}$$

By evaluating the radial component of Bessel beams in the equation (3.9)

$$\begin{aligned}
&\lim_{\rho\to\infty}\sqrt{\rho}\left(\frac{d}{d\rho}J_m(k_r\rho)-ik_rJ_m(k_r\rho)\right),\\
\sim&\lim_{\rho\to\infty}\sqrt{\rho}\left(\frac{d}{d\rho}\sqrt{\frac{2}{\pi}}\sqrt{\frac{1}{\rho k_r}}\cos\left(-\rho k_r+\frac{\pi m}{2}+\frac{\pi}{4}\right)-ik_r\sqrt{\frac{2}{\pi}}\sqrt{\frac{1}{\rho k_r}}\cos\left(-\rho k_r+\frac{\pi m}{2}+\frac{\pi}{4}\right)\right),\\
\sim&\frac{(1-i)k_re^{\frac{1}{2}i(\pi m-2\rho k_r)}}{\sqrt{\pi}}.
\end{aligned} \tag{3.17}$$

therefore standard Bessel beams also do not fulfill Sommerfeld's radiation condition. Additionally the second solution N_m also does not fulfill Sommerfeld's condition. The only solution which fulfills the radiation condition is the one of the form

$$U(\rho,\phi,z)=e^{im\phi}\,e^{ik_zz}H_m^{(1)}(k_\rho\rho). \tag{3.18}$$

Implications of this results are briefly reviewed in next section, and are in accordance with reference [19].

3.1.5 Properties of the Hankel waves and its relationship with Bessel beams

Both Hankel waves and spherical waves have similar properties. Hankel waves can be described as diverging and converging, not from a point source as in the spherical case, but from the propagation axis, and like in the case of the spherical wave, only the diverging solution fulfills the radiation condition.
The wavefronts of the wave $H_m^{(1)}(\vec{r})$ are diverging cones, while the wavefronts of the wave $H_m^{(2)}(\vec{r})$ are converging cones. The wavefronts and rays of $H_0^{(1)}(\vec{r})$ and $H_0^{(2)}(\vec{r})$ are shown in figures 3.5 and 3.6.

Under the Hankel waves scheme, the properties of truncated Bessel beams of the first kind are readily explained. Bessel beams are standing waves produced by interference of the two Hankel waves:

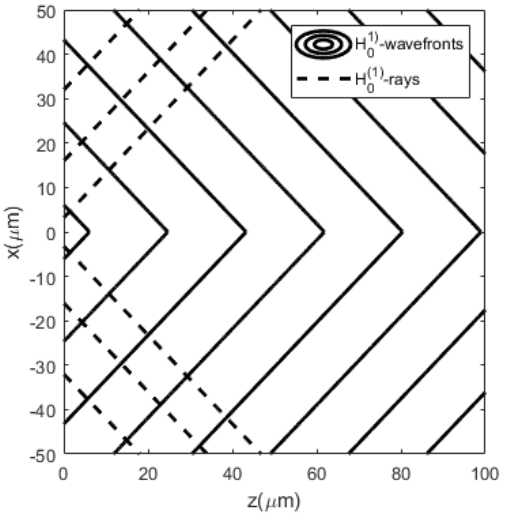

FIGURE 3.5: Wavefronts and rays of $H_0^{(1)}(\vec{r})$.

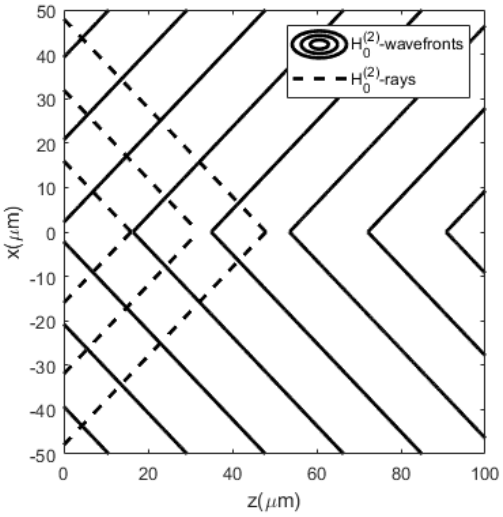

FIGURE 3.6: Wavefronts and rays of $H_0^{(2)}(\vec{r})$.

$$\begin{aligned} U &= e^{im\phi}\, e^{ik_z z} H_m^{(1)}(k_r\rho) + e^{im\phi}\, e^{ik_z z} H_m^{(2)}(k_\rho\rho) \\ &= e^{im\phi}\, e^{ik_z z}(J_m(k_r\rho) + iN_m(k_r\rho)) + e^{im\phi}\, e^{ik_z z}(J_m(k_r\rho) - iN_m(k_r\rho)), \\ &= 2e^{im\phi}\, e^{ik_z z} J_m(k_r\rho) \end{aligned} \tag{3.19}$$

This also explains the physics of Bessel beams. Bessel beams only exist where its constituent Hankel waves interfere. This can be seen by superposing the Bessel beam and the rays of the Hankel waves in figures 3.7 and 3.8. In conclusion, even though normally

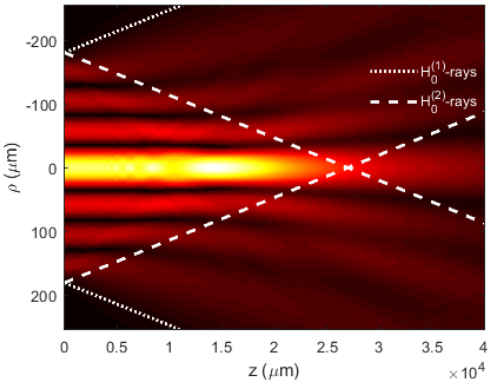

FIGURE 3.7: Region of existence of the Bessel beam and its associated Hankel rays.

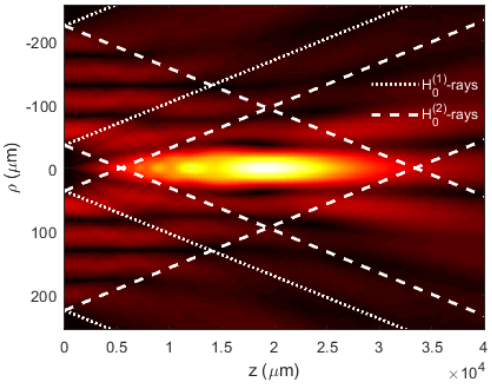

FIGURE 3.8: Self healing of obstructed Bessel beam and its associated Hankel rays.

solutions as the Bessel function of the second kind and the Hankel functions are usually discarded and deemed as nonphysical, such solutions may contain and explain physical phenomena, as in the case of the Hankel waves and the Bessel beams.

3.2 The second Laguerre solution

In chapter 3 a brief introduction to the standard Laguerre-Gauss beams was presented. As in the case of Bessel beams, we will explore the possibility of describing Laguerre-Gauss beams in the traveling wave approach, that is, to write Laguerre-Gauss beams as the superposition of two counter propagating traveling waves. As we have shown in the previous chapter, Laguerre polynomials behave asymptotically as the Bessel function of the first kind. In this section we will obtain a second solution to the associated Laguerre equation that behaves asymptotically as the Bessel function of the second kind, so that we can find, in analogy to Hankel waves, what we will call from now on Hankel-Laguerre traveling waves

3.2.1 First attempt to obtain a second solution for the Laguerre equation

The associated Laguerre equation is given by 2.14, presented here for convenience,

$$x\frac{d^2H}{dx^2} + (m+1-x)\frac{dH}{dx} + nH = 0.$$

From the basic theory of second order differential equation[37], given a first solution for a second order differential equation, a second linearly independent solution can be obtained in the following way

$$y_2(x) = y_1(x)\int^x \frac{\exp\left(-\int^{x_1} P(x_2)\,dx_2\right)}{(y_1(x_1))^2}\,dx_1, \tag{3.20}$$

where $P(x)$ is the coefficient of the first derivative term of the differential equation in the form $y''(x) + P(x)y'(x) + q(x)y(x) = 0$. In particular, for the associated Laguerre equation, a second solution, denominated as $L_n^{m[2]}$,can be expressed as

$$\begin{aligned} L_n^{m[2]}(x) &= C_0\, L_n^m(x)\int^x \frac{\exp\left(-\int^{x_1}(m+1-x_2)/x_2\,dx_2\right)}{(L_n^m(x_1))^2}\,dx_1, \\ &= \frac{1}{\pi}\,L_n^m(x)\int^x \frac{e^{x_1}}{x_1^{m+1}(L_n^m(x_1))^2}\,dx_1. \end{aligned} \tag{3.21}$$

This second solution, as with Laguerre polynomials, does satisfy recurrence relations

$$\begin{aligned} L_{k+1}^{\alpha[2]}(x) &= \frac{(2k+1+\alpha-x)L_k^{\alpha[2]}(x) - (k+\alpha)L_{k-1}^{\alpha[2]}(x)}{k+1}, \\ L_{k-1}^{\alpha+1[2]}(x) &= \frac{1}{x}\left((k+\alpha)L_{k-1}^{\alpha[2]}(x) - kL_k^{\alpha[2]}(x)\right). \end{aligned} \tag{3.22}$$

However, as it will be stressed in the next section, this second solution, in the form in which it is written, is not suitable to formally study its asymptotically behavior in terms of the Neumann function N_m.

3.2.2 A formal expansion for the second Laguerre

As mentioned at the beginning of this section, we are looking for a second solution of the associated Laguerre equation that behaves asymptotically as the Neumann function so that traveling waves, in the case of Laguerre-Gauss beams, can be defined. The latter second solution is not written in a suitable form to perform such asymptotic analysis. In the last chapter, it was presented the asymptotic expansion of the associated Laguerre polynomials for large values of n, given by:

$$L_n^m(x) \sim e^{x/2}\left(x(n+(m+1)/2)\right)^{-m/2} J_m(2\sqrt{x(n+(m+1)/2)}), \tag{3.23}$$

Then we look for a second solution with an asymptotic expansion of the form

$$X_n^m(x) \sim e^{x/2} x^{-m/2} N_m(2\sqrt{x(n+(m+1)/2)}) \tag{3.24}$$

As it was shown in reference [22], this can be obtained by using the confluent hypergeometric function and the linearly independent second solution, the Tricomi function following a procedure similar to the one introduced by Hankel in the definition of the Neumann function [38]. The associated Laguerre polynomial, expressed in terms of the confluent hypergeometric takes the form

$$L_n^m(x) = \frac{(m+1)_n}{n!} {}_1F_1\left(-n, m+1, x\right). \tag{3.25}$$

By using the Tricomi function to obtain a second linearly independent solution, we define, as in reference [22],

$$X_\nu^m(x) = \frac{\Gamma(\nu+m+1)\,{}_1F_1\left(-\nu, m+1, x\right) - m!\cos\nu\pi\, U(-\nu, m+1, x)}{\sin\nu\pi}, \tag{3.26}$$

where ν is not an integer. However, we are interested in the integer case, then we define, $X_n^m := \lim_{\nu\to n} X_\nu^m$, with n integer.As it was proved in [22], X_n^m is a second solution of the Laguerre equation, that by means of L'Hopital's rule, it can be expressed as

$$X_n^m(x) = \frac{(-1)^n}{\pi}\frac{\partial}{\partial\nu}\left[\Gamma(\nu+m+1)\,{}_1F_1\left(-\nu,m+1,x\right)\right]\Big|_{\nu=n}$$
$$-\frac{m!}{\pi}\frac{\partial}{\partial\nu}U\left(-\nu,m+1,x\right)\Big|_{\nu=n}.$$

By using the definition of the confluent hypergeometric function and the Tricomi function in last equation, the explicit form of the second solution to the associated Laguerre equation can be written as

$$X_n^m(x) = \frac{(-1)^n n!m!(n+m)!}{\pi}\left[\sum_{k=1}^{m}\frac{(k-1)!}{(n+k)!(m-k)!}x^{-k} + (-1)^{n+1}\sum_{k=n+1}^{\infty}\frac{(k-n-1)!}{(m+k)!k!}x^k\right.$$
$$\left.+\sum_{k=0}^{n}\frac{(-x)^k}{(n-k)!(m+k)!k!}\left[-\mathrm{Ln}(x)+\psi(m+k+1)+\psi(k+1)-\psi(n-k+1)\right]\right], \tag{3.27}$$

where ψ is the Digamma function [39]. This solution is singular at $x = 0$, what clearly makes it independent of the first solution.

For this solution, to obtain an asymptotic expansion is not a simple task, but in reference [22] it is proved to have the form

$$X_n^m(x) \sim (-1)^{n+1} n!\, m!\, N^{m/2} e^{x/2} x^{-m/2} N_m\left(2\sqrt{x(n+(m+1)/2)}\right). \tag{3.28}$$

for large n. It is interesting that the second solution in equation (3.21), as shown by heuristic methods, is proportional to $X_n^m(x)$. Nevertheless for a high order polynomial, the second solution presented in equation (3.21) presents very low numerical accuracy at double precision, and the use of equations of recurrence (3.22) possesses an inherent numerical instability which limits its use to low grade and order second solutions. Therefore, the expansions of the associated Laguerre equation solutions, can be written as:

$$\frac{n!N^{m/2}}{(n+m)!}e^{-x/2}x^{m/2}L_n^m(x) \sim J_m(2\sqrt{Nx}), \tag{3.29}$$

$$\frac{(-1)^{n+1}}{n!\,m!\,N^{m/2}}e^{-x/2}x^{m/2}X_n^m(x) \sim N_m(2\sqrt{Nx}), \tag{3.30}$$

where $N = n + (m+1)/2$. This representation possesses an interesting property, the left hand side of equation (3.30) has the form of the Laguerre-Gauss beam at the focal

plane, while the right hand side of equation (3.30) has only the Bessel function N_m. Examples of those asymptotic expansions are shown in figures 3.9 and 3.10.

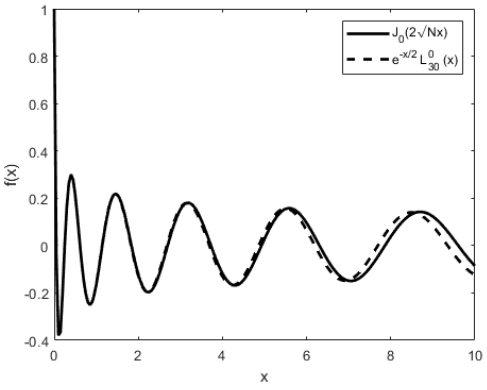

FIGURE 3.9: Asymptotic expansion (3.29) for $n = 30$ and $m = 0$.

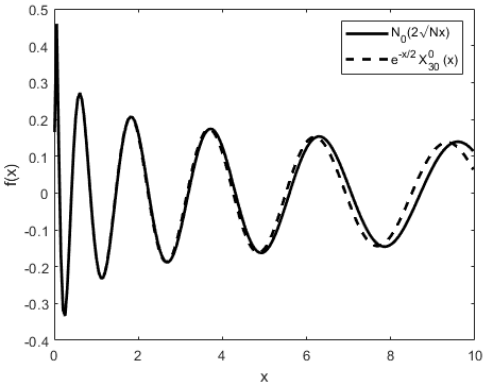

FIGURE 3.10: Asymptotic expansion (3.30) for $n = 30$ and $m = 0$.

3.2.3 The Hankel-Laguerre waves

By adding equation (3.29) and i times equation(3.30) we obtain a solution to the associated Laguerre equation with the envelope of a Laguerre-Gauss beam, that behaves asymptotically as the Hankel wave $H^{(1)}$ for large values of n. The phase of the Hankel Laguerre waves at the focal plane are semiconical within the spot size of the associated Laguerre-Gauss beam. By increasing the radial index n, the semiconical wavefronts approximate the wavefront of the Bessel wave. Some examples of the amplitude, phase, wavefronts and rays of the Hankel-like Laguerre waves are shown in figures 3.11 to 3.14.

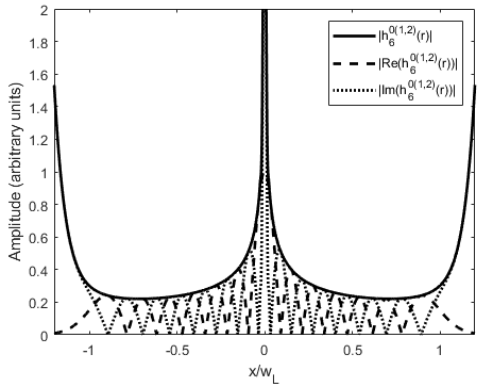

FIGURE 3.11: Amplitude at the focal plane of $h_6^{0(1,2)}(r)$.

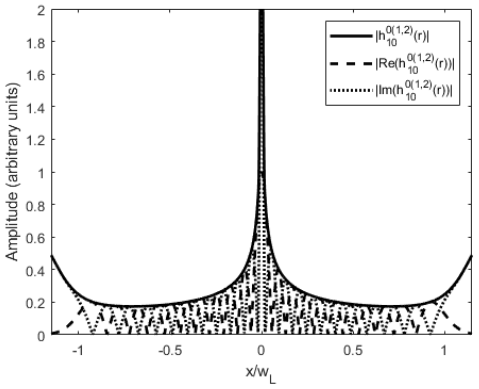

FIGURE 3.12: Amplitude at the focal plane of $h_{10}^{0(2)}(r)$.

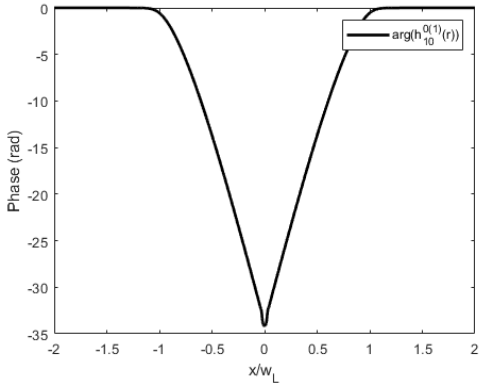

FIGURE 3.13: Phase of $h_{10}^{0(1)}(z=0)$.

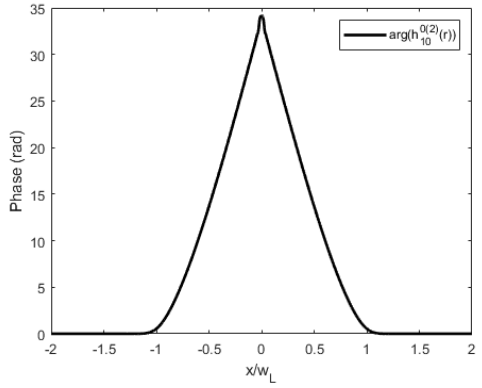

FIGURE 3.14: Phase of $h_{10}^{0(2)}(z=0)$.

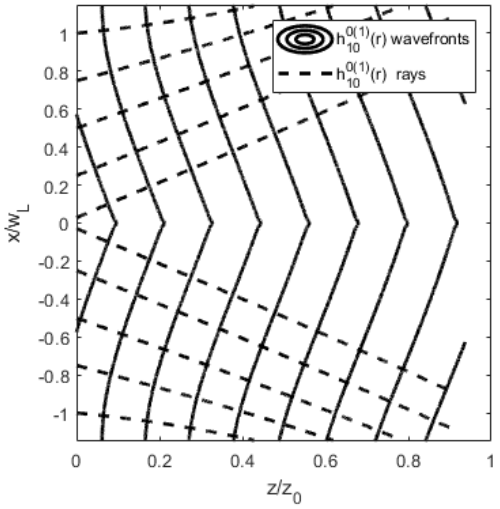

FIGURE 3.15: Wavefronts and rays of $h_{10}^{0(1)}(\vec{r})$.

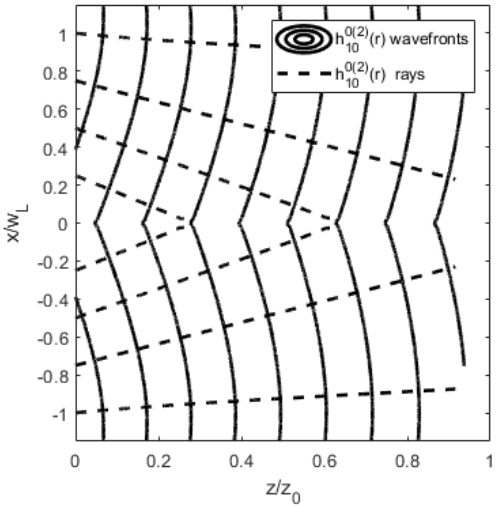

FIGURE 3.16: Wavefronts and rays of $h_{10}^{0(2)}(\vec{r})$.

Let us define the Hankel Laguerre waves as

$$\begin{aligned} h_n^{m(1)}(\vec{r}) &= \left(L_n^m(2\rho^2/\omega(z)^2) + iX_n^m(2\rho^2/\omega(z)^2)\right) u(\vec{r}), \\ h_n^{m(2)}(\vec{r}) &= \left(L_n^m(2\rho^2/\omega(z)^2) - iX_n^m(2\rho^2/\omega(z)^2)\right) u(\vec{r}), \end{aligned} \tag{3.31}$$

where $u(\vec{r})$ contain the remaining terms of the Laguerre-Gauss beam. By means of interference of the Hankel Laguerre waves it is possible to obtain the Laguerre-Gauss beam as a standing wave

$$\begin{aligned} h_n^{m(1)}(\vec{r}) + h_n^{m(2)}(\vec{r}) = &\left(L_n^m(2\rho^2/\omega(z)^2) + iX_n^m(2\rho^2/\omega(z)^2)\right) u(\vec{r}) + \\ &\left(L_n^m(2\rho^2/\omega(z)^2) - iX_n^m(2\rho^2/\omega(z)^2)\right) u(\vec{r}), \\ =&2L_n^m(2\rho^2/\omega(z)^2)u(\vec{r}). \end{aligned} \tag{3.32}$$

Therefore the Hankel Laguerre waves locally behave (asymptotically for large values of the radial index n) as the traveling Hankel waves. Then we have obtained the traveling waves that conform in superposition (interference) the Laguerre-Gauss beams. The use of the Hankel-Laguerre waves to describe the self-healing of obstructed Laguerre-Gauss beams[40] is shown in figures 3.17 to 3.22.

However, as discussed in reference [22], the second solution diverges, for large values of x, fast enough so the Hankel Laguerre wave diverges too for $\rho \to \infty$. Although that divergent behavior is cancelled out in the interference of the Hankel Laguerre waves (X_n^m is cancelled out in the sum $h_n^{m(1)} + h_n^{m(2)}$), their asymptotic behavior for large values of ρ is a problem that must be addressed. Our hypothesis is that the paraxial approximation induces the singular behavior in the second solutions of the paraxial wave equation. Therefore, we will study the exact solutions of the Helmholtz equation that behave asymptotically as Laguerre-Gauss beams, and construct the corresponding travelling waves. This is the main concern of further chapters.

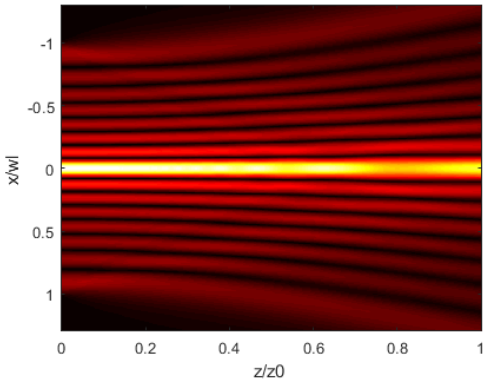

FIGURE 3.17: Laguerre-Gauss beam with $n = 7$ and $m = 0$.

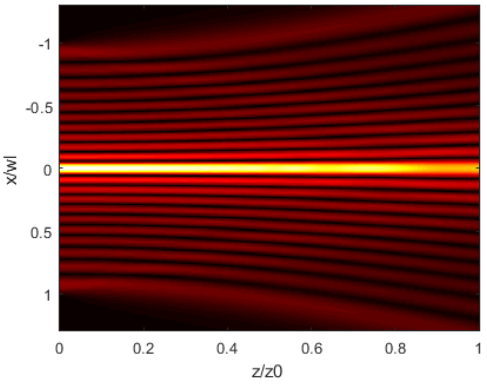

FIGURE 3.18: Laguerre-Gauss beam with $n = 10$ and $m = 0$.

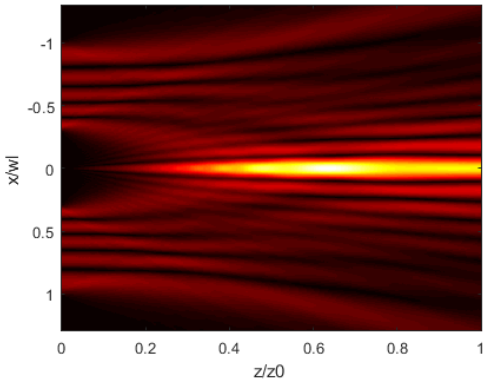

FIGURE 3.19: Obstructed Laguerre-Gauss beam with $n = 7$ and $m = 0$.

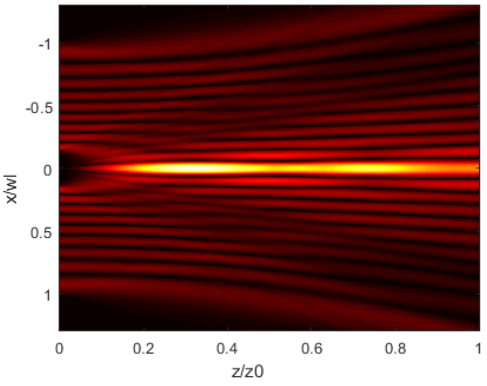

FIGURE 3.20: Obstructed Laguerre-Gauss beam with $n = 10$ and $m = 0$.

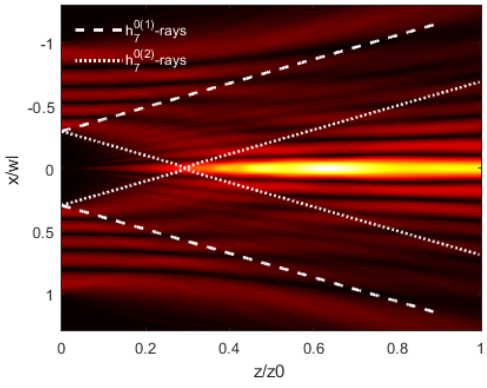

FIGURE 3.21: Obstructed Laguerre-Gauss beam with $n = 7$ and $m = 0$ and its associated Hankel-Laguerre rays.

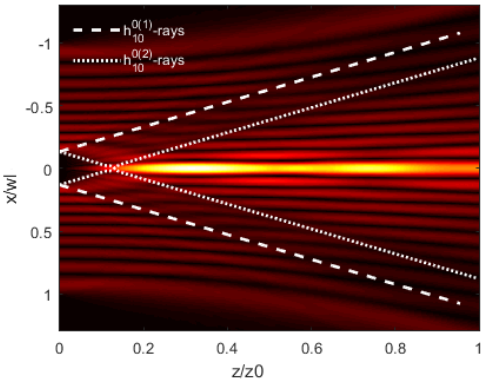

FIGURE 3.22: Obstructed Laguerre-Gauss beam with $n = 10$ and $m = 0$ and its associated Hankel-Laguerre rays.

Chapter 4

Spheroidal functions

This chapter includes a brief introduction to the theory of the spheroidal functions and the connection between spheroidal wavefunctions and Laguerre-Gaussian beams.
Many problems in physics and mathematics involve the exploitation of the symmetries of the system under study. This could avoid difficulties, as in the case of solving centre-symmetrical problems in Cartesian coordinates or by choosing the cylindrical coordinates in axial-symmetrical systems[41]. In our case of interest, the coordinate system used is the oblate spheroidal, which is one of the eleven coordinate systems where the Helmholtz equation is separable [42], and, as stated in previous chapters, the geometrical properties of the Gaussian and Laguerre-Gauss beams suggest a relation with this coordinate system.

4.1 The spheroidal coordinate systems

The spheroidal coordinate systems are defined by confocal revolution hyperboloids and ellipsoids. If the revolution is around the major axis, the coordinate system is called prolate spheroidal, and if the revolution is done around the minor axis, it is called oblate spheroidal.

4.1.1 Oblate spheroidal coordinate system

The oblate spheroidal coordinates can be defined by the following transformation, relating the Cartesian coordinate system

$$
\begin{aligned}
x &= f\sqrt{1-\eta^2}\sqrt{1+\xi^2}\cos\phi, \\
y &= f\sqrt{1-\eta^2}\sqrt{1+\xi^2}\sin\phi, \\
z &= f\eta\xi,
\end{aligned}
\tag{4.1}
$$

where η is the angular coordinate, ranging from $[0, 1]$, ξ is the radial coordinate, ranging from $(-\infty, \infty)$, ϕ is the azimuth coordinate and f is the focal distance. The level surfaces are oblate ellipsoids for ξ constant and varying η and ϕ (figure 4.1), one sheet hyperboloids for η constant and varying ξ and ϕ (figure 4.3), and semi-planes for ϕ constant and varying η and ξ. These surfaces are shown in figure 4.5, where the red circle shows the focal circle, the blue line the rotation axis, and the orange dot the coordinate (ξ, η, ϕ). The oblate spheroidal coordinate system is related to the spherical system at the limit $f \to 0$.

4.1.2 Prolate spheroidal coordinate system

Among various representations, the prolate spheroidal coordinate system can be defined by the following transformation, relating the Cartesian coordinate system

$$
\begin{aligned}
x &= f\sqrt{1-\eta^2}\sqrt{\xi^2-1}\cos\phi, \\
y &= f\sqrt{1-\eta^2}\sqrt{\xi^2-1}\sin\phi, \\
z &= f\eta\xi,
\end{aligned}
\tag{4.2}
$$

where (x, y, z) correspond to the Cartesian components, η is the angular coordinate ranging from $[-1, 1]$, ξ corresponds the radial coordinate, ranging from $[1,\infty)$, ϕ is the usual azimuth coordinate and f is the focal distance of the conic surfaces. The associated level surfaces corresponds to prolate ellipsoids for ξ constant and varying η and ϕ (figure 4.2), two sheets hyperboloids for η constant and varying ξ and ϕ (figure 4.4), and semi-planes for ϕ constant and varying η and ξ. These surfaces are shown in figure 4.6 where the red dots shows the focal points, the blue line the rotation axis, and the orange dot the coordinate (ξ, η, ϕ). The prolate spheroidal coordinate system is related to the spherical coordinates at the limit $f \to 0$.

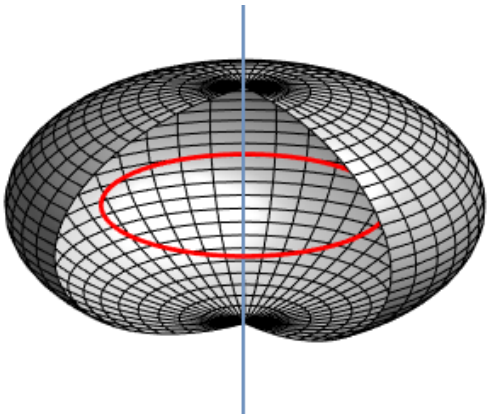

FIGURE 4.1: Oblate spheroid.

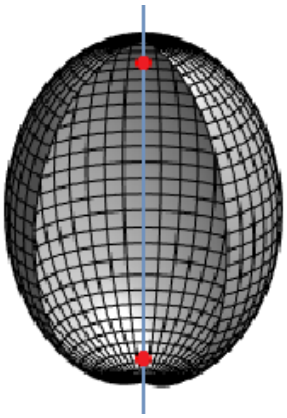

FIGURE 4.2: Prolate spheroid.

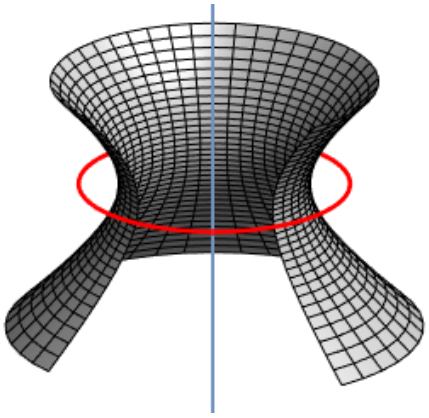

FIGURE 4.3: Hyperboloid of one sheet.

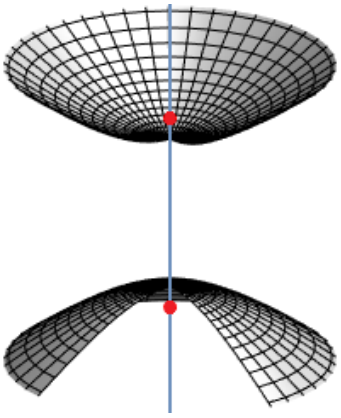

FIGURE 4.4: Hyperboloid of two sheets.

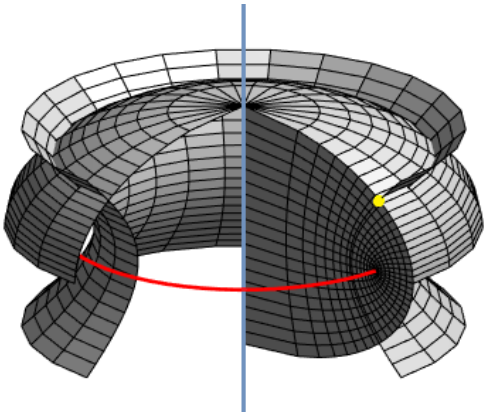

FIGURE 4.5: Constant coordinate surfaces for oblate coordinates.

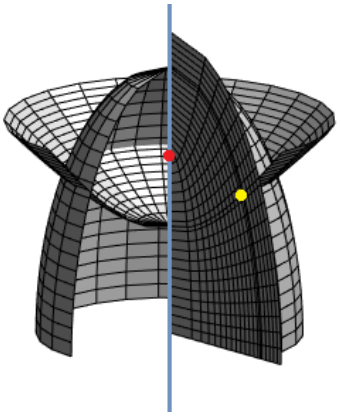

FIGURE 4.6: Constant coordinate surfaces for prolate coordinates.

4.2 The Helmholtz equation for spheroidal coordinates

The Helmholtz equation

$$\nabla^2 U(\vec{r}) + k^2 U(\vec{r}) = 0, \tag{4.3}$$

describes the propagation of waves in space. To solve equation (4.3) we need the expression of the ∇^2 operator in the spheroidal coordinates. This can be obtained from the equation

$$\nabla^2 \psi(q_1, q_2, q_3) = \frac{1}{h_1 h_2 h_3}\left(\frac{\partial}{\partial q_1}\left(\frac{h_2 h_3}{h_1}\frac{\partial \psi}{\partial q_1}\right) + \frac{\partial}{\partial q_2}\left(\frac{h_1 h_3}{h_2}\frac{\partial \psi}{\partial q_2}\right) + \frac{\partial}{\partial q_3}\left(\frac{h_1 h_2}{h_3}\frac{\partial \psi}{\partial q_3}\right)\right), \tag{4.4}$$

where h_i are the scale factors[41]. For the spheroidal coordinates, the scale factors are given by

$$\begin{aligned} h_\xi &= f\sqrt{\frac{\xi^2 - \eta^2}{\xi^2 \mp 1}}, \\ h_\eta &= f\sqrt{\frac{\xi^2 - \eta^2}{1 - \eta^2}}, \\ h_\phi &= f\sqrt{(\xi^2 \mp 1)(1 - \eta^2)}, \end{aligned} \tag{4.5}$$

where the upper sign is for the prolate and the lower for the oblate coordinates respectively. Thus, the Helmholtz equation can be written as

$$\left(\frac{\partial}{\partial \xi}\left((\xi^2 \mp 1)\frac{\partial}{\partial \xi}\right) + \frac{\partial}{\partial \eta}\left((1 - \eta^2)\frac{\partial}{\partial \eta}\right) + \frac{\xi^2 \mp \eta^2}{(\xi^2 \mp 1)(1 - \eta^2)}\frac{\partial^2}{\partial \phi^2}\right) U + c^2(\xi^2 \mp \eta^2)U = 0, \tag{4.6}$$

where $U = U(\xi, \eta, \phi)$ is the wave function, $c = fk$ is the spheroidicity parameter with f the focal distance and k the wave number, and the upper sign is for prolate coordinates and the lower for the oblate coordinates. By using separation of variables, the wavefunction can be written as $U = R(c;\xi)S(c;\eta)\Phi(\phi)$. The resultant set of equations is

$$\frac{d}{d\xi}\left((\xi^2 \mp 1)\frac{dR(c;\xi)}{d\xi}\right) - \left(\lambda_n^m - c^2\xi^2 + \frac{m^2}{\xi^2 \mp 1}\right)R(c;\xi) = 0, \tag{4.7}$$

$$\frac{d}{d\eta}\left((1 - \eta^2)\frac{dS(c;\eta)}{d\eta}\right) + \left(\lambda_n^m - c^2\eta^2 - \frac{m^2}{1 - \eta^2}\right)S(c;\eta) = 0, \tag{4.8}$$

$$\frac{d^2\Phi}{d\phi^2} + m^2\Phi = 0, \tag{4.9}$$

where the upper sign corresponds to the prolate system, while the lower sign to the oblate system, and λ_n^m is the eigenvalue of the differential equation. The azimuth function, Φ, is the same of the spherical and circular cylindrical coordinates, so that m must be an integer to have a continuous solution around the propagation axis.
As it was pointed by Flammer [43], both angular and radial equations of the spheroidal coordinates can be analyzed from one equation, this is:

$$\frac{d}{dz}\left((1-z^2)\frac{du}{dz}\right)+\left(\lambda_n^m+c^2z^2-\frac{m}{1-z^2}\right)u=0. \tag{4.10}$$

By applying coordinate transforms to (4.10) we recover the originally spheroidal equations. The transformations are: $c \to c$ and $z \to z$ for the oblate angular, $c \to c$ and $z \to iz$ for the oblate radial, $c \to ic$ and $z \to z$ for the prolate angular, and $c \to ic$ and $z \to -iz$ for the prolate radial.

4.3 The spheroidal functions

The spheroidal functions are some of the hardest functions to program, according to Zhang[44] this is due to the high numerical accuracy required for both the expansion coefficients and the eigenvalue λ_n^m, as well as to the singularities of the differential equation, that forces the use of different expansions for different regions. Even though the angular and radial spheroidal functions are the same over a complex space of their parameters, in order to have physical solutions, the angular and radial indexes n and m must be integers, and the arguments must be real or imaginary instead of full complex arguments. As described earlier, the parameter m must be integer to have continuous solutions encircling the propagation axis. In order to fulfill the finiteness boundary condition, that is, the existence of finite solutions at the singularities $\eta \to \pm 1$, the parameter n must be integer. This restricts the eigenvalues λ_n^m to a countable set indexed as $n = 0, 1...$ [45].

4.3.1 The angular spheroidal functions

The angular spheroidal equation can be written as:

$$\frac{d}{d\eta}\left((1-\eta^2)\frac{dS(c;\eta)}{d\eta}\right)+\left(\lambda_n^m(c)-c^2\eta^2-\frac{m^2}{1-\eta^2}\right)S(c;\eta)=0, \tag{4.11}$$

in the spherical limit, $c \to 0$, equation (4.11) becomes

$$\frac{d}{d\eta}\left((1-\eta^2)\frac{dS(\eta)}{d\eta}\right)+\left(\lambda_n^m(0)-\frac{m^2}{1-\eta^2}\right)S(\eta)=0. \tag{4.12}$$

Equation (4.12) is the Legendre differential equation, whose solutions are the Legendre functions $P_n^m(\eta)$ and $Q_n^m(\eta)$, where $\lambda_n^m(0) = n(n+1)$. A standard method of solution for differential equations is to use the limiting solutions as a basis of expansion for the general solution. For the angular spheroidal differential equation, this basis is conformed by the first and second Legendre functions that act as limiting solutions. The two linearly independent solutions to equation (4.11) are the spheroidal angular functions $S_n^{m(1,2)}(c;\eta)$. They can be written in terms of the latter expansions basis as

$$\begin{aligned} S_n^{m(1)}(c;\eta) &= \sum_{k_{even}=-\infty}^{\infty} d_k^{mn}(c) P_{n+k}^m(\eta), \\ S_n^{m(2)}(c;\eta) &= \sum_{k_{even}=-\infty}^{\infty} d_k^{mn}(c) Q_{n+k}^m(\eta), \end{aligned} \tag{4.13}$$

where the summations are only over even values of k. These are general solutions, and were studied for general m and n by Meixner [23]. By evaluating the solutions in equation (4.11), and using the properties of the Legendre functions, we obtain a three term recurrence relation

$$\alpha_k^{mn}(c) d_{k+2}^{mn}(c) + \left(\beta_k^{mn}(c) - \lambda_n^m(c)\right) d_k^{mn}(c) + \gamma_k^{mn} d_{k-2}^{mn}(c) = 0, \tag{4.14}$$

where

$$\begin{aligned} \alpha_k^{mn}(c) &= -\frac{c^2(k+m+n+1)(k+m+n+2)}{(2k+2n+3)(2k+2n+5)} \\ \beta_k^{mn}(c) &= (n+k)(n+k+1) - \frac{c^2}{2}\left(1 - \frac{4m^2-1}{(2n+2k-1)(2n+2k+3)}\right) \\ \gamma_k^{mn}(c) &= -\frac{c^2(k-m+n-1)(k-m+n)}{(2k+2n-3)(2k+2n-1)} \end{aligned} \tag{4.15}$$

The recurrence relation is the motive for having the sums running only for even values of k. By means of equation (4.14), we can obtain two formulas for the terms:

$$\frac{d_k^{mn}(c)}{d_{k+2}^{mn}(c)} = \frac{-\alpha_k^{mn}(c)}{\gamma_k^{mn}(c)\frac{d_{k-2}^{mn}(c)}{d_k^{mn}(c)} + \beta_k^{mn}(c) - \lambda_n^m(c)}, \tag{4.16}$$

$$\frac{d_k^{mn}(c)}{d_{k-2}^{mn}(c)} = \frac{-\gamma_k^{mn}(c)}{\alpha_k^{mn}(c)\frac{d_{k+2}^{mn}(c)}{d_k^{mn}(c)} + \beta_k^{mn}(c) - \lambda_n^m(c)}. \tag{4.17}$$

As described in the work of Fallon [24] the ratio $d_k^{mn}(c)/d_{k-2}^{mn}(c)$, for $k \to \pm\infty$ behaves like $-4k^2/c^2$ or $-c^2/4k^2$, being dominant or minimal respectively. As discussed and proved by [23], only minimal solutions are of interest, leading to convergent series, and

this only occurs for specific values of λ_n^m. To compute the ratios of terms, the ratio $d_{k-2}^{mn}(c)/d_k^{mn}(c)$ is set to zero for a large enough k. This term is then used as a starting point to calculate the recursion (4.16). The terms are then calculated by multiplication. The terms for negative k are calculated analogously.

By using this method, the coefficients are calculated up to a multiplicative constant, that is, the functions are not normalized. There are many normalization schemes for the angular functions, being the most used the Flammer scheme, in which the values of the first angular function $S_n^{m(1)}$ and its derivative at $\eta = 0$ are the same as the Legendre functions P. On the other hand, in the Meixner scheme, the integrals of the squared modulus of the Legendre function P and the first angular function $S_n^{m(1)}$ are set equal. In the Flammer normalization, the angular functions grow exponentially fast with increasing c. Since we are interested in the asymptotic approximation of large c (as it will be clear later), the normalization used in this work will be the one of the Meixner scheme, written as

$$\sum_{k_{even}=-\infty}^{\infty} d_k^{mm}(c)^2 \frac{2}{2k+2n+1}\frac{(k+m+n)!}{(k-m+n)!} = \frac{2}{2n+1}\frac{(n+m)!}{(n-m)!}. \tag{4.18}$$

Angular functions of the first kind with different parameters are shown in figures 4.7 and 4.8.

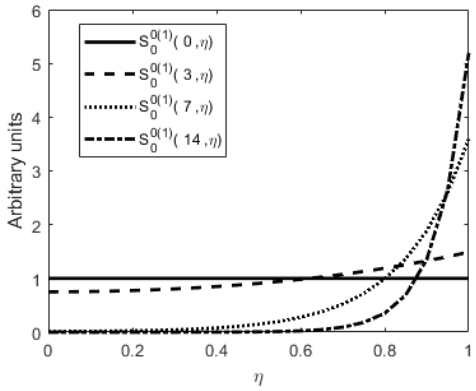

FIGURE 4.7: Oblate angular functions $S_0^{0(1)}(c;\eta)$.

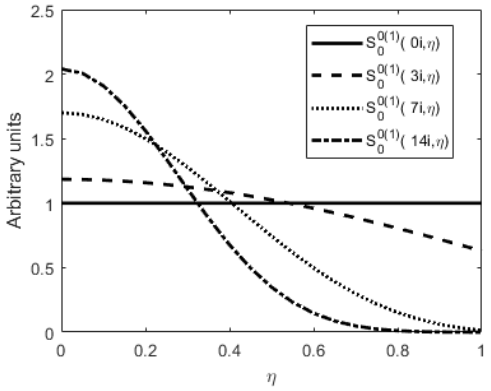

FIGURE 4.8: Prolate angular functions $S_0^{0(1)}(c;\eta)$.

When n and m are integer numbers, the expansion of the angular function of the first kind takes the form:

$$S_n^{m(1)}(c;\eta) = \sum_{k_{even}=m-n+\delta}^{\infty} d_k^{nm}(c) P_{n+k}^m(\eta), \tag{4.19}$$

where $\delta = (m+n) \mod 2$, due to the fact that the Legendre functions of the first kind are zero for $m > n$.

The expansion and computation of the angular function of the second kind $S_n^{m(2)}$ possesses additional details. By using upward recursion, defined in equation (4.16), the ratios turn out to be zero after $\alpha_k^{mn}(c)$ is zero at $k_{cut} = -n - m + \delta - 2$. Since the terms lower than k_{cut} in expansion (4.13) are functions of the upper terms, all the lower terms are infinitely small. The Legendre functions of the second kind become divergent for $n < -m$ and any value of η. However, the product of this diverging functions and the infinitely small expansion coefficients remains finite[23]. Thus, the expansion can be written as

$$S_n^{m(2)}(c;\eta) = \sum_{k_{even}=\infty}^{-n-m+\delta-2} \tilde{d_k}^{mn}(c) P_{-n-k-1}^m(\eta) + \sum_{k_{even}=-n-m+\delta}^{\infty} d_k^{mm}(c) Q_{n+k}^m(\eta) \tag{4.20}$$

The terms $\tilde{d_k}^{mn}(c)$ are slight different from $d_k^{mm}(c)$ terms. The former terms are calculated by using upward recursion up to the term $k = -n - m + \delta - 2$. The last term $\tilde{d}_{-n-m+\delta-2}$, is calculated as follows

$$\tilde{d_k}^{mn}(c) = -d_{k+2}^{mm}(c) \frac{\tilde{\alpha}_k^{mn}(c)}{\beta_k^{mn} - \lambda_n^m + \gamma_k^{mn} \frac{\tilde{d}_{k-2}{}^{mn}(c)}{\tilde{d_k}^{mn}(c)}} \tag{4.21}$$

where

$$\tilde{\alpha}_k^{mn}(c) = \frac{(-1)^{\delta+1} c^2}{(2m - 2\delta - 1)(2m - 2\delta + 1)}, \tag{4.22}$$

and the lower terms are then calculated by direct multiplication. Functions of the second kind with different parameters are shown in figures 4.9 and 4.10. As the Legendre functions of the second kind, the spheroidal angular functions of the second kind possesses singularities at $\eta = \pm 1$. In both spheroidal coordinate systems, the singularities are located at the z-axis.

The wronskian is used to evaluate two linearly independent solutions of a second order differential equation. The former is defined as $W = y_1 y_2' - y_1' y_2$. For the angular spheroidal differential equation, the wronskian is defined up to a multiplicative constant. Thus, the wronskian can be written as

$$W(S_n^{m(1)}(c;\eta), S_n^{m(2)}(c;\eta)) \propto \frac{1}{1-\eta^2}. \tag{4.23}$$

4.3.2 The radial spheroidal functions

The radial spheroidal differential equation

$$\frac{d}{d\xi}\left((\xi^2 - 1)\frac{df(\xi)}{d\xi}\right) - \left(\lambda_n^m(c) - c^2\xi^2 + \frac{m^2}{\xi^2 - 1}\right) f(\xi) = 0, \tag{4.24}$$

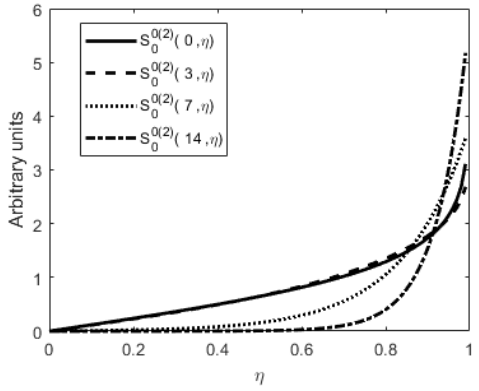

FIGURE 4.9: Oblate angular functions $S_0^{0(2)}(c;\eta)$.

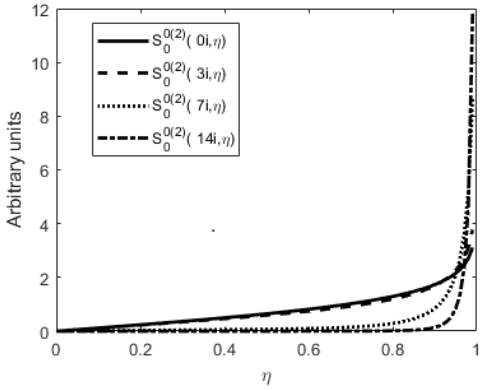

FIGURE 4.10: Prolate angular functions $S_0^{0(2)}(c;\eta)$.

has two regular singular points at $\xi = \mp 1$. When the two singularities are made coalesce, by performing transformations in equation (4.24), the resulting differential equation is the spherical Bessel equation. Thus, like in the case of the angular functions, in the radial case the appropriated expansion basis is conformed by the spherical Bessel functions $j_m(c\xi)$ and $y_m(c\xi)$. In this basis, the radial functions can be defined as

$$\begin{aligned} R_n^{m(1)}(c;\xi) &= (\xi^2-1)^{m/2}(c\xi)^{-m} \sum_{k_{even}=-\infty}^{\infty} a_k^{mn} j_{n+k}(c\xi), \\ R_n^{m(2)}(c;\xi) &= (\xi^2-1)^{m/2}(c\xi)^{-m} \sum_{k_{even}=-\infty}^{\infty} a_k^{mn} y_{n+k}(c\xi), \end{aligned} \tag{4.25}$$

where $j_n(x) = \sqrt{\pi/2x}\, J_{n+1/2}(x)$ and $y_n(x) = \sqrt{\pi/2x}\, N_{n+1/2}(x)$, where J and N denote the Bessel and Neumann functions. Two other radial functions are defined, in analogy with the Hankel functions.

$$\begin{aligned} R_n^{m(3)}(c;\xi) &= R_n^{m(1)}(c;\xi) + iR_n^{m(2)}(c;\xi), \\ R_n^{m(4)}(c;\xi) &= R_n^{m(1)}(c;\xi) - iR_n^{m(2)}(c;\xi). \end{aligned} \tag{4.26}$$

The standard normalization of the radial functions is defined by matching the asymptotic expansion for large ξ of the radial functions to the spherical Bessel functions. That is:

$$\begin{aligned} R_n^{m(1)}(c;\xi) &\sim \frac{1}{c\xi} \sin\left(c\xi - \frac{n\pi}{2}\right), \\ R_n^{m(2)}(c;\xi) &\sim \frac{1}{c\xi} \cos\left(c\xi - \frac{n\pi}{2}\right). \end{aligned} \tag{4.27}$$

With this normalization, the coefficients of the radial functions are

$$a_k^{mn}(c) = \frac{(-1)^{k/2}c^m}{\sum_{-\infty}^{\infty} d_k^{-m,n}(c)} d_k^{-m,n}. \tag{4.28}$$

Some important remarks are needed for the radial function of the second kind. In the oblate system, ξ is defined for all real numbers. However, the expansion on spherical Bessel functions of the second kind, is not useful for small arguments, since the increasing rate of the expansion basis is larger than the expansion coefficients decreasing rate, resulting in a divergent expansion for arguments close to zero. A standard method to avoid this problem consists in using the fact that radial and angular functions are the same functions over a complex space. This allows to calculate the radial function of the second kind as a function of the angular functions. The radial function of the second kind can be calculated through

$$R_n^{m(2)}(c;z) = \kappa_n^{m(2)}(c)\frac{(z^2-1)^{m/2}}{(-z-1)^{m/2}(z-1)^{m/2}}\left(\frac{\pi}{2}\frac{\sqrt{-z-1}}{\sqrt{z+1}}S_n^{m(1)}(z) + S_n^{m(2)}(z)\right), \tag{4.29}$$

where

$$\kappa_n^{m(2)}(c) = \frac{2^{2n+1}(-1)^(1+n)c^{-m-n-1}}{\Gamma(n+m+1)}\frac{\sum_{k=0}^{\infty}\frac{(-1)^k a_{2k}^{mn}(c)}{k!\,\Gamma\left(-k-n+\frac{1}{2}\right)}}{\sum_{k=0}^{\infty}\frac{(-1)^k d_{-2k}^{mn}(c)}{k!\,\Gamma\left(-k-n+\frac{3}{2}\right)}}. \tag{4.30}$$

$\kappa_n^{m(2)}(c)$ is called joining factor. Some radial functions are shown in figures through 4.11 to 4.14.

As in the spheroidal angular functions, the spheroidal radial functions can be evaluated by using the wronskian, that is

$$W(R_n^{m(1)}(c;\xi), R_n^{m(2)}(c;\xi)) = \frac{1}{c(\xi^2-1)}. \tag{4.31}$$

4.3.3 The spheroidal eigenvalue

As described in previous sections, the spheroidal functions only converge for the eigenvalues λ_n^m of the spheroidal differential equations. As the eigenvalues appear in the expansion coefficients, it is very important to have very high accuracy in their computation. There are many methods to do this, for instance, by using eigenvalues of tridiagonal matrices, to use a zero finding algorithm over a continuous fraction, by using asymptotic methods for the behavior of the angular differential equation, among others. In this work, we calculate the eigenvalues of a tridiagonal matrix, being this a direct

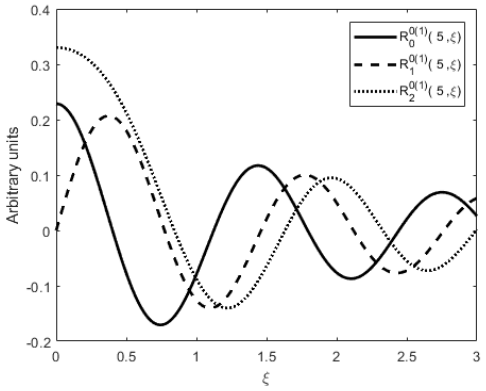

FIGURE 4.11: Oblate radial functions $R_n^{0(1)}(-5i;\eta)$.

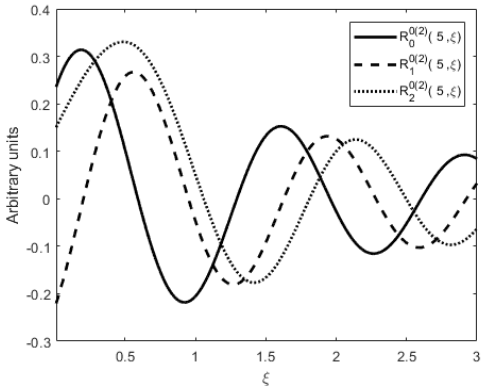

FIGURE 4.12: Oblate radial functions $R_n^{0(2)}(-5i;\eta)$.

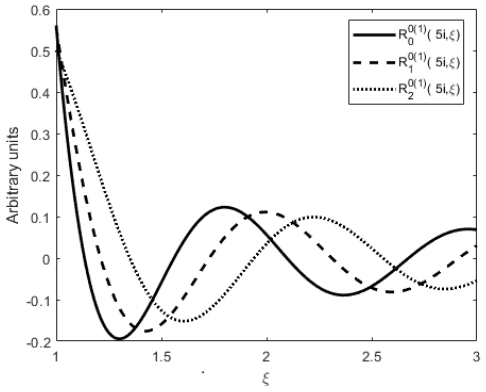

FIGURE 4.13: Prolate radial functions $R_n^{0(1)}(5;\eta)$.

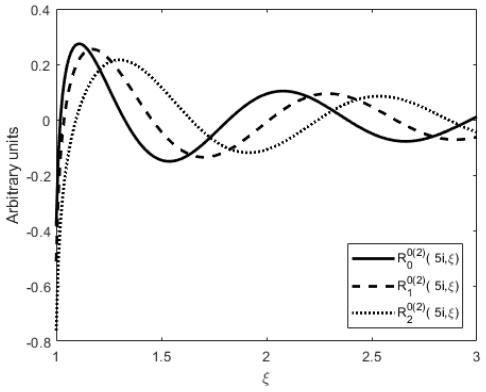

FIGURE 4.14: Prolate radial functions $R_n^{0(2)}(5;\eta)$.

approach. The three terms recurrence relation (4.14), can be considered as an infinite tridiagonal matrix

$$\begin{pmatrix} \bullet & \bullet & \bullet & 0 & 0 & 0 & 0 & 0 & 0 \\ 0 & \bullet & \bullet & \bullet & 0 & 0 & 0 & 0 & 0 \\ 0 & 0 & \gamma_k & \beta_k & \alpha_k & 0 & 0 & 0 & 0 \\ 0 & 0 & 0 & \gamma_{k+2} & \beta_{k+2} & \alpha_{k+2} & 0 & 0 & 0 \\ 0 & 0 & 0 & 0 & \gamma_{k+4} & \beta_{k+4} & \alpha_{k+4} & 0 & 0 \\ 0 & 0 & 0 & 0 & 0 & \bullet & \bullet & \bullet & 0 \\ 0 & 0 & 0 & 0 & 0 & 0 & \bullet & \bullet & \bullet \end{pmatrix} \begin{pmatrix} \bullet \\ \bullet \\ d_{-2} \\ d_0 \\ d_2 \\ \bullet \\ \bullet \end{pmatrix} = \lambda_n^m(c) \begin{pmatrix} \bullet \\ \bullet \\ d_{-2} \\ d_0 \\ d_2 \\ \bullet \\ \bullet \end{pmatrix}, \quad (4.32)$$

where the matrix starts at $k = -m - n + \delta$. From the Sturm-Liouville theory, since $n \geq m \geq 0$ are integers, there exists a countably infinite set of strictly increasing eigenvalues [46]. This method generates a highly accurate set of eigenvalues.

4.3.4 The asymptotics of the angular equation for large c

The angular function possesses two asymptotic expansions, the prolate asymptotic , $c \to -i\infty$, and the oblate asymptotic, $c \to \infty$.
In the prolate limit, by performing the change of coordinates $x = \sqrt{2c}\eta$, and letting the angular function take the form $S_n^{m(1)}(c;\eta) = (1-\eta^2)^{m/2} u_n^m(c;x)$, the angular spheroidal equation is written as

$$\left(1 - \frac{x^2}{-2ic}\right)\frac{d^2u_n^m(c;x)}{dx^2} - \frac{(m+1)x}{-ic}\frac{du_n^m(c;x)}{dx} + \left(\frac{\lambda_n^m(c) - m(m+1)}{-2ic} - \frac{1}{4}x^2\right)u_n^m(c;x) = 0. \tag{4.33}$$

By taking $c \to -i\infty$, equation (4.33) reduces to

$$\frac{d^2u_n^m(c;x)}{dx^2} + \left(\frac{\lambda_n^m(c)}{2c} - \frac{1}{4}x^2\right)u_n^m(c;x) = 0. \tag{4.34}$$

Equation (4.34) matches the differential equation for the parabolic cylinder functions $D_r(z)$ [47], where $r = n - m$, and thus the eigenvalue takes the asymptotic form of $\lambda_n^m(c) \to (2n - 2m + 1)c$. Then, the prolate asymptotic can be written as

$$S_n^{m(1)}(c;\eta) \sim (1-\eta^2)^{m/2}\, 2^{-(n-m)/2}\, e^{-c\eta^2/2}\, H_{n-m}(\sqrt{c}\eta). \tag{4.35}$$

With the asymptotic expansion, a new basis for the evaluation of the differential equation can be defined, this produces a five terms recurrence relation, and can also be used to expand the eigenvalue.

In the oblate limit, the angular functions are compressed towards the lower and upper limits of its domain, that is, $\eta = \pm 1$. Thus, the expansion can be done for $\eta > 0$ and use parity for the other half of the interval. By using the coordinate transform $x = 2c(1-\eta)$ and having the angular function take the form $S_n^{m(1)}(c;\eta) = (1-\eta^2)^{m/2}\, e^{-x/2} u_n^m(c;x)$, the angular equation takes the form[48]

$$\begin{aligned} &x\left(1 - \frac{x}{4c}\right)\frac{d^2u_n^m(c;x)}{dx^2} + \left((m+1)\left(1 - \frac{x}{2c}\right) - x\left(1 - \frac{x}{4c}\right)\right)\frac{du_n^m(c;x)}{dx} \\ &+ \left(\frac{\left(c^2 + \lambda_n^m(c) - m(m+1)\right)}{4c} - \frac{1}{2}(m+1)\left(1 - \frac{x}{2c}\right)\right)u_n^m(c;x) = 0. \end{aligned} \tag{4.36}$$

By taking the oblate limit $c \to \infty$, equation (4.36) becomes

$$x\frac{d^2}{dx^2}u_n^m(c;x) + (m+1-x)\frac{d}{dx}u_n^m(c;x) + \frac{\left(c^2 - \lambda_n^m(c) + 2c(m+1)\right)}{4c}u_n^m(c;x) = 0. \tag{4.37}$$

Equation (4.37) matches the associated Laguerre equation. The Laguerre polynomial $L_s^m(x)$ has s zeros for $z > 0$. On the other hand, in the domain $0 \leq \eta \leq 1$, like the associated Legendre polynomial P_n^m, $S_n^{m(1)}(c;\eta)$ has $(n-m)/2$ zeros for $n-m$ even, and $(n-m-1)/2$ zeros for $n-m$ odd. This can also be written as $(n-m-\delta)/2$ zeros, where $\delta = (n-m) \mod 2$. From this considerations, the order of the Laguerre polynomial in the asymptotic expansion is $s = (n-m-\delta)/2$. Therefore, the asymptotic expansion for the oblate angular function is

$$S_n^{m(1)}(c;\eta) \sim (1-\eta^2)^{m/2}\, e^{-c(1-\eta)} L^m_{(n-m-\delta)/2}\left(2c(1-\eta)\right). \tag{4.38}$$

In the plane $z = 0$, the relation between η and ρ can be written as $\rho = f\sqrt{1-\eta^2}$. By solving this relation for η, expanding in powers and taking the lower terms, equation (4.38) can be written as

$$S_n^{m(1)}(c;\eta) \sim \left(\frac{\rho}{f}\right)^m \exp\left(-\frac{k\rho^2}{2f}\right) L^m_{(n-m-\delta)/2}\left(\frac{k\rho^2}{f}\right), \tag{4.39}$$

which matches the form of the Laguerre-Gauss beam at its waist plane. Furthermore, the eigenvalue takes the following asymptotic form $\lambda_n^m(c) \sim c(-c+2\delta+4m-2n+2)$, which is equal for $n-m$ and $n-m+1$ at $n-m$ even. From this asymptotic form, another basis for the expansion of the angular function can be defined in terms of associated Laguerre polynomials, with a three term recurrence relation [24].

4.4 The relation between the spheroidal wavefunction and the Laguerre-Gauss beam

Throughout literature, it can be found several methods that has been used to obtain non paraxial beams with properties similar to those of the Gaussian beam, Laguerre-Gauss and Hermite Gauss beams among others. For instance, by using a point source in a complex position of space, and using the coordinates to obtain properties of the solution, in the case of spheroidal coordinates, the solution is given in terms of the associated Legendre functions [49][50][51][52] instead of the spheroidal wavefunctions. In the work of Rodriguez-Chávez (2004) [9], it is presented a unified theory on the propagation of paraxial and non-paraxial beams, thorough a connection between the paraxial Laguerre-Gauss beam and the non-paraxial spheroidal wavefunctions. In this section, that connection is described briefly. As it was described in previous chapters, the spot size of a Gaussian beam takes the geometric form of a hyperbola. The latter is a level curve of the oblate spheroidal angular coordinate system. Using this fact, a spheroidal coordinate system, defined by the spheroidal parameter c can be defined

univocally for a Gaussian beam. This relation is shown in figure 4.15. In SI units, the

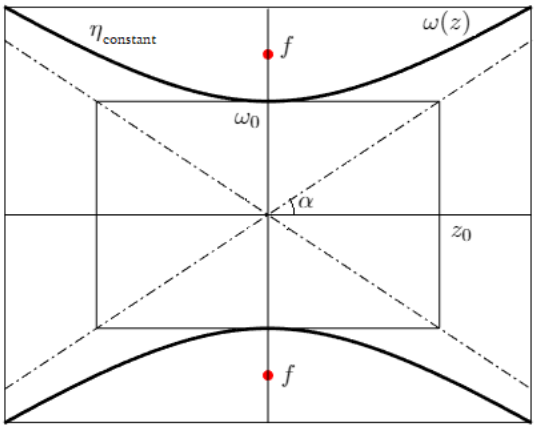

FIGURE 4.15: Spheroidal coordinate system and the Gaussian beam.

spot size of a Gaussian beam takes the form:

$$\omega(z) = \omega_0 \sqrt{1 + \frac{z^2}{z_0^2}}, \tag{4.40}$$

which can be written in canonical form as

$$\frac{\omega(z)^2}{\omega_0^2} - \frac{z^2}{z_0^2} = 1. \tag{4.41}$$

The angle of the asymptote of the hyperbola (4.40) is given by

$$\tan(\alpha) = \frac{\omega_0}{z_0}, \tag{4.42}$$

where ω_0 is the waist size and z_0 is the Rayleigh length. For an hyperbola, given the real and imaginary axes, which are ω_0 and z_0 respectively in equation (4.41), the focal distance f can be calculated as $f^2 = \omega_0^2 + z_0^2$. Using this relation and rearranging equation (4.42) we obtain

$$f^2 = \frac{c^2}{k^2} = \omega_0^2 \csc^2(\alpha). \tag{4.43}$$

By using $z_0 = k\omega_0^2/2$ in equation (4.43) and solving for the waist width

$$\omega_0 = \frac{\sqrt{2\left(\sqrt{1+c^2} - 1\right)}}{k} \tag{4.44}$$

This equation is the bridge that connects the paraxial Gauss beam and the non-paraxial propagation theory, relating a spheroidal coordinate system to a paraxial beam. It

remains to define a threshold for the paraxial and non-paraxial behavior. According to Siegman[3], the maximum diffraction angle for the paraxial beam approximation is approximately 30° or $\pi/6$ radians. By using equation (4.43) and $\tan(\alpha) = \omega_0/z_0 = 2/k\omega_0$, an expression relating the angle of divergence at ω_0 and the elliptic parameter c is obtained

$$c = \frac{2}{\tan(\alpha)\sin(\alpha)}. \tag{4.45}$$

By using the maximum diffraction angle $\alpha = \pi/6$ we obtain $c \sim 7$. This is an important result, for $c < 7$ it is expected a non-paraxial, highly diverging wavefield, where the limit $c = 0$ corresponds to a spherical wave. On the other hand, for $c \gg 7$ it is expected a highly paraxial wave.

4.4.1 The spheroidal beam

We are interested in a wavefield that, for large values of c, behaves asymptotically as a Laguerre-Gaussian beam. As it was shown in section 4.3.4, the angular function of the first kind $S_n^{m(1)}$, is the one that presents the desired behavior. For the radial function, we are interested in a solution which has the form of an outgoing wave in order to satisfy the Sommerfeld radiation condition. From equation (4.27), the asymptotic behavior of $R_n^{m(3)}(c;\xi)$ for large c,takes the form

$$R_n^{m(3)}(\xi) \sim \frac{1}{c\xi}\exp\left(i\left(c\xi - \frac{n\pi}{2}\right)\right), \tag{4.46}$$

which satisfies the radiation condition. Then, the spheroidal beam takes the form

$$\psi_n^{m(1)}(c;\xi,\eta,\phi) = S_n^{m(1)}(c;\eta)R_n^{m(3)}(c;\xi)\,e^{im\phi}. \tag{4.47}$$

The angular function $S_n^{m(1)}$ describes the transverse profile of the wavefunction, on the other hand, the radial function $R_n^{m(3)}$ describes the characteristics through propagation, that is, the Guoy phase shift, the wavefront and the intensity change over propagation.

4.4.2 Comparison for the spheroidal beam and the Gaussian beam

We are interested in the behavior of the spheroidal beams in the regimes defined by the equation (4.45) at the maximum diffraction angle, that is, the non-paraxial and the paraxial regimes, in comparison with the Gauss beam. In order to do so, a brief analysis on the properties of the spheroidal coordinates is useful. The level surfaces of the variable η are one sheet hyperboloids, which away from the focal plane $z = 0$ are approximately cones, this is due to the relation of the spheroidal coordinate systems

and the spherical coordinate system, that is, for the angular η coordinate, away from the focal plane, $\eta \sim \sin(\theta)$, where θ is the polar angle of the spherical coordinates. This relation is illustrated in figure 4.16. From that behavior, the transverse profile during propagation and the transverse profile at the focal plane are related up to a scaling factor. The level surfaces of the radial coordinate ξ are oblate ellipsoids with focal distance f. Away from the origin, the ellipsoids take the form of spheres with a radius of $r \sim f\xi$. This is illustrated in figure 4.17. From that, and away from the origin, the wavefronts described by the radial functions are almost spherical. The behavior described earlier for the angular and radial coordinates describe the behavior of the spheroidal beams. The Gauss beam, though not directly from the coordinates, also follows a similar behavior, that is, the transverse profile during propagation and the profile at the focal plane $z = 0$ are related by a scaling factor, and the wavefront of the Gauss beam, follows the paraxial approximation of the spherical wavefront. In the next figures, a comparison of the properties of the spheroidal and Gaussian beams are illustrated over the different regimes: non paraxial, the threshold and approximately paraxial.

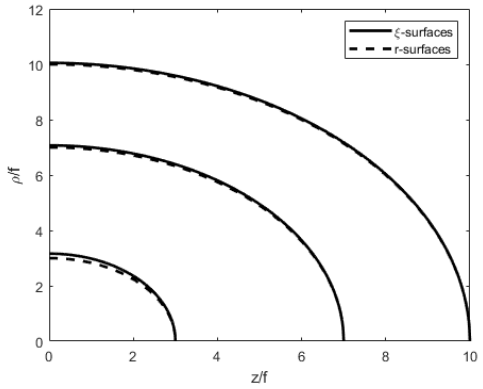

FIGURE 4.16: ξ-level surfaces and spherical radial r-level surfaces.

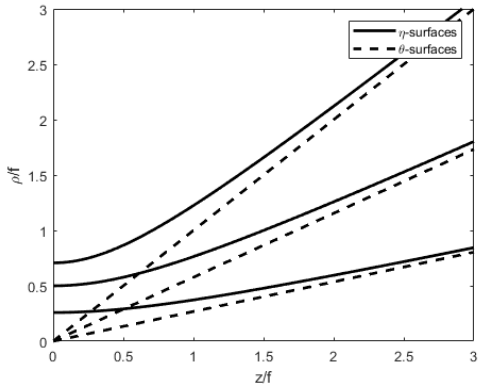

FIGURE 4.17: η-level surfaces and spherical polar angle θ-level surfaces.

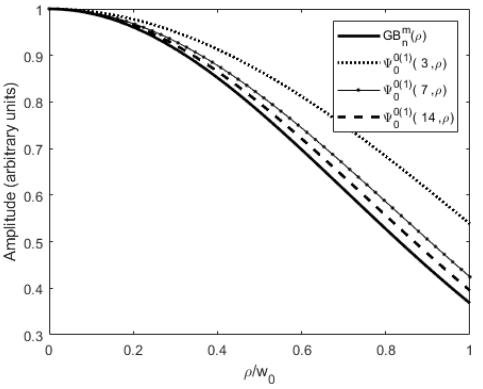

FIGURE 4.18: Transverse intensity of Gaussian and spheroidal beams.

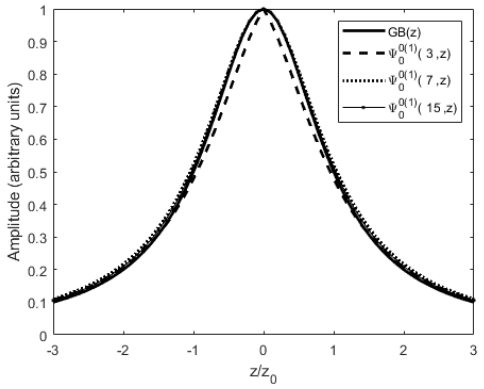

FIGURE 4.19: Longitudinal intensity of Gaussian and spheroidal beams.

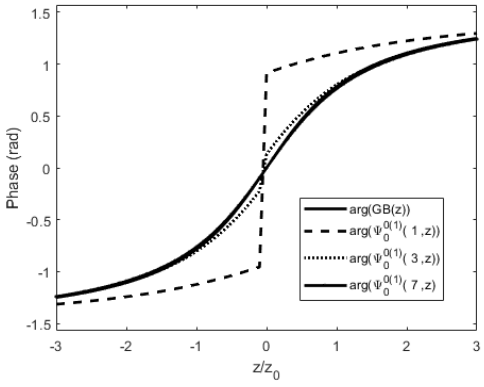

FIGURE 4.20: Phase shift of Gaussian and spheroidal beams.

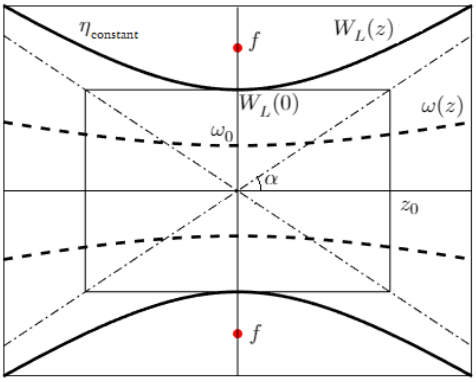

FIGURE 4.21: Spheroidal coordinate system and Laguerre-Gauss beam.

4.5 Paraxiality threshold for the spheroidal beams

An important result from previous sections is equation (4.45), which represents a threshold that separates the paraxial and non-paraxial behavior for the spheroidal beam with indices $n = m = 0$. This threshold is important as it allows to compare the Gaussian and the spheroidal beams. Given that the spheroidal beams behave asymptotically, for large values of the spheroidicity parameter c, as the Laguerre-Gauss beams, a general paraxiality threshold is needed for higher values of n, m. This can be obtained by using the spot size of the Laguerre-Gauss beams and its hyperbolic behavior as well as the properties of the spheroidal coordinates.

The spot size of the Laguerre-Gauss beam, $W_L(z) = \sqrt{2n+m+1}\,\omega(z)$, is illustrated in figure 4.21. It can be written in the canonical form of a hyperbola:

$$\frac{W_L^2(z)}{W_L^2(0)} - \frac{z^2}{z_0^2} = 1. \tag{4.48}$$

where $W_L(0) = \sqrt{2n+m+1}\,\omega_0$ is the waist size of the Laguerre-Gauss beam and z_0 is the Rayleigh length. Analogously to the previous section, the general relation for the divergence angle and the spheroidal parameter takes the form

$$c = \frac{2(2n+m+1)}{\tan(\theta)\sin(\theta)}, \tag{4.49}$$

which, using the maximum diffraction angle θ of a paraxial beam, $\theta \sim \pi/6$, can be written as

$$c = 4\sqrt{3}(2n+m+1) \approx 7(2n+m+1). \tag{4.50}$$

In the next table some values for c are calculated, where the indices are the associated Laguerre-Gauss beam indices.

Threshold values for multiple indices											
m \ n	0	1	2	3	4	5	6	7	8	9	10
0	7	21	35	48	62	76	90	104	118	132	145
1	14	28	42	55	69	83	97	111	125	139	152
2	21	35	48	62	76	90	104	118	132	145	159
3	28	42	55	69	83	97	111	125	139	152	166
4	35	48	62	76	90	104	118	132	145	159	173
5	42	55	69	83	97	111	125	139	152	166	180
6	48	62	76	90	104	118	132	145	159	173	187
7	55	69	83	97	111	125	139	152	166	180	194
8	62	76	90	104	118	132	145	159	173	187	201
9	69	83	97	111	125	139	152	166	180	194	208
10	76	90	104	118	132	145	159	173	187	201	215

The threshold value obtained for the Gaussian beam with $m = 0$ and $n = 0$ is in accordance with reference [9].

By solving equation (4.50) for the angle θ, and using the divergence angle of the hyperbola (4.48), we obtain the relation of the spheroidal coordinates and the Laguerre-Gauss beam,

$$\omega_0 = \frac{\sqrt{2}\sqrt{\sqrt{c^2 + (2n + m + 1)^2} - (2n + m + 1)}}{k}. \tag{4.51}$$

With equation (4.51) an univocal relation is defined for the Laguerre-Gauss and the spheroidal beams. These results will be used in the next chapter.

Chapter 5

An alternative second solution for the spheroidal equation

As covered in previous chapters, second solutions to differential equations describing the transverse profile of structured wavefields are important in the theory of propagation of beams, as they may contain physical meaning, and can explain phenomena such as the self healing [19] [20] [22]. In the case of the spheroidal functions, there has been few studies on the angular function of the second kind, aside from being used as a mean to calculate the radial function of the second kind. This chapter describes a method to obtain a second solution that behaves asymptotically as the Laguerre function of the second kind X_n^m described in chapter 3.
In this chapter n and m denote the radial and azimuthal indices of the Laguerre-Gauss beam respectively, while m and s the spheroidal indexes, where $s = m + 2n - \delta$, and $\delta = (s - m) \mod 2$.

5.1 The spheroidal angular function of the second kind

The spheroidal angular function of the first kind behaves asymptotically as an associated Laguerrre polynomial, times a Gaussian envelope for large values of c, as it was obtained in equation (4.39). We are interested in a second solution to the angular equation that behaves asymptotically as the Laguerre function of the second kind X_n^m times the same Gaussian envelope of the previous case. In figures 5.1 and 5.2 it is shown the behavior of the angular functions of the first and second kind as the spheroidicity parameter c increases.

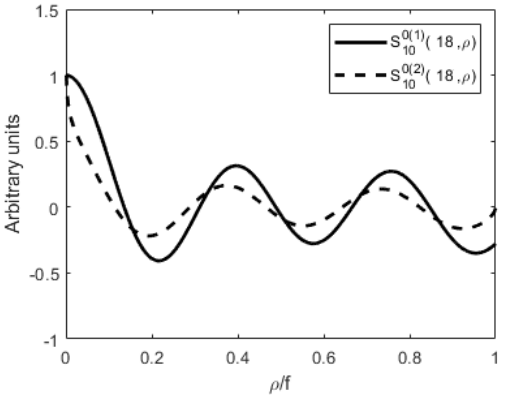

FIGURE 5.1: Angular functions $S_s^{m(1)}(-18i,\rho)$ and $S_s^{m(2)}(-18i,\rho)$.

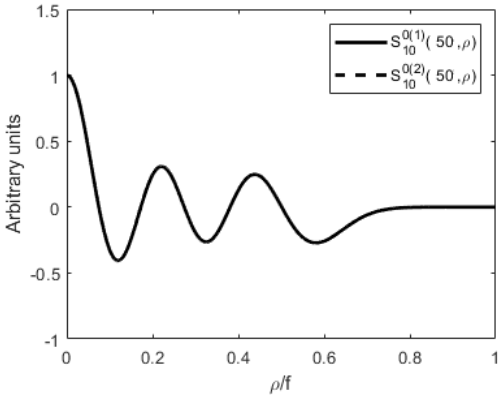

FIGURE 5.2: Angular functions $S_s^{m(1)}(-50i,\rho)$ and $S_s^{m(2)}(-50i,\rho)$.

The amplitude of the angular functions in figures 5.1 and 5.2 is normalized for visualization purposes. This is due to the fact that the Angular function of the second kind grows exponentially fast in comparison with the angular function of the first kind, so that with large enough spheroidicity parameter c, $S_s^{m(2)}$ might present numerical overflow, that is, numbers that are not representable in double-precision arithmetic. It can also be observed numerically that as the spheroidicity parameter increases, the zeros of the angular functions of the second kind gets closer to the zeros of the angular function of the first kind. This may be due to the fact that the $P_s^m(\eta)$ elements in the expansion of the angular functions of the second kind (4.20) get closer to the ones of $S_s^{m(1)}$ and grow faster than the $Q_s^m(\eta)$ elements, for increasing c. At first glance we could use the angular functions of the first and second kind to build Hankel like functions of the form

$$\begin{aligned} F_s^{m(1)}(c;\eta) &= S_s^{m(1)}(c;\eta) + iS_s^{m(2)}(c;\eta), \\ F_s^{m(2)}(c;\eta) &= S_s^{m(1)}(c;\eta) - iS_s^{m(2)}(c;\eta). \end{aligned} \tag{5.1}$$

Those angular functions in equation (5.1) do not provide a smooth envelope for $S_s^{m(1)}$ and $S_s^{m(2)}$ even after normalization, like in the case of Hankel and Hankel-Laguerre functions nor do they present the expected asymptotic behavior for a Hankel function. This is shown in figures 5.3 to 5.6 for $F_s^{m(1)}(c;\eta)$.

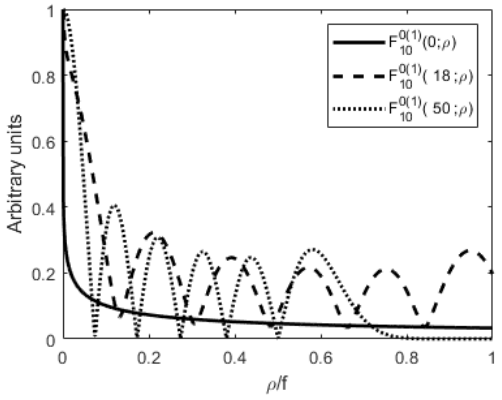

FIGURE 5.3: $|F_{10}^{0(1)}(c;\eta)|$ for increasing c.

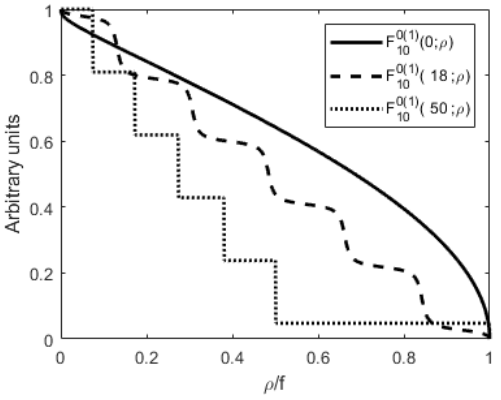

FIGURE 5.4: $F_{10}^{0(1)}(c;\eta)$ phase for increasing c.

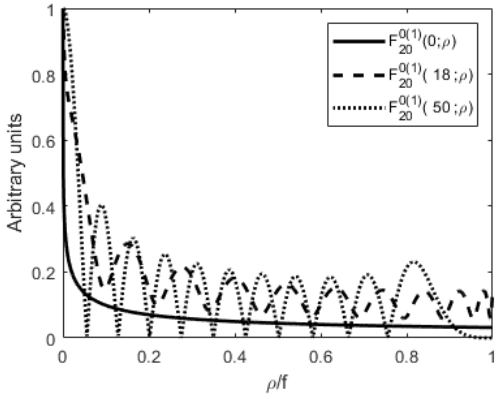

FIGURE 5.5: $|F_{20}^{0(1)}(c;\eta)|$ for increasing c.

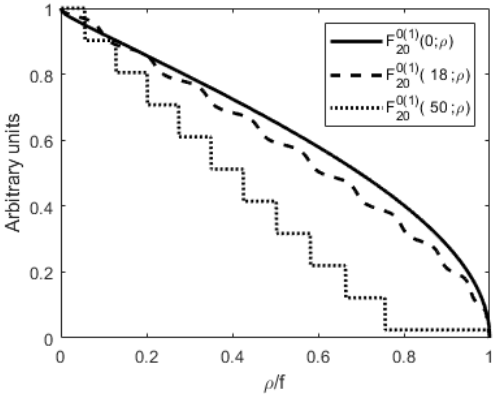

FIGURE 5.6: $F_{20}^{0(1)}(c;\eta)$ phase for increasing c.

Furthermore, as it was shown in the previous chapter, we look for a second solution to the angular equation that behaves asymptotically as the associated Laguerre function of the second kind X_n^m. In the work of Fallon [53] it is shown that the angular function of the second kind $S_s^{m(2)}$ behaves asymptotically as the angular function of the first kind $S_s^{m(1)}$(for large and fixed values of c and η respectively), with the radial index s displaced to $s+1$ or $s-1$ depending on whether $s-m$ is even or odd, respectively. Thus, the first and the second angular functions are not a suitable set to build a Hankel like angular function. On the other hand, the eigenvalue of the oblate spheroidal differential equations is equal for s and $s+1$ or $s-1$, that is, the eigenvalue is degenerate, forcing the angular function of the second kind to behave asymptotically as the angular function of the first kind [53].

5.2 Building an alternative second angular function

From the last section, it can be concluded that by increasing the spheroidicity parameter c, the angular function of the second kind $S_s^{m(2))}$ behaves asymptotically as the angular function of the first kind $S_s^{m(1))}$ for fixed values of η.
Much work has been done on the spheroidal functions, and many basis for expansions have been proposed and used as shown in reference [44]. Nevertheless, not much work has been done to investigate asymptotic representations of either $S_s^{m(2)}$ or any other linearly independent solution to $S_s^{m(1)}$, so we have to implement a numerical procedure to obtain a suitable second solution to the angular equation. Defining an angular function of the second kind is a complicated task from both theoretical and numerical standpoint. In this work, our numerical approach is to use the properties of the associated Laguerre equation solutions as starting points to approximate the new angular function.
We will build an alternative second angular function, namely SX_s^m, by considering it as a linear combination of $S_s^{m(1)}$ and $S_s^{m(2)}$, that is

$$SX_s^m(c;\eta) = c_1 S_s^{m(1)}(c;\eta) + c_2 S_s^{m(2)}(c;\eta). \tag{5.2}$$

From the deduction of equation (4.39), it is clear that to obtain a good approximation of the coefficients of equation (5.2), we have to use the region around the propagation axis ($\rho \sim 0$), where the angular function of the first kind is closer to the Laguerre-Gauss beam transverse profile, and $SX_s^m(c;\eta)$ is expected to be closer to the second solution X_n^m sector of the Hankel-Laguerre waves described in equation (3.31).
The first step in every attempt to obtain $SX_s^m(c;\eta)$ is to normalize $S_s^{m(1)}(c;\eta)$ in accordance to the Laguerre-Gauss beam. This last, in SI units, implies

$$R_s^{m(3)}(c;\xi=0) = 1, \tag{5.3}$$

and

$$\begin{aligned} S_s^{m(1)}(c;\eta_0) &= S_s^{m(1)}\left(c;\sqrt{1-\left(\frac{\rho_0^2}{f^2}\right)}\right), \\ &= \sqrt{\frac{2n!}{\pi(n+m)!}}\left(\frac{\sqrt{2}\rho_0}{\omega_0}\right)^m L_n^m\left[\frac{2\rho_0^2}{\omega_0^2}\right] e^{-\rho_0^2/\omega_0^2} \end{aligned} \tag{5.4}$$

where ρ_0 is the position of the maximum of the amplitude closest to the propagation axis, η_0 its corresponding angular coordinate and ω_0 is defined through equation (4.51). The azimuth dependent terms are set aside by taking $\theta = 0$, as well as the z dependent terms by working in the plane $z = 0$.

As a starting point, we want that $SX_s^m(c;\eta)$ approximate to the Second Laguerre solution X_n^m, defined in the section 3.2, at the neighborhood of the propagation axis.
The first proposed method is to use two random points in the neighborhood of $\rho \sim 0$ and use equation (5.2) to solve for c_1 and c_2. This is a poor approximation, and the results depend on c, as well as on the initial points.
This approximation can be improved by using the least squares method. The latter to minimize the difference of the Laguerre function of the second kind X_n^m and $SX_s^m(c;\eta)$ by variations over c_1 and c_2. This can be written as

$$\min\left(\sum_{k=1}^{k_{max}}\left(XL_n^m(\rho_k)-(c_1S_s^{m(1)}(\rho_k)+c_2S_s^{m(2)}(\rho_k))\right)^2\right), \tag{5.5}$$

where k is an index counting over the discrete points where the functions are sampled and ρ_K is its corresponding position, XL_n^m is the Laguerre function of the second kind, $S_s^{m(1,2)}$ are the standard angular solutions in the same conditions of equation (5.4). This method provides an approximation to the second solution which is bad for low values of c, but steadily improving with increasing c. Nevertheless, this method is computationally expensive, as it may require more than one optimization depending on the initial values of c_1 and c_2. Besides, given that the least squares method uses the first derivative criterion, a possible solution can turn out to be a saddle point for the variables (c_1, c_2). This is specially problematic for high radial and angular indices n and m, where this method is inefficient.
In order to improve the approximation of $SX_s^m(c;\eta)$, and avoid the least squares method problems, a geometric approach is used instead. The latter consists in using the relative position of the zeros of the solutions to the associated Laguerre equation, to obtain the position of the first zeros of the spheroidal functions, this can be expressed as

$$\frac{Z_{LG}}{Z_{XL}}=\frac{Z_{S1}}{Z_{SX}}, \tag{5.6}$$

where the Z terms are the position of the first zero, shown in figure 5.7. By using the relation (5.6) we obtain the position of the first zero of $SX_n^m(c;\eta)$. This can be written as

$$Z_{SX}=Z_{XL}\frac{Z_{S1}}{Z_{LG}}. \tag{5.7}$$

For convenience, equation (5.2) can be written as

$$SX_s^m(c;\eta)=c_2\left(S_s^{m(1)}(c;\eta)+c_1S_s^{m(2)}(c;\eta)\right), \tag{5.8}$$

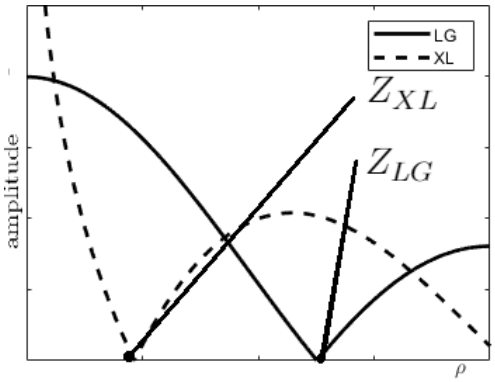

FIGURE 5.7: Zero points in the paraxial solutions

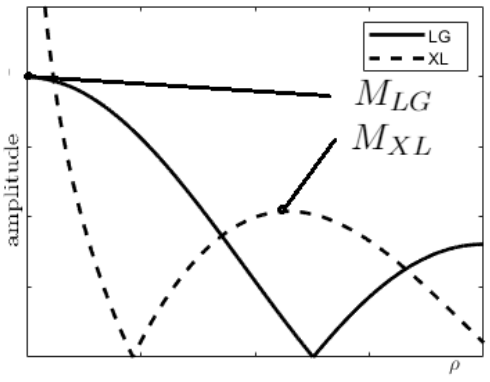

FIGURE 5.8: Normalization points in paraxial solutions

where c_1 defines the position of the zero at (5.7) and c_2 the normalization. By using equations (5.7) and (5.8), c_1 is obtained as

$$c_1 = -\frac{S_s^{m(1)}(c; Z_{SX})}{S_s^{m(2)}(c; Z_{SX})}. \tag{5.9}$$

If we use a normalization different to the one defined through (5.3) and (5.4), the normalization of $SX_s^m(c;\eta)$ can be obtained from

$$\frac{M_{LG}}{M_{XL}} = \frac{M_{S1}}{M_{SX}}, \tag{5.10}$$

where the M terms represent the amplitude of the first maxima of the Laguerre and spheroidal functions as illustrated in figure 5.8.

Otherwise, by using the normalization defined in (5.3) and (5.4), equation (5.10) reduces to

$$M_{XL} = M_{SX}. \tag{5.11}$$

By using equation (5.8) and (5.11), we obtain c_2 as

$$c_2 = \frac{M_{XL}}{S_s^{m(1)}(c; \rho_{M_{XL}}) + c_1 S_s^{m(2)}(c; \rho_{M_{XL}})}, \tag{5.12}$$

where $\rho_{M_{XL}}$ is the position of the maximum M_{XL}. This method to obtain c_1 and c_2 is computationally friendly, and also does not possess the least squared method problems described earlier. It is computationally cheap, in most cases it produces a function very close to the Laguerre function of the second kind, and it is specially well suited for large s and m indices. This method does not set aside the first method, which is used in the lower indexes s and m, case in which the second method can not be applied.

It is worth noting that both methods described above, produce a solution to the spheroidal

angular differential equation, as they are built over linear combinations of the standard solutions. This can be verified numerically by using numerical derivatives to evaluate both the ordinary differential equation and the wronskian relation of the angular spheroidal functions. Examples of $SX_s^m(c;\eta)$ and numerical tests are shown in the next figures.

Figures 5.9 to 5.14 and figures 5.21 to 5.26 show angular functions SX_s^m for $s = 20$ and $s = 10$ with $m = 0$, with increasing spheroidal parameter c, respectively in comparison with their angular function of the first kind $S_s^{m(1)}$ and associated paraxial solution XL_n^m, whereas figures 5.15 to 5.20 and figures 5.27 to 5.32 show their respective numerical tests.

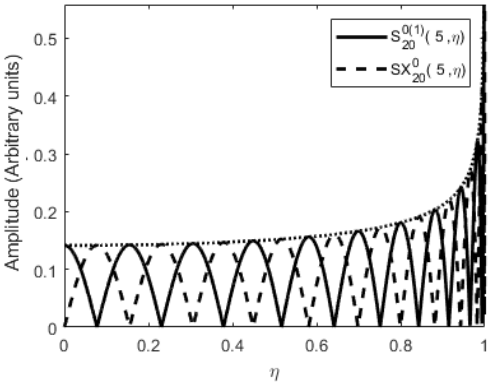

FIGURE 5.9: Comparison of $S_{20}^{0(1)}(5;\eta)$ and $SX_{20}^{0}(5;\eta)$.

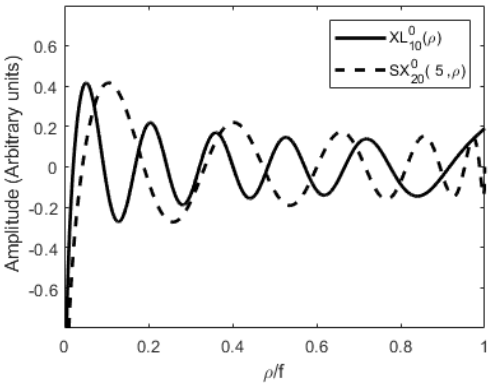

FIGURE 5.10: Comparison of $SX_{20}^{0}(5;\rho)$ and $XL_{10}^{0}(\rho)$.

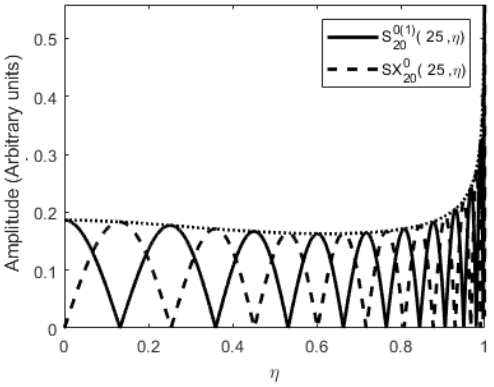

FIGURE 5.11: Comparison of $S_{20}^{0(1)}(25;\eta)$ and $SX_{20}^{0}(25;\eta)$.

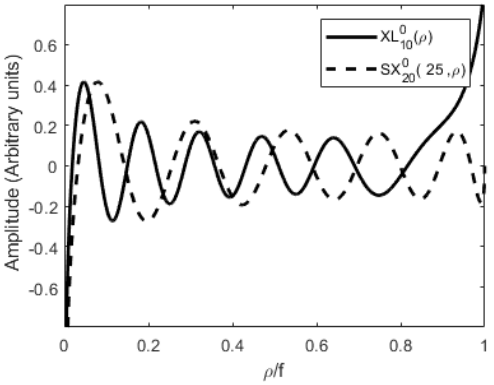

FIGURE 5.12: Comparison of $SX_{20}^{0}(25;\rho)$ and $XL_{10}^{0}(\rho)$.

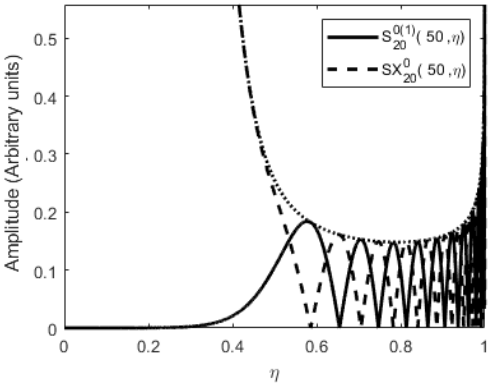

FIGURE 5.13: Comparison of $S_{20}^{0(1)}(50;\eta)$ and $SX_{20}^{0}(50;\eta)$.

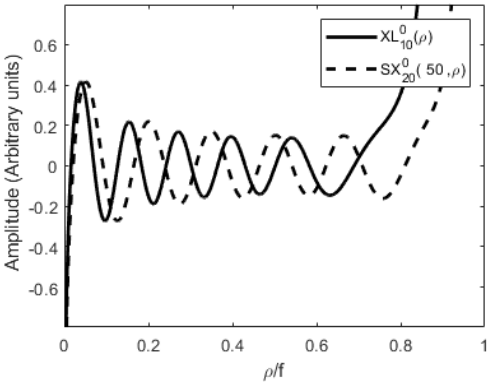

FIGURE 5.14: Comparison of $SX_{20}^{0}(50;\rho)$ and $XL_{10}^{0}(\rho)$.

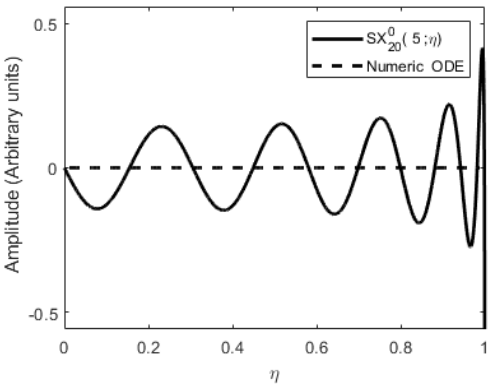

FIGURE 5.15: Ode test for $SX^0_{20}(5;\eta)$.

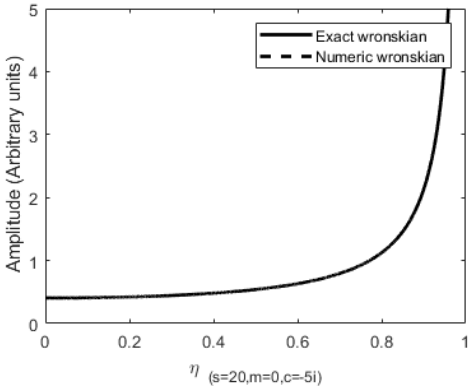

FIGURE 5.16: Wronskian test for $SX^0_{20}(5;\eta)$.

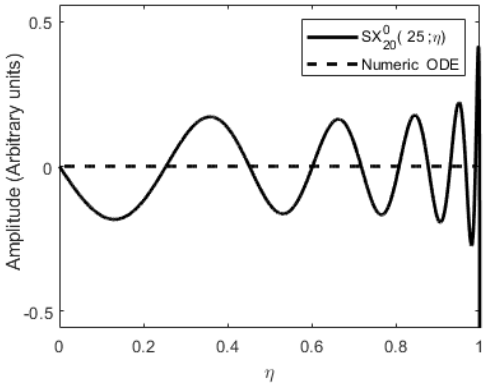

FIGURE 5.17: Ode test for $SX^0_{20}(25;\eta)$.

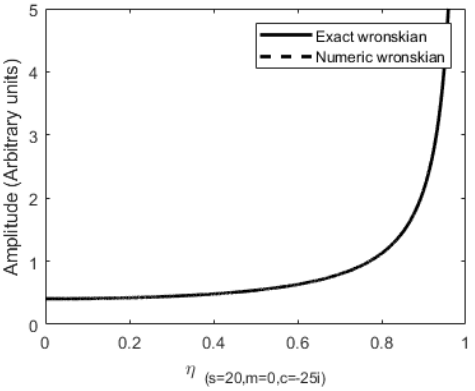

FIGURE 5.18: Wronskian test for $SX^0_{20}(25;\eta)$.

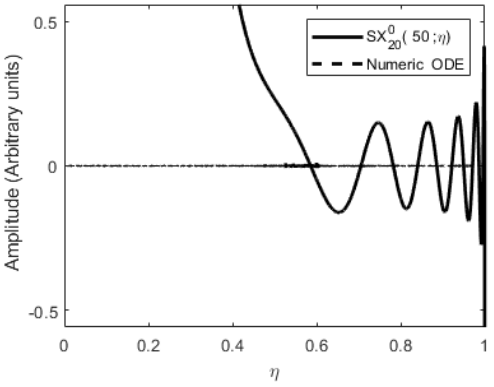

FIGURE 5.19: Ode test for $SX^0_{20}(50;\eta)$.

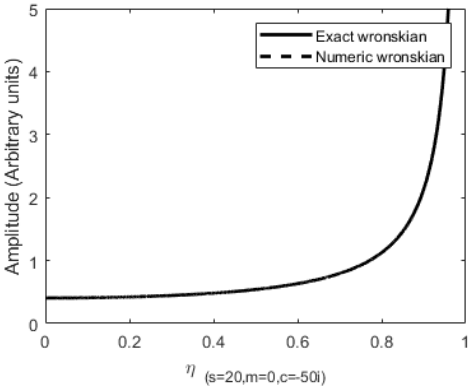

FIGURE 5.20: Wronskian test for $SX^0_{20}(50;\eta)$.

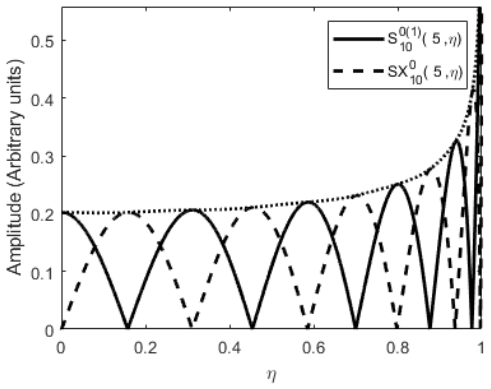

FIGURE 5.21: Comparison of $S_{10}^{0(1)}(5;\eta)$ and $SX_{10}^{0}(5;\eta)$.

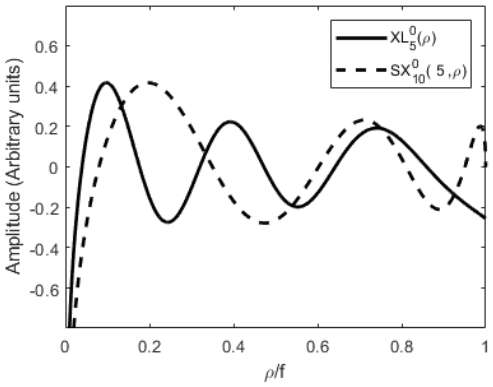

FIGURE 5.22: Comparison of $SX_{10}^{0}(5;\rho)$ and $XL_5^0(\rho)$.

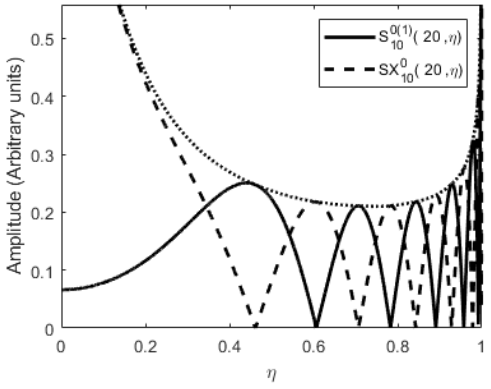

FIGURE 5.23: Comparison of $S_{10}^{0(1)}(20;\eta)$ and $SX_{10}^{0}(20;\eta)$.

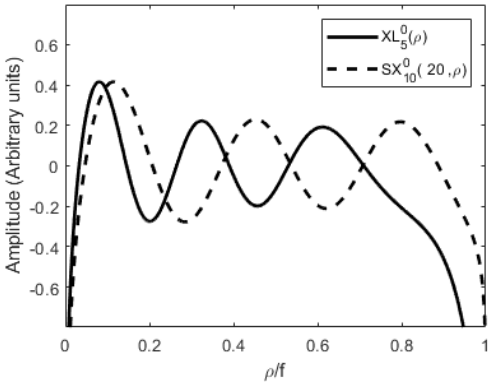

FIGURE 5.24: Comparison of $SX_{10}^{0}(20;\rho)$ and $XL_5^0(\rho)$.

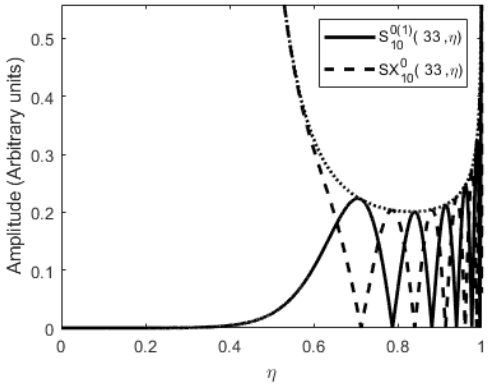

FIGURE 5.25: Comparison of $S_{10}^{0(1)}(33;\eta)$ and $SX_{10}^{0}(33;\eta)$.

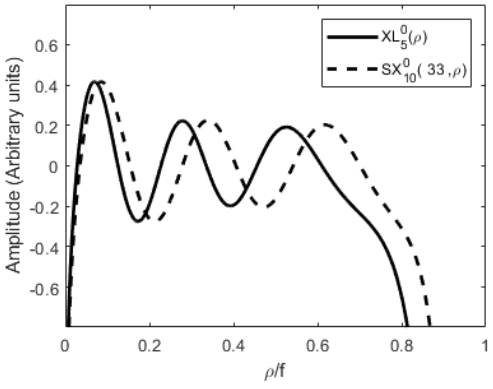

FIGURE 5.26: Comparison of $SX_{10}^{0}(33;\rho)$ and $XL_5^0(\rho)$.

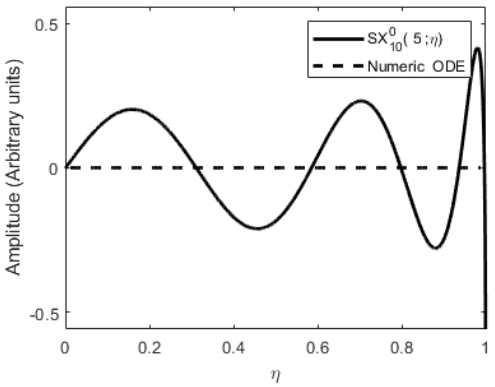

FIGURE 5.27: Ode test for $SX^0_{10}(5;\eta)$.

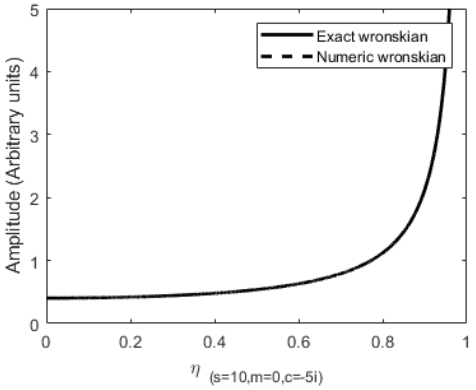

FIGURE 5.28: Wronskian test for $SX^0_{10}(5;\eta)$.

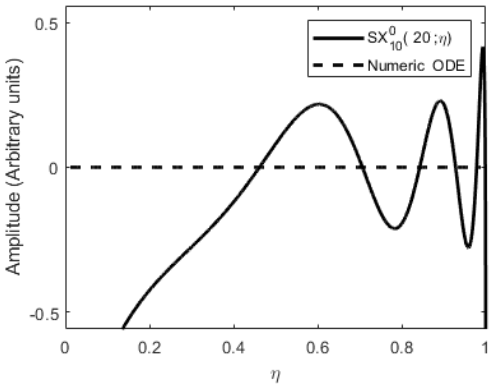

FIGURE 5.29: Ode test for $SX^0_{10}(20;\eta)$.

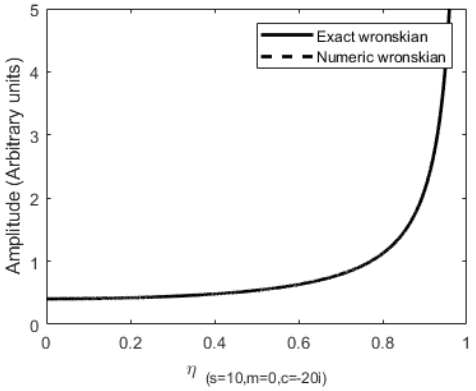

FIGURE 5.30: Wronskian test for $SX^0_{10}(20;\eta)$.

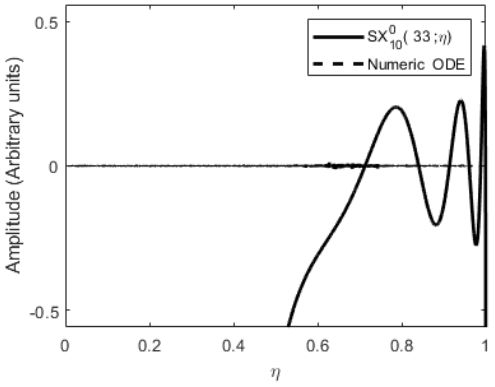

FIGURE 5.31: Ode test for $SX^0_{10}(33;\eta)$.

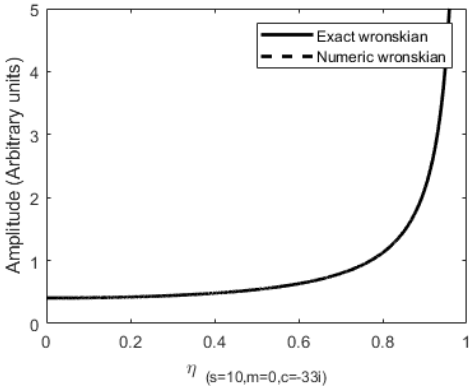

FIGURE 5.32: Wronskian test for $SX^0_{10}(33;\eta)$.

5.3 Limits of the angular expansions

By using the methods described in the previous section, at the threshold of the values calculated via equation (4.50), we face a problem inherent to the angular functions, namely, as the spheroidicity parameter c increases, $S_s^{m(2)}(c;\eta)$ grows exponentially compared to $S_s^{m(1)}(c;\eta)$, so that the coefficients c_1 and c_2 suffer the same problem. In order to illustrate this, a logarithmic plot of the coefficients $c_1(c)$ and $c_2(c)$ is shown in figures 5.33 and 5.34.

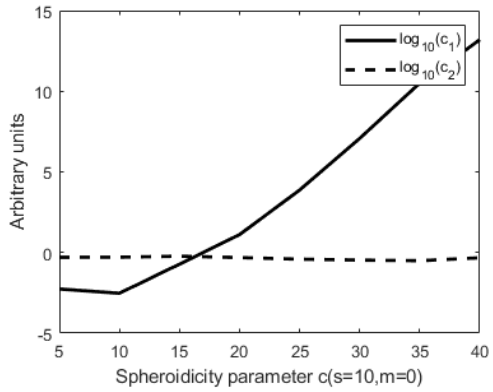

FIGURE 5.33: Normalization coefficients behavior with $s = 10, m = 0$.

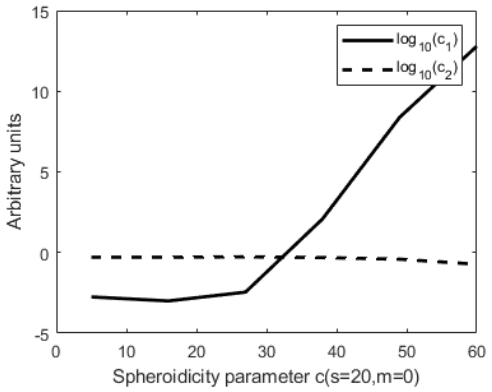

FIGURE 5.34: Normalization coefficients behavior with $s = 20, m = 0$.

In the best case, by working with double-precision arithmetic, we obtain the angular functions with fourteen decimal places, and as Figures 5.33 to 5.34 suggest, we do not have enough significant digits to obtain $SX_s^m(c;\eta)$ for values close to the threshold defined by equation (4.50) for most cases. This is also the reason for the choice of the spheroidal parameter c in figures 5.20 and 5.32, as these are approximately the maximum values with acceptable numerical error in the ODE test for their respective indices. That is not the only problem. By increasing the spheroidicity parameter c, the radial function of the second kind $R_s^{m(2)}$ becomes unstable for small values of the product $c\xi$, even using equation (4.29). Both problems can be solved by using a numerical approach to obtain both spheroidal functions of the second kind. The problem of the radial function can be solved by using the fourth order Runge-Kutta method. We have found numerically that a suitable starting point for this method is $c\xi \sim 30$ with initial values $R_s^{m(2)}(c;30)$ and $R_s^{m(2)'}(c;30)$.

From the theory of second order ordinary differential equations [54] the general solution has the form $y = c_1 y_1 + c_2 y_2$ with y_1 and y_2 linearly independent solutions of the differential equation. In order to obtain a particular solution, initial or boundary conditions are required. As we are interested in a solution to the spheroidal angular differential equation that behaves closer to SX_s^m than to $S_s^{m(1)}$, we use the Laguerre function of the second kind X_n^m as reference in the neighborhood of $\rho \sim 0$ ($\eta \sim 1$). With that, the

initial conditions can be written as

$$\begin{aligned}
\eta_0 &= 1 - 10^{-12}, \\
y(\eta_0) &= 2^{\frac{m+1}{2}} \sqrt{\frac{n!}{\pi(m+n)!}} \left(\frac{f\sqrt{1-\eta_0^2}}{\omega_0^2}\right)^m X_n^m \left(\frac{2f^2\left(1-\eta_0^2\right)}{\omega_0^2}\right) \exp\left(-\frac{f^2\left(1-\eta_0^2\right)}{\omega_0^2}\right), \\
y'(\eta_0) &= 2^{\frac{m+1}{2}} \sqrt{\frac{n!}{\pi(m+n)!}} \frac{d}{d\eta} \left(\frac{f\sqrt{1-\eta^2}}{\omega_0^2}\right)^m X_n^m \left(\frac{2f^2\left(1-\eta^2\right)}{\omega_0^2}\right) \exp\left(-\frac{f^2\left(1-\eta^2\right)}{\omega_0^2}\right) \Bigg|_{\eta\to\eta_0}.
\end{aligned} \tag{5.13}$$

The solution of the spheroidal angular differential equation with the initial conditions (5.13), namely SN_s^m, can be obtained by using standard numerical methods. For the Matlab software, the best results are obtained by using the solvers *ode45* and *ode113*. According to the Matlab description, *ode45* and *ode113* are solvers for non-stiff differential equations (equations where the step of the calculation is inaccurate for the variations of the solution [55]). *ode113* is described as "*a variable-step, variable-order (VSVO) Adams-Bashforth-Moulton PECE solver of orders 1 to 13*", on the other hand, *ode45* is described as "*based on an explicit Runge-Kutta (4,5) formula*". *ode45* has the best results if the domain is defined with a small step vector (in the order of $\delta\eta \sim 10^{-6}$), otherwise, *ode113* is more effective.

The angular function of the first kind $S_s^{m(1)}$ and the numeric solution SN_s^m described above conform a new basis in order to obtain SX_s^m using the methods described previously. The numeric angular function SN_s^m is linearly independent of the angular function of the first kind $S_s^{m(1)}$ because the initial condition (5.13) describes, approximately, a singularity which $S_s^{m(1)}$ does not possess. Figures 5.35 to 5.40 show the angular functions of the first kind $S_s^{m(1)}$ and the resulting second kind SX_s^m.

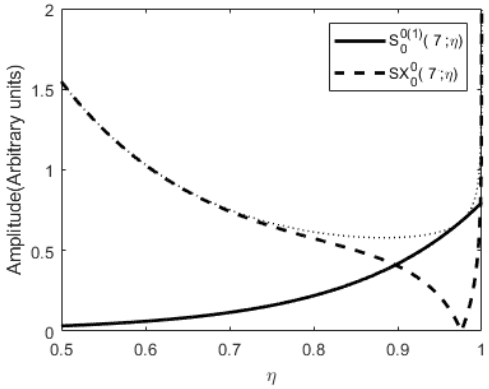

FIGURE 5.35: Angular functions $S_0^{0(1)}(7,\eta)$ and $SX_0^0(7,\eta)$.

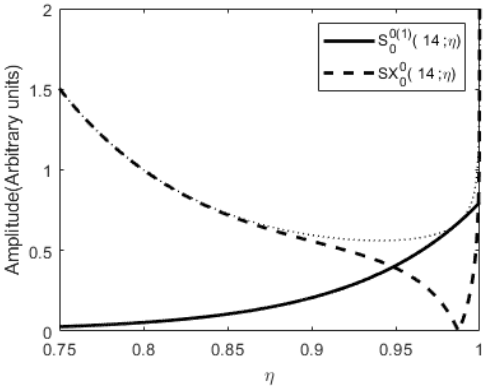

FIGURE 5.36: Angular functions $S_0^{0(1)}(14,\eta)$ and $SX_0^0(14,\eta)$.

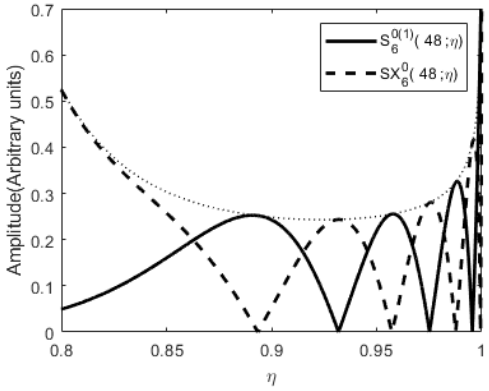

FIGURE 5.37: Angular functions $S_6^{0(1)}(48,\eta)$ and $SX_6^0(48,\eta)$.

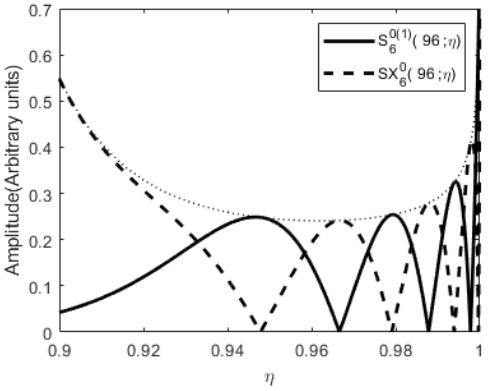

FIGURE 5.38: Angular functions $S_6^{0(1)}(96,\eta)$ and $SX_6^0(96,\eta)$.

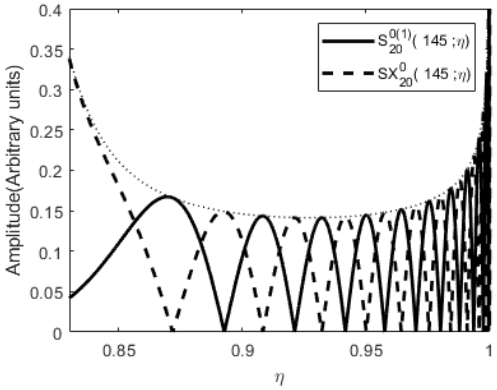

FIGURE 5.39: Angular functions $S_{20}^{0(1)}(145,\eta)$ and $SX_{20}^0(145,\eta)$.

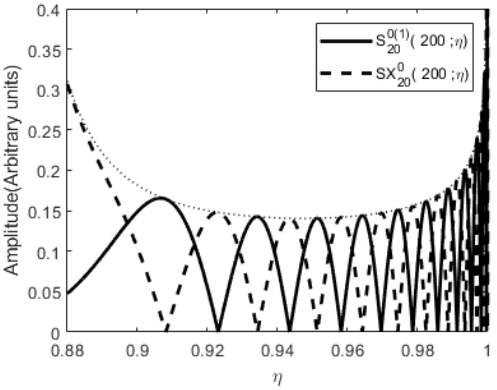

FIGURE 5.40: Angular functions $S_{20}^{0(1)}(200,\eta)$ and $SX_{20}^0(200,\eta)$.

5.4 The second angular spheroidal solution and its relation with the second Laguerre function

By using the methods developed in previous sections, we are now able to obtain the angular function SX_s^m up to $c \sim 300$. From section 4.3.4 we know that the asymptotic expansion for large c of the oblate spheroidal angular function of the first kind is

$$S_s^{m(1)}(c;\eta) \sim \left(\frac{\rho}{f}\right)^m \exp\left(-\frac{k\rho^2}{2f}\right) L_s^m\left(\frac{k\rho^2}{f}\right). \tag{5.14}$$

We expect that the asymptotic expansion of the angular function of the second kind SX_s^m takes the form

$$SX_s^m(c;\eta) \sim \left(\frac{\rho}{f}\right)^m \exp\left(-\frac{k\rho^2}{2f}\right) X_n^m\left(\frac{k\rho^2}{f}\right), \tag{5.15}$$

We will compare the angular function SX_s^m and the second Laguerre function X_n^m, at the focal plane $z = 0$. In this plane, the asymptotic expansion (5.15) is valid only inside the focal disk, that is, a circle with radius f. The border of this disk corresponds to the level curve associated to $\eta = 0$, and the value of the angular functions at this border is finite, as there is no singularity in the spheroidal angular differential equation defined at $\eta = 0$. Nonetheless, the amplitude of the angular function of the second kind SX_s^m at $\eta = 0$ increases exponentially for increasing values of c. In figures 5.41 and 5.42 the behavior of the angular function of the second kind is shown, with the horizontal axis in units of focal distance f in order to compare the increasing value in the border of the angular function of the second kind SX_s^m. It can be seen that even at small spheroidicity parameters c, small increases of c yield large increases in the value of SX_s^m at the border of the focal disk.

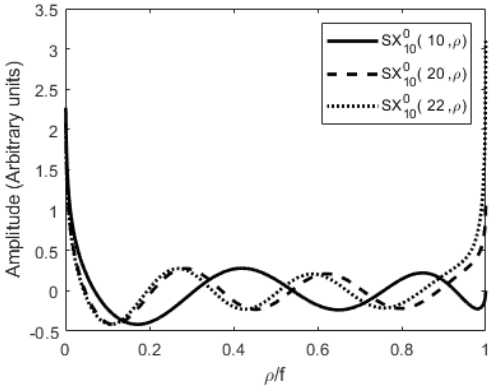

FIGURE 5.41: Behavior $SX_{10}^0(c,\rho)$ for increasing c.

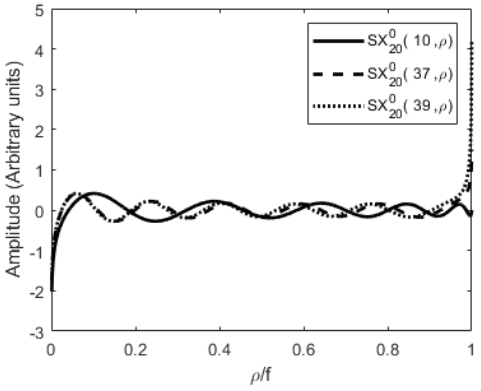

FIGURE 5.42: Behavior $SX_{20}^0(c,\rho)$ for increasing c.

The Angular function SX_s^m behaves asymptotically as the second solution of the paraxial wave equation in circular cylindrical coordinates, which involves the second Laguerre function X_n^m, with increasing c, as verified by numerical inspection of the asymptotic expansion (5.15). This is illustrated in figures 5.43 and 5.44, where the horizontal axis is in units of the spot size of the associated Laguerre-Gauss beam, $\omega_L = \omega_0\sqrt{2n+m+1}$, for comparison.

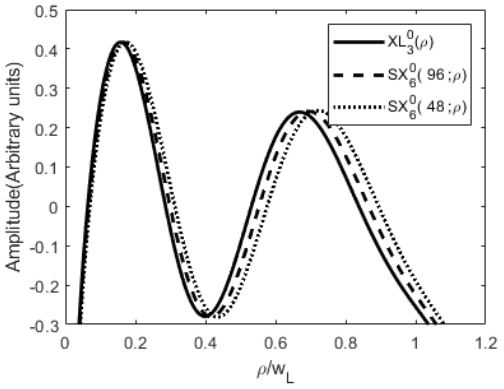

FIGURE 5.43: Behavior $SX_6^0(c,\rho)$ at increasing c.

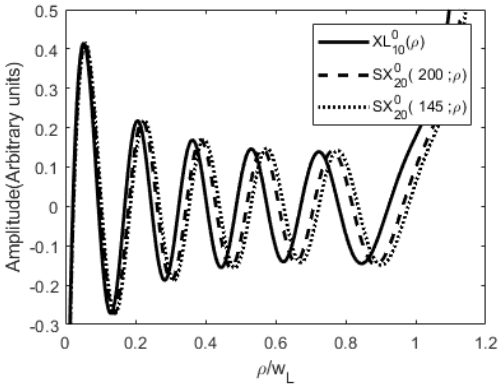

FIGURE 5.44: Behavior $SX_20^0(c,\rho)$ at increasing c.

The spheroidal beam, which is an exact solution to the Helmholtz equation, can be written as

$$\psi_s^{m(1)}(c;\eta) = S_s^{m(1)}(c;\eta)R_s^{m(3)}(c;\xi)\,e^{im\phi}. \tag{5.16}$$

In analogy to the spheroidal beam (5.16), which was described in the previous chapter, we construct another solution using SX_s^m, which from now on we will call angular function of the third kind,

$$\psi_s^{m(2)}(c;\eta) = SX_s^m(c;\eta)R_s^{m(3)}(c;\xi)\,e^{im\phi}. \tag{5.17}$$

The spheroidal function $\psi_s^{m(2)}(c;\eta)$ solves one of the critical problems in the treatment of Hankel-like solutions to the paraxial wave equation in circular cylindrical coordinates which involves the second Laguerre Function X_n^m, in the following sense: the paraxial Hankel-like solutions approach infinity as $\rho \to \infty$. In the focal plane, as described earlier, the angular function varies only inside the focal disk, where the radial function of the third kind $R_s^{m(3)}(c;\xi)$ is constant; outside this region, the angular function is constant, and the radial function is monotonically decreasing. In consequence, the full wavefunction $\psi_s^{m(2)}(c;\eta)$ does not approach infinity as $\rho \to \infty$, regardless of how large the angular function might be at the border of the focal disk. Like in the spheroidal beam $\psi_s^{m(1)}(c;\eta)$ case, the radial function of the third kind $R_s^{m(3)}(c;\xi)$ describes the phase wavefronts, the Guoy phase shift, the direction of the rays from the Eikonal and

the change in the intensity due to propagation, while the angular function describes the transverse profile of the beam. In analogy to the Hankel and the Hankel-Laguerre waves described in chapter 3, we use the spheroidal wavefunctions $\psi_s^{m(1)}(c;\eta)$ and $\psi_s^{m(2)}(c;\eta)$ to build Hankel-like spheroidal waves in the form

$$\begin{aligned} H_s^{m(1)} &= \psi_s^{m(1)}(c;\eta) + i\psi_s^{m(2)}(c;\eta), \\ H_s^{m(2)} &= \psi_s^{m(1)}(c;\eta) - i\psi_s^{m(2)}(c;\eta). \end{aligned} \tag{5.18}$$

Also, the spheroidal beam $\psi_s^{m(1)}(c;\eta)$ can be obtained by interference of the Hankel-like waves. That is

$$\begin{aligned} H_s^{m(1)} + H_s^{m(2)} &= \psi_s^{m(1)}(c;\eta) + i\psi_s^{m(2)}(c;\eta) \\ &\quad + \psi_s^{m(1)}(c;\eta) - i\psi_s^{m(2)}(c;\eta), \\ &= 2\psi_s^{m(1)}(c;\eta). \end{aligned} \tag{5.19}$$

The phase of the Hankel-like spheroidal functions $H_s^{m(1)}$ and $H_s^{m(2)}$ varies in function of the value of the spheroidicity parameter c. For values of c smaller than the paraxial threshold defined in equation (4.50), the phase takes a conical shape. By increasing the value of the spheroidicity parameter c, the phase becomes localized cones around the propagation axis, resembling the phase structure of the Hankel-Laguerre waves, as it is expected from the asymptotic expansions discussed in this chapter. Further studies are required in order to describe the properties of the Hankel-like spheroidal waves and their physical behavior. In the next figures, some examples of the Hankel-like spheroidal waves are shown. In Figures 5.45 to 5.50 Hankel like spheroidal functions $H_s^{m(1)}(c,\rho)$ are compared with Hankel-Laguerre functions $XL_n^m(\rho)$. On the other hand, figures 5.51 to 5.56 show the behavior of the spheroidal functions $H_s^{m(1)}(c,\rho)$ with increasing spheroidal parameter c, as the intensity at the border of the focal disk increases but the spheroidal functions remains monotonically decreasing for $\to \infty$.

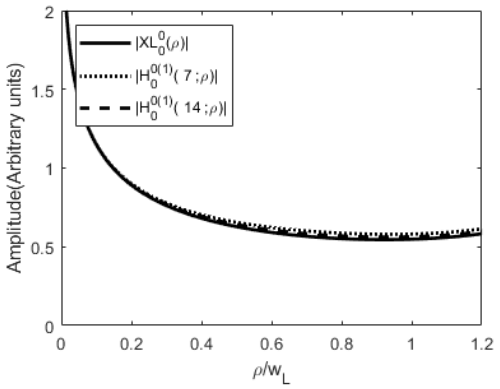

FIGURE 5.45: Amplitude of $H_0^{0(1)}(c,\rho)$ and $XL_0^0(\rho)$.

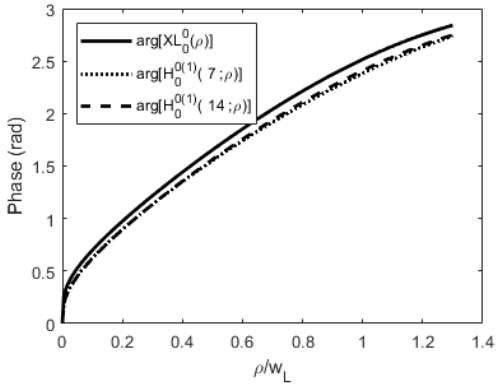

FIGURE 5.46: Phase of $H_0^{0(1)}(c,\rho)$ and $XL_0^0(\rho)$.

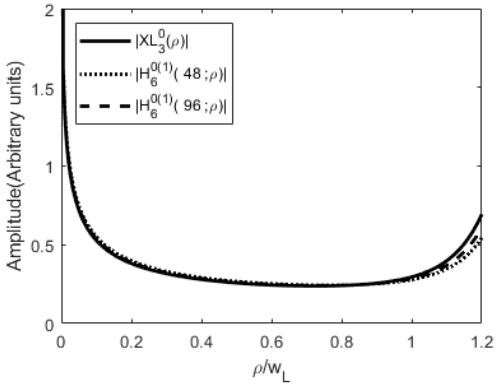

FIGURE 5.47: Amplitude of $H_6^{0(1)}(c,\rho)$ and $XL_3^0(\rho)$.

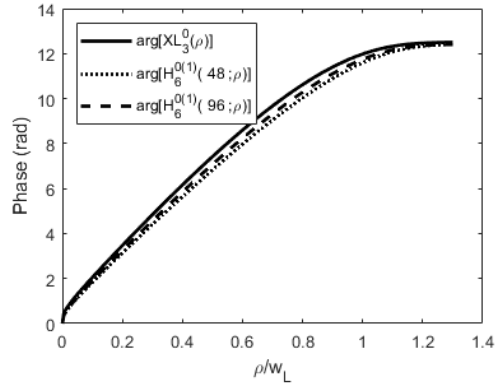

FIGURE 5.48: Phase of $H_6^{0(1)}(c,\rho)$ and $XL_3^0(\rho)$.

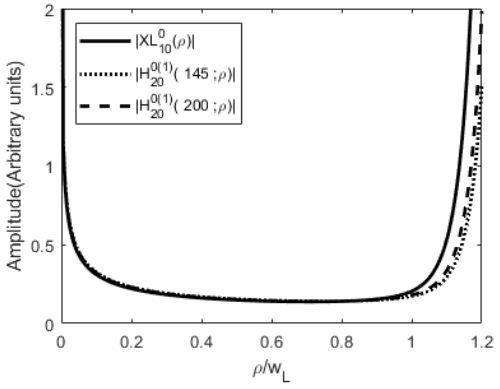

FIGURE 5.49: Amplitude of $H_{20}^{0(1)}(c,\rho)$ and $XL_{10}^0(\rho)$.

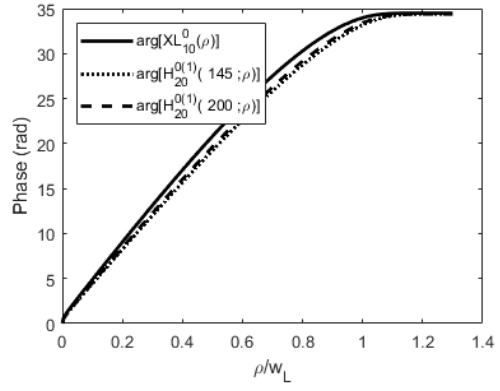

FIGURE 5.50: Phase of $H_{20}^{0(1)}(c,\rho)$ and $XL_{10}^0(\rho)$.

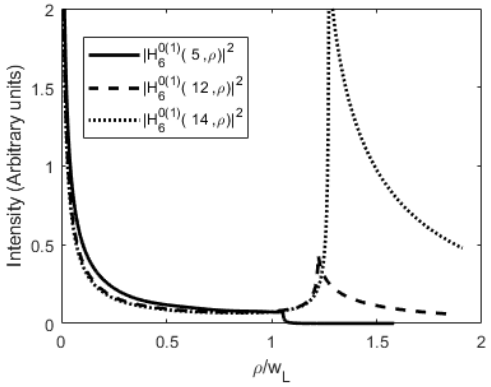

FIGURE 5.51: Behavior of $H_6^{0(1)}(c,\rho)$ intensity with increasing c.

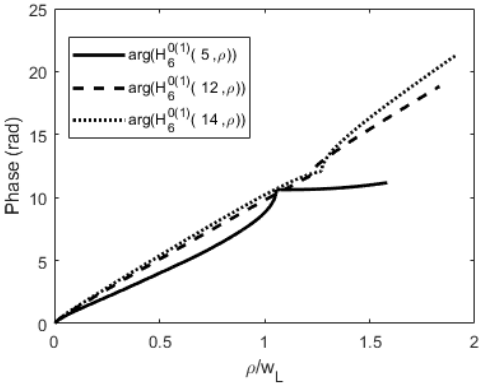

FIGURE 5.52: Behavior of $H_6^{0(1)}(c,\rho)$ phase with increasing c.

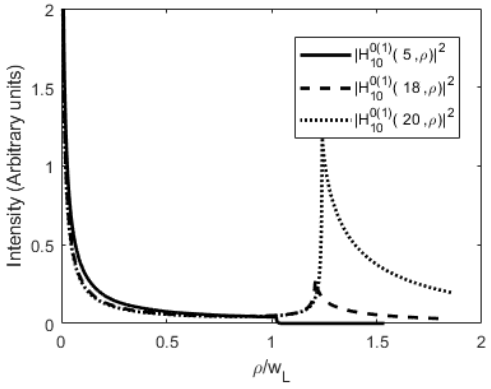

FIGURE 5.53: Behavior of $H_{10}^{0(1)}(c,\rho)$ intensity with increasing c.

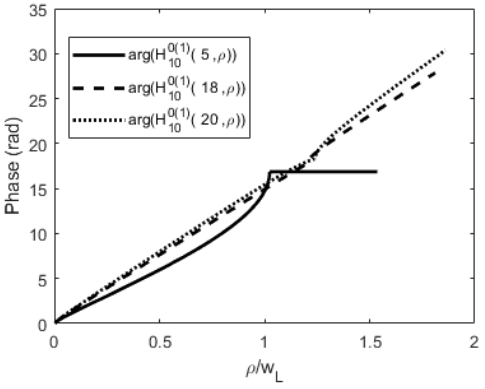

FIGURE 5.54: Behavior of $H_{10}^{0(1)}(c,\rho)$ phase with increasing c.

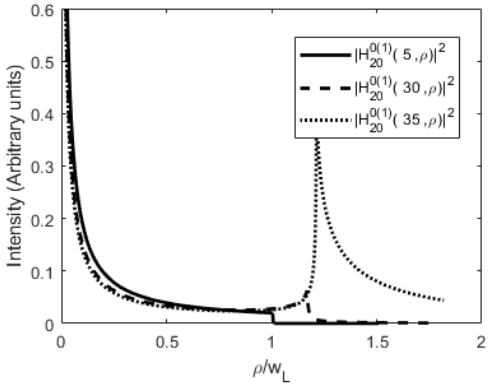

FIGURE 5.55: Behavior of $H_{20}^{0(1)}(c,\rho)$ intensity with increasing c.

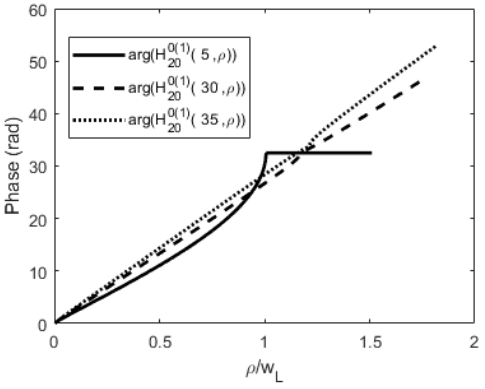

FIGURE 5.56: Behavior of $H_{20}^{0(1)}(c,\rho)$ phase with increasing c.

Conclusions and perspectives

The present work has been addressed to investigate a second solution to the angular equation of the oblate spheroidal coordinates SX_s^m, that behaves asymptotically as the second Laguerre function X_n^m described in the work of Jaimes-Nájera [22] in the following sense:

$$SX_s^m(c;\eta) \sim \left(\frac{\rho}{f}\right)^m \exp\left(-\frac{k\rho^2}{2f}\right) X_n^m\left(\frac{k\rho^2}{f}\right).$$

With this, we have obtained a complete set of solutions to the above mentioned equation, that also behaves asymptotically as the Bessel functions of the first and second kind [22], that is, Hankel-like solutions to the angular spheroidal equation. This solution is achieved through a linear combination of the linearly independent standard angular solutions $S_s^{m(1)}$ and $S_s^{m(2)}$. Given that $S_s^{m(1)}$ is the only angular spheroidal function whose asymptotic behavior has been studied in the literature, SX_s^m has been studied through numerical procedures, since its formal study is out of the scope of this work. However, we have developed a systematic procedure to find numerically the SX_s^m function. The latter consists in the use of geometric relations between the solutions of the associated Laguerre and angular spheroidal equations. Following the work of Rodriguez-Morales [9], in which is presented the unification of the paraxial and non-paraxial beam propagation theories, a threshold was obtained that delimits the paraxial and the non-paraxial behavior of high order spheroidal beams. Using that threshold it was found that the expansion of the angular function of the second kind $S_s^{m(2)}$ described in the literature, is inadequate to solve the aforementioned linear system. This problem is solved by the use of a second solution obtained from the numerical resolution of the spheroidal angular differential equation, whose initial values are those described by the Laguerre function of the second kind X_n^m in the neighborhood of the singularity at zero radial distance. With this alternative second solution, a new set of linearly independent solutions, along with $S_s^{m(1)}$, is obtained so that the systematic procedure above mentioned and described in this work can be applied to obtain SX_s^m. In this way, the angular function SX_s^m can be obtained even for high values of the parameters where the traditional expansions are

inadequate. Furthermore, as stressed in chapter 3, the Hankel-Laguerre waves are not bounded functions of the radial coordinate, due to the divergent behavior of the Laguerre function of the second kind X_n^m. Our hypothesis is that this unbounded behavior is due to the paraxial approximation, since the latter applies very well for short but not for long radial distances. In this respect, the spheroidal angular function described in this work can be used to write solutions to the exact Helmholtz equation that firstly, behave asymptotically as the Hankel-Laguerre waves, and secondly, are bounded functions of the radial coordinate, in spite of growing when approaching the paraxial regime (large spheroidicity parameter c) since it is delimited by a spheroidal radial function that is strictly decreasing away from the propagation axis. By obtaining the second angular solution described, bounded Hankel-like spheroidal waves can be constructed, analogous to those described in the work of Jaimes-Nájera [22]. The analysis of the properties of those waves requires further studies. However, as part of the perspectives of this work, let us discuss briefly the potential application of our results in describing fundamental traveling spheroidal waves.

Perspectives for future work

As described earlier, Hankel-like spheroidal can be constructed with the spheroidal angular functions of the first kind $S_s^{m(1)}$ and the linearly independent spheroidal angular function SX_s^m described in this work. In analogy to Hankel waves, it is expected that these Hankel-like spheroidal waves describe the propagation properties of the spheroidal beam such as the self-healing. Although the problem of unbounded Hankel-Laguerre waves was overcome, in first instance by proposing the bounded Hankel-like spheroidal waves, there is work left to do. For instance, the first problem to solve is to elucidate the rapid growth of the spheroidal function SX_s^m towards the edge of the focal disk discussed in the previous chapter. As any real wave, a spheroidal wave cannot extend infinitely in any direction. Experimentally, one of the most efficient methods to obtain structured beams is by means of a spatial light modulator and diffractive elements[56]. This imposes inherent limits to the spatial bandwidth and extent of the generated beam. As described in the work of Andrews [32], a suitable spot size of a beam is a region that contains all the maxima and minima of the beam. This concept can be used in the case of the spheroidal beams, since they behave asymptotically as the Laguerre-Gauss beams. The spot contains most energy of the spheroidal beams, and as in the case of the Laguerre-Gauss beams, it is a suitable region to truncate in order to generate an experimental beam. A thorough study of the consequences of truncating the Hankel-like spheroidal waves, and the physical behavior described by them, are beyond the scope of work of this thesis and are considered as the future perspectives of this work. However,

let us take as first step the truncation of the Hankel-like spheroidal waves (5.18) at the spot size of the associated spheroidal beams. This truncation may not greatly affect the phase structure of the Hankel-like spheroidal waves as shown in figures 5.57 and 5.58, where the units are given in terms of the Laguerre waist w_L and radians, since, for

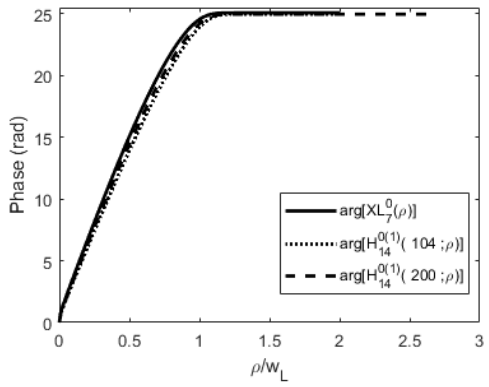

FIGURE 5.57: Phase of Spheroidal waves $H_{14}^{0(1)}(c, z = 0)$.

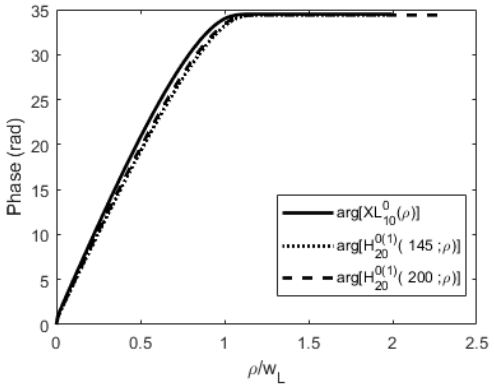

FIGURE 5.58: Phase of Spheroidal waves $H_{20}^{0(1)}(c, z = 0)$.

spheroidicity parameters c approximately or greater than the paraxial threshold (4.50), the phase of the Hankel-like waves is almost plane outside the spot disk, and the direction of energy transfer described by the Eikonal rays indicates that the energy outside the spot disk does not interferes with the interior in both Hankel-like spheroidal waves. This is illustrated in figures 5.59 and 5.60, where the red line represents a ray in the neighborhood of the spot disk.

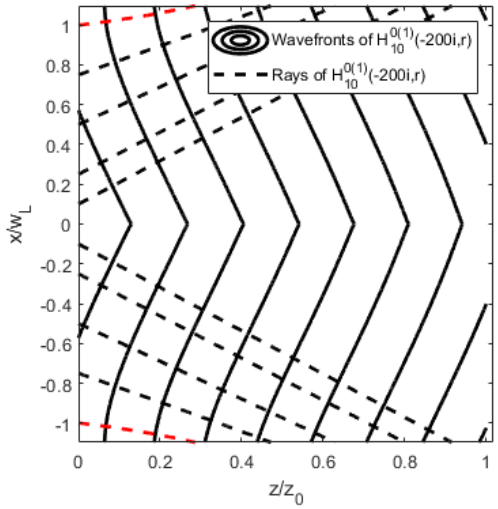

FIGURE 5.59: Wavefronts and rays of the spheroidal wave $H_{20}^{0(1)}(200, r)$.

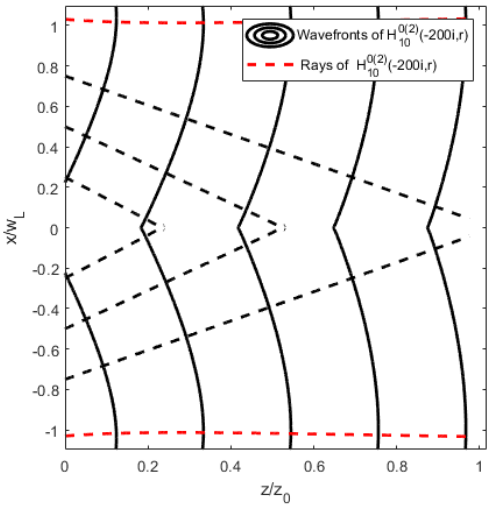

FIGURE 5.60: Wavefronts and rays of the spheroidal wave $H_{20}^{0(2)}(200, r)$.

The propagation of such truncated waves is shown in figures 5.61 to 5.64 along with the

Hankel-Laguerre waves truncated in the same way, for comparison purposes.

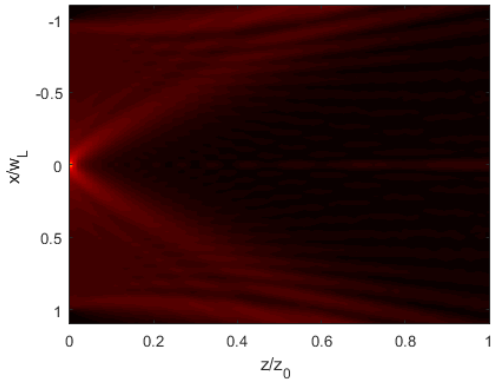

FIGURE 5.61: Simulation of Hankel-Laguerre wave $h_{10}^{0(1)}(r)$.

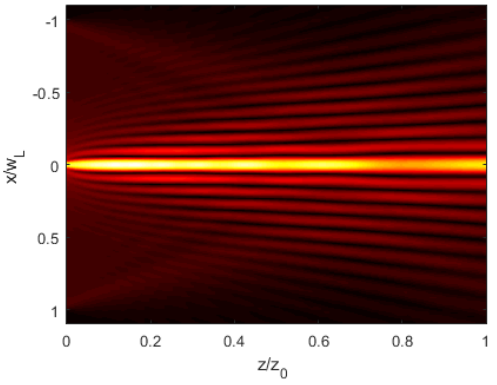

FIGURE 5.62: Simulation of Hankel-Laguerre wave $h_{10}^{0(2)}(r)$.

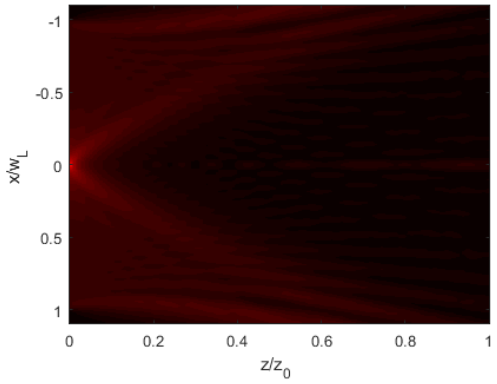

FIGURE 5.63: Simulation of Hankel-like spheroidal wave $H_{20}^{0(1)}(r)$.

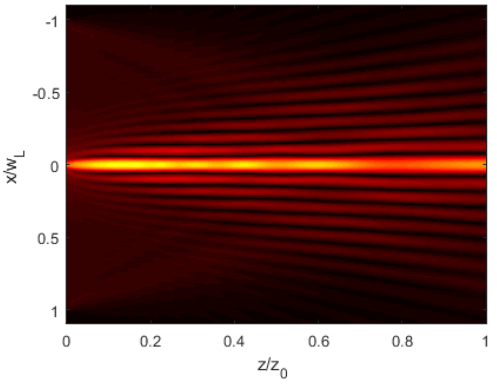

FIGURE 5.64: Simulation of Hankel-like spheroidal wave $H_{20}^{0(2)}(r)$.

At first glance, they behave according to their Hankel-like nature, that is $H_s^{m(1)}$ behaves as a diverging wave and $H_s^{m(2)}$ as a converging one towards the propagation axis.
Finally we present the propagation of an off-axis obstructed spheroidal beam. In order to test if the Hankel-like spheroidal waves do carry physical information, we calculate trajectories normal to the wavefronts of both Hankel-like spheroidal waves. As shown in figures 5.65 to 5.70, at first glance, the truncated Hankel-like spheroidal waves seem to predict the behavior of the shadows of the obstructed spheroidal beam.

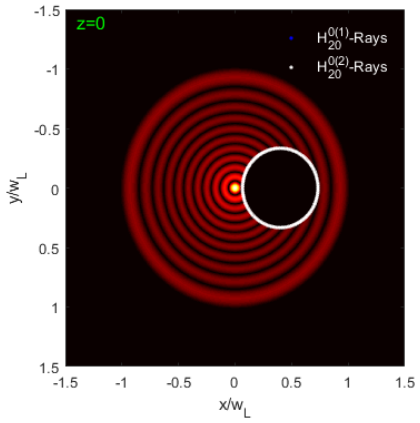

FIGURE 5.65: Simulation of obstructed $\psi_{20}^{0(1)}$ at $z = 0$

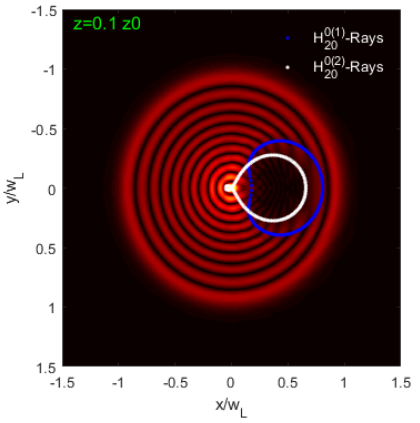

FIGURE 5.66: Simulation of obstructed $\psi_{20}^{0(1)}$ at $z = 0.1\, z_0$

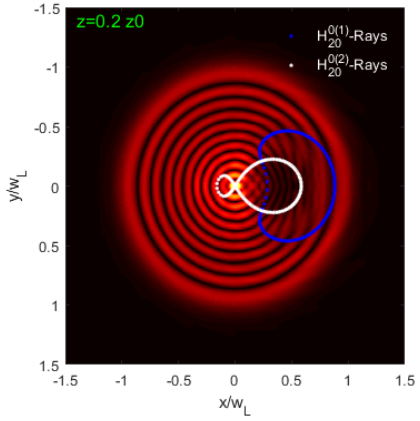

FIGURE 5.67: Simulation of obstructed $\psi_{20}^{0(1)}$ at $z = 0.2\, z_0$

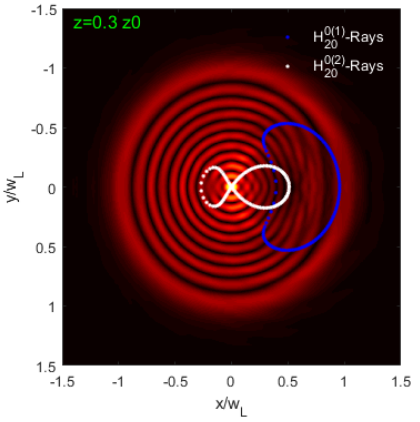

FIGURE 5.68: Simulation of obstructed $\psi_{20}^{0(1)}$ at $z = 0.3\, z_0$

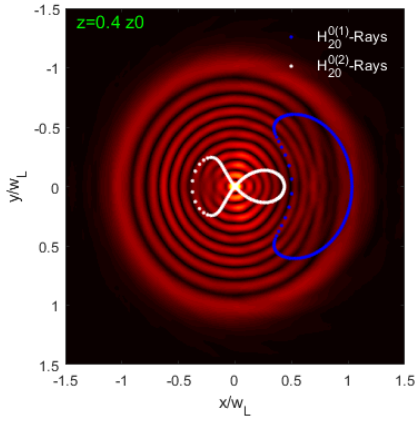

FIGURE 5.69: Simulation of obstructed $\psi_{20}^{0(1)}$ at $z = 0.4\, z_0$

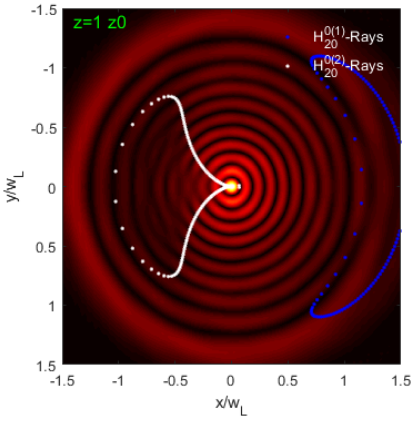

FIGURE 5.70: Simulation of obstructed $\psi_{20}^{0(1)}$ at $z = z_0$

Nevertheless, as mentioned before a thorough study of the physics of the Hankel-like spheroidal waves as well as their seemingly necessary truncation, are the perspectives of this work.

Bibliography

[1] G. F.F. G. Hertz's miscellaneous papers. *Nature*, 1896. ISSN 00280836. doi: 10.1038/055006f0.

[2] J. C. Maxwell. A Dynamical Theory of the Electromagnetic Field. *Philosophical Transactions of the Royal Society of London*, 1865. ISSN 0261-0523. doi: 10.1098/rstl.1865.0008.

[3] Anthony E. Siegman. *Lasers*. University Science Books, 1986. ISBN 0-935702-11-3.

[4] David McGloin Miles J. Padgett, Justin Molloy. *Optical Tweezers: Methods and Applications (Series in Optics and Optoelectronics)*. Chapman and Hall/CRC, 2010. ISBN 1420074121. URL https://www.amazon.com/Optical-Tweezers-Methods-Applications-Optoelectronics/dp/1420074121?SubscriptionId=AKIAIOBINVZYXZQZ2U3A{&}tag=chimbori05-20{&}linkCode=xm2{&}camp=2025{&}creative=165953{&}creativeASIN=1420074121.

[5] H. Kogelnik and T. Li. Laser Beams and Resonators. *Proceedings of the IEEE*, 1966. ISSN 15582256. doi: 10.1109/PROC.1966.5119.

[6] S. Y. Shin and L. B. Felsen. Gaussian beam modes by multipoles with complex source points. *Journal of the Optical Society of America*, 1977. ISSN 0030-3941. doi: 10.1364/JOSA.67.000699.

[7] Kwai-Man Luk and Ping-Kong Yu. Generation of Hermite–Gaussian beam modes by multipoles with complex source points. *J. Opt. Soc. Am. A*, 2(11):1818–1820, nov 1985. doi: 10.1364/JOSAA.2.001818. URL http://josaa.osa.org/abstract.cfm?URI=josaa-2-11-1818.

[8] A. L. Cullen and P. K. Yu. Complex Source-Point Theory of the Electromagnetic Open Resonator. *Proceedings of the Royal Society A: Mathematical, Physical and Engineering Sciences*, 1979. ISSN 1364-5021. doi: 10.1098/rspa.1979.0045.

[9] G Rodriguez-Morales and S Chavez-Cerda. Exact nonparaxial beams of the scalar Helmholtz equation. *Optics Letters*, 2004. ISSN 0146-9592. doi: 10.1364/ol.29.000430.

[10] J. Durnin. Exact solutions for nondiffracting beams I The scalar theory. *Journal of the Optical Society of America A*, 1987. ISSN 1084-7529. doi: 10.1364/JOSAA.4.000651.

[11] J. Durnin, J. Miceli, and J. H. Eberly. Diffraction-free beams. *Physical Review Letters*, 1987. ISSN 00319007. doi: 10.1103/PhysRevLett.58.1499.

[12] L. Allen, M. W. Beijersbergen, R. J.C. Spreeuw, and J. P. Woerdman. Orbital angular momentum of light and the transformation of Laguerre-Gaussian laser modes. *Physical Review A*, 1992. ISSN 10502947. doi: 10.1103/PhysRevA.45.8185.

[13] Graham Gibson, Johannes Courtial, Miles J Padgett, Mikhail Vasnetsov, Valeriy Pas'ko, Stephen M Barnett, and Sonja Franke-Arnold. Free-space information transfer using light beams carrying orbital angular momentum. *Opt. Express*, 12(22):5448–5456, nov 2004. doi: 10.1364/OPEX.12.005448. URL http://www.opticsexpress.org/abstract.cfm?URI=oe-12-22-5448.

[14] David McGloin Miles J. Padgett, Justin Molloy. *Optical Tweezers: Methods and Applications (Series in Optics and Optoelectronics)*. Chapman and Hall/CRC, 2010. ISBN 1420074121. URL https://www.amazon.com/Optical-Tweezers-Methods-Applications-Optoelectronics/dp/1420074121?SubscriptionId=AKIAIOBINVZYXZQZ2U3A{&}tag=chimbori05-20{&}linkCode=xm2{&}camp=2025{&}creative=165953{&}creativeASIN=1420074121.

[15] V. Garcés-Chávez, K. Volke-Sepulveda, S. Chávez-Cerda, W. Sibbett, and K. Dholakia. Transfer of orbital angular momentum to an optically trapped low-index particle. *Phys. Rev. A*, 66:063402, Dec 2002. doi: 10.1103/PhysRevA.66.063402. URL https://link.aps.org/doi/10.1103/PhysRevA.66.063402.

[16] Alfonso Jaimes-Nájera, Jorge Alberto Ugalde-Ontiveros, Songjie Luo, Jixiong Pu, and Sabino Chávez-Cerda. Elegant Laguerre-Gaussian beams as structured wavefields: light on self-healing. In *Frontiers in Optics 2017*, page FM4B.6. Optical Society of America, 2017. doi: 10.1364/FIO.2017.FM4B.6. URL http://www.osapublishing.org/abstract.cfm?URI=FiO-2017-FM4B.6.

[17] Jorge Alberto Ugalde-Ontiveros, Alfonso Jaimes-Nájera, Job Mendoza-Hernández, Marcelo David Iturbe-Castillo, and Sabino Chávez-Cerda. Self-Healing of Laguerre-Gauss Beams described by superposition of conical-like traveling waves. In *Frontiers in Optics 2016*, page JW4A.91. Optical Society of America, 2016. URL http://www.osapublishing.org/abstract.cfm?URI=LS-2016-JW4A.91.

[18] Mendoza Job. *Estudio de la generación y auto reconstrucción de nuevos haces invariantes.* PhD thesis, Benemérita Universidad Autónoma de Puebla, 2011.

[19] S Chávez-cerda. A new approach to bessel beams. *Journal of Modern Optics*, 46(6):923–930, 1999. doi: 10.1080/09500349908231313. URL https://www.tandfonline.com/doi/abs/10.1080/09500349908231313.

[20] Igor A. Litvin, Melanie G. McLaren, and Andrew Forbes. A conical wave approach to calculating Bessel-Gauss beam reconstruction after complex obstacles. *Optics Communications*, 2009. ISSN 00304018. doi: 10.1016/j.optcom.2008.11.079.

[21] Marcelino Anguiano-Morales. Conical dynamics of Bessel beams. *Optical Engineering*, 2007. ISSN 0091-3286. doi: 10.1117/1.2752167.

[22] Chavez-cerda Jaimes-Nájera. Explicit second solution to the associated Laguerre equation and the singular behavior induced by the paraxial approximation. 2018.

[23] J. Meixner, F.W. Schäfke, and G. Wolf. *Mathieu Functions and Spheroidal Functions and their Mathematical Foundations: Further Studies (Lecture Notes in Mathematics)*. Springer, 1981. ISBN 3540102825. URL https://www.amazon.com/Mathieu-Functions-Spheroidal-Mathematical-Foundations/dp/3540102825?SubscriptionId=AKIAIOBINVZYXZQZ2U3A&tag=chimbori05-20&linkCode=xm2&camp=2025&creative=165953&creativeASIN=3540102825.

[24] P. E. Falloon, P. C. Abbott, and J. B. Wang. Theory and computation of spheroidal wavefunctions. *Journal of Physics A: Mathematical and General*, 2003. ISSN 03054470. doi: 10.1088/0305-4470/36/20/309.

[25] M. Born and Emil Wolf. *Principles of optics: Electromagnetic Theory of Propagation, Interference and Diffraction of Light*. Cambridge University Press, 1994. ISBN 0521642221. doi: 10.1016/S0030-3992(00)00061-X.

[26] Bahaa E A Saleh and Malvin Carl Teich. Fundamentals of Photonics , 2nd Edition, 2007. ISSN 0950-0340.

[27] Joseph W. Goodman. Introduction to Fourier Optics, Third Edition, 2004. ISSN 978-0974707723.

[28] Gregory J. Gbur. Mathematical Methods for Optical Physics and Engineering. *Skulls in the Stars*, 2010. ISSN 9780521516105 0521516102. doi: 10.1017/CBO9780511777677.

[29] Robert W Boyd. Intuitive explanation of the phase anomaly of focused light beams. *J. Opt. Soc. Am.*, 70(7):877–880, jul 1980. doi: 10.1364/JOSA.70.000877. URL http://www.osapublishing.org/abstract.cfm?URI=josa-70-7-877.

[30] Sun Cunzhi, Jixiong Pu, and Sabino Chávez-Cerda. Elegant Cartesian Laguerre-Hermite-Gaussian laser cavity modes. *Opt. Lett.*, 40(6):1105–1108, mar 2015. doi: 10.1364/OL.40.001105. URL http://ol.osa.org/abstract.cfm?URI=ol-40-6-1105.

[31] Alfonso Jaimes-Nájera and Sabino Chávez-Cerda. Elegant Laser Resonator Modes with OAM. In *Conference on Lasers and Electro-Optics*, page SW3M.1. Optical Society of America, 2018. doi: 10.1364/CLEO_SI.2018.SW3M.1. URL http://www.osapublishing.org/abstract.cfm?URI=CLEO{_}SI-2018-SW3M.1.

[32] Ronald L Phillips and Larry C Andrews. Spot size and divergence for Laguerre Gaussian beams of any order. *Appl. Opt.*, 22(5):643–644, mar 1983. doi: 10.1364/AO.22.000643. URL http://ao.osa.org/abstract.cfm?URI=ao-22-5-643.

[33] Job Mendoza-Hernández, Maximino Luis Arroyo-Carrasco, Marcelo David Iturbe-Castillo, and Sabino Chávez-Cerda. Laguerre-Gauss beams versus Bessel beams showdown: peer comparison. *Opt. Lett.*, 40(16):3739–3742, aug 2015. doi: 10.1364/OL.40.003739. URL http://ol.osa.org/abstract.cfm?URI=ol-40-16-3739.

[34] N. N. Lebedev. *Special Functions & Their Applications (Dover Books on Mathematics)*. Dover Publications, 1972. ISBN 0486606244. URL https://www.amazon.com/Special-Functions-Their-Applications-Mathematics/dp/0486606244?SubscriptionId=AKIAIOBINVZYXZQZ2U3A&tag=chimbori05-20&linkCode=xm2&camp=2025&creative=165953&creativeASIN=0486606244.

[35] Z. Bouchal, J. Wagner, and M. Chlup. Self-reconstruction of a distorted non-diffracting beam. *Optics Communications*, 1998. ISSN 00304018. doi: 10.1016/S0030-4018(98)00085-6.

[36] F V Atkinson M A D.Phil. LXI. On Sommerfeld's "radiation condition.". *The London, Edinburgh, and Dublin Philosophical Magazine and Journal of Science*, 40 (305):645–651, 1949. doi: 10.1080/14786444908561291. URL https://doi.org/10.1080/14786444908561291.

[37] William E. Boyce and Richard C. DiPrima. *Elementary Differential Equations and Boundary Value Problems*. Wiley, 2012. ISBN 0470458313. URL https://www.amazon.com/Elementary-Differential-Equations-Boundary-Problems/dp/0470458313?SubscriptionId=AKIAIOBINVZYXZQZ2U3A&tag=chimbori05-20&linkCode=xm2&camp=2025&creative=165953&creativeASIN=0470458313.

[38] Hermann Hankel. Die Cylinderfunctionen erster und zweiter Art. *Mathematische Annalen*, 1(3):467–501, sep 1869. ISSN 1432-1807. doi: 10.1007/BF01445870. URL https://doi.org/10.1007/BF01445870.

[39] Milton Abramowitz, Irene A. Stegun, and Robert H. Romer. Handbook of Mathematical Functions with Formulas, Graphs, and Mathematical Tables. *American Journal of Physics*, 1988. ISSN 0002-9505. doi: 10.1119/1.15378.

[40] Alfonso Jaimes-Nájera, Jorge Ugalte-Ontiveros, Job Mendoza-Hernández, Marcelo David Iturbe-Castillo, Victor Arrizón, and Sabino Chavez-Cerda. Hankel-Laguerre exotic beams. *Preprint*, 2018.

[41] George B. Arfken, Hans J. Weber, and Frank E. Harris. *Mathematical Methods for Physicists*. Academic Press, 2013. ISBN 9780123846549. doi: 10.1016/C2009-0-30629-7.

[42] P. Moon and D. E. Spencer. *Field Theory Handbook: Including Coordinate Systems, Differential Equations and Their Solutions*. Springer, 1988. ISBN 3540184309. URL https://www.amazon.com/Field-Theory-Handbook-Coordinate-Differential/dp/3540184309?SubscriptionId=AKIAIOBINVZYXZQZ2U3A&tag=chimbori05-20&linkCode=xm2&camp=2025&creative=165953&creativeASIN=3540184309.

[43] C. Flammer and S.W. Functions. *Spheroidal Wave Functions*. Stanford University Press, 1957. ISBN 9780804716345. URL https://books.google.com.mx/books?id=GjusAAAAIAAJ.

[44] Shanjie Zhang and Jian-Ming Jin. *Computation of Special Functions*. Wiley-Interscience, 1996. ISBN 0471119636. URL https://www.amazon.com/Computation-Special-Functions-Shanjie-Zhang/dp/0471119636?SubscriptionId=AKIAIOBINVZYXZQZ2U3A&tag=chimbori05-20&linkCode=xm2&camp=2025&creative=165953&creativeASIN=0471119636.

[45] Rodes Donald. On the spheroidal functions. *NIST journal of research*, 74b:187, 1970.

[46] Edward L. Ince. *Ordinary Differential Equations (Dover Books on Mathematics)*. Dover Publications, 1956. ISBN 0486603490. URL https://www.amazon.com/Ordinary-Differential-Equations-Dover-Mathematics/dp/0486603490?SubscriptionId=AKIAIOBINVZYXZQZ2U3A&tag=chimbori05-20&linkCode=xm2&camp=2025&creative=165953&creativeASIN=0486603490.

[47] E. T. Whittaker and G. N. Watson. *A Course of Modern Analysis*. Cambridge University Press, 1962. ISBN 0521091896. URL https://www.amazon.com/Course-Modern-Analysis-T-Whittaker/dp/0521091896?SubscriptionId=AKIAIOBINVZYXZQZ2U3A&tag=chimbori05-20&linkCode=xm2&camp=2025&creative=165953&creativeASIN=0521091896.

[48] T Do-Nhat. Asymptotic expansions of the oblate spheroidal eigenvalues and wave functions for large parameter c. *Canadian Journal of Physics*, 2001. ISSN 0008-4204. doi: 10.1139/cjp-79-5-813.

[49] Z Ulanowski and I K Ludlow. Scalar field of nonparaxial Gaussian beams. *Opt. Lett.*, 25(24):1792–1794, dec 2000. doi: 10.1364/OL.25.001792. URL http://ol.osa.org/abstract.cfm?URI=ol-25-24-1792.

[50] B Tehan Landesman and H H Barrett. Gaussian amplitude functions that are exact solutions to the scalar Helmholtz equation. *J. Opt. Soc. Am. A*, 5(10):1610–1619, oct 1988. doi: 10.1364/JOSAA.5.001610. URL http://josaa.osa.org/abstract.cfm?URI=josaa-5-10-1610.

[51] S. Y. Shin and L. B. Felsen. Gaussian beam modes by multipoles with complex source points. *Journal of the Optical Society of America*, 1977. ISSN 0030-3941. doi: 10.1364/JOSA.67.000699.

[52] Kwai-Man Luk and Ping-Kong Yu. Generation of Hermite–Gaussian beam modes by multipoles with complex source points. *J. Opt. Soc. Am. A*, 2(11):1818–1820, nov 1985. doi: 10.1364/JOSAA.2.001818. URL http://josaa.osa.org/abstract.cfm?URI=josaa-2-11-1818.

[53] Fallon Peter. *Theory and Computation of Spheroidal Harmonics with General Arguments*. PhD thesis, The University of Western Australia, 2001.

[54] Edward L. Ince. *Ordinary Differential Equations (Dover Books on Mathematics)*. Dover Publications, 2012. URL https://www.amazon.com/Ordinary-Differential-Equations-Dover-Mathematics-ebook/dp/B00EZDHV9Q?SubscriptionId=AKIAIOBINVZYXZQZ2U3A&tag=chimbori05-20&linkCode=xm2&camp=2025&creative=165953&creativeASIN=B00EZDHV9Q.

[55] J. D. Lambert. *Numerical Methods for Ordinary Differential Systems: The Initial Value Problem*. Wiley, 1991. ISBN 0471929905. URL https://www.amazon.com/Numerical-Methods-Ordinary-Differential-Systems/dp/0471929905?SubscriptionId=AKIAIOBINVZYXZQZ2U3A&tag=chimbori05-20&linkCode=xm2&camp=2025&creative=165953&creativeASIN=0471929905.

[56] Victor Arrizón, Guadalupe Méndez, and David Sánchez-de La-Llave. Accurate encoding of arbitrary complex fields with amplitude-only liquid crystal spatial light modulators. *Optics express*, 2005. ISSN 1094-4087. doi: 10.1364/OPEX.13.007913.